Undrained Bearing Capacity of Misaligned Suction Anchors: A Comparative Study on Different Numerical Approaches

Despoina Chioktouridi

September 2016

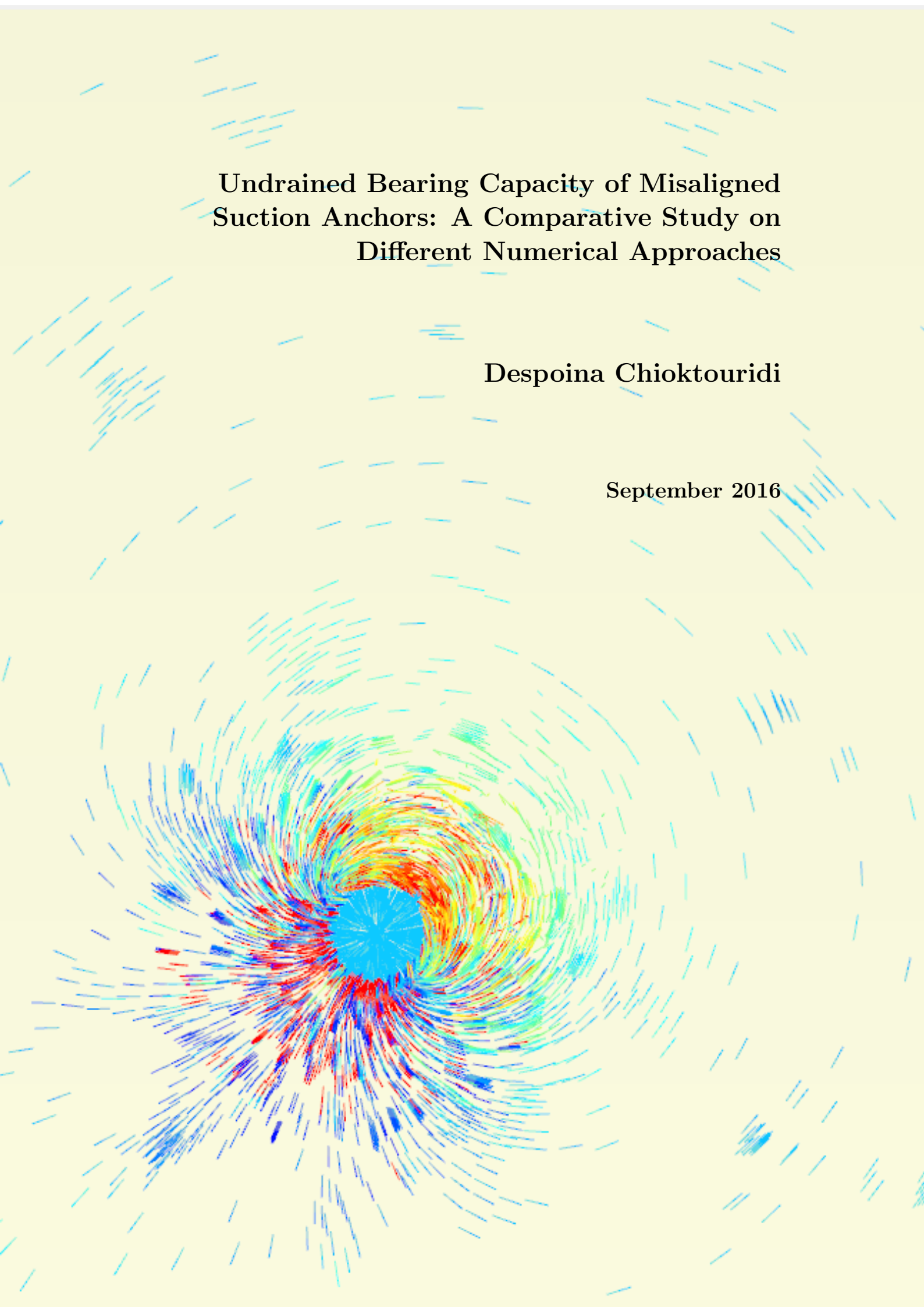

Undrained Bearing Capacity of Misaligned Suction Anchors: A Comparative Study on Different Numerical Approaches

Using Plaxis 3D and SPCalc

A Thesis presented for the degree of
Master of Science in Geo - Engineering

by

Despoina Chioktouridi

Committee:	Prof.dr. K.G. Gavin,	TU Delft, chairman
	Dr. Ir. R.B.J. Brinkgreve,	TU Delft, supervisor
	Dr. F. Pisanò,	TU Delft, daily supervisor

Department of Civil Engineering and Geosciences
Delft University of Technology
September 2016

Abstract

The constantly increasing demand of the world for energy has led to a remarkable advancement in the offshore geotechnical engineering field that is closely related to the oil and gas production. In this industry, floating production facilities are connected with the seabed through mooring lines that are attached to anchor foundations. In this context, suction anchors have been increasingly installed to ensure good mechanical performance under variable operational loads. Therefore, they should be able to withstand the horizontal, vertical and torsional (HVT) loads stemming from the inclined loading imposed by the mooring chains. The undesired torsion is induced in the problem when the anchor is not perfectly aligned with the floating facility due to imperfections during installation.

This work constitutes a comparative study between three distinctive numerical approaches that revolve around the undrained capacity of misaligned suction anchors founded in normally consolidated clay. Its main aim is to unravel the strengths and weaknesses of the well established methods of analysis used nowadays. The effectiveness of the two current adopted methods is shown with reference to a benchmark study that involves a thorough 3D finite element investigation on the impact of misalignment on the capacity of suction anchors following a total stress analysis (TSA) within Plaxis 3D.

Even though this type of analysis (TSA) is widely employed nowadays, it is considered as a rough approximation of the actual soil behaviour under undrained conditions. This statement acted as an incentive to conduct an effective stress analysis (ESA) of the same problem. For this purpose, different calibrations of an advanced Cam - Clay type constitutive model (the Soft Soil model) were realised to capture the soil conditions of the benchmark study, which embraced a simplified Tresca failure criterion. Additionally, a simpler 2D numerical approach of the same problem was realised with the use of SPCalc, which is a special purpose tool that accounts for 3D effects through the application of side shear and reduction factors. In this case, misorientation is modelled by the reduction of the soil - anchor interface resistance.

Failure envelopes are derived for the two current approaches and compared for three different length-to-diameter anchor ratios (1.5, 3 and 6), and for misalignment angles in the range of 0° to 10°. The outcomes of this study give a better insight into the practical implications of certain modelling assumptions. In particular, it is shown that the influence of misalignment on the undrained HV capacity may be in fact non-negligible, while the expected conservatism arising from simplified 2D analysis is quantitatively pointed out. Even though ESA is thought to enhance the mechanical soundness of undrained modelling, it creates additional difficulties in terms of soil parameter calibration. Therefore, the close relationship between HVT failure envelopes and the modelling of clay strength in the effective stress framework is critically discussed with respect to the preliminary results of the benchmark study.

Acknowledgements

The research described in this thesis have been accomplished with the help of a number of people. First of all, I would like to express my special appreciation and thanks to Federico Pisanò for his expert guidance and continuous support during all the steps of my graduation project. His perpetual willingness to listen to my questions and help with my problems was a tremendous help for me.

Next, my sincere thanks goes to Ronald Brinkgreve for his valuable help throughout my thesis. His proficient advice played a fundamental role in the better understanding of numerical and constitutive modelling. Then, I would like to thank Kenneth Gavin for his interest and constructive comments on my work.

I would like to express my gratitude to my colleagues at Plaxis bv that helped deepen my knowledge regarding the wide range of capabilities of the Plaxis software and for their contribution to carrying out my thesis smoothly. Many thanks to Alessio Saviano for his precious guidance during the first steps of my work.

Last but not least, I am immensely grateful to my family and friends for their constant encouragement and wholehearted support throughout my studies. It is an undeniable fact that, without their unconditional love, I would not be able to successfully conclude this important part of my life.

Despoina Chioktouridi
Delft, September 2016

Contents

List of Figures

List of Tables

Nomenclature

Latin lower case symbols

Symbol	*Unit*	*Explanation*
a	-	Shape coefficient of elliptical curves [45]
b	-	Shape coefficient of elliptical curves [45]
c	kN/m^2	Cohesion
d	m	Depth of the padeye
e	-	Void ratio
e_{o}	-	Initial void ratio
f	kN/m^2	Yield function in SPCalc
f_{c}	kN/m^2	Yield function of the Soft Soil cap
f_{f}	kN/m^2	Yield function of the Mohr - Coulomb failure surface
g	kN/m^2	Plastic potential function in SPCalc
h	m	Height of a soil layer in SPCalc
h_{w}	m	Height of the water head
m	-	Shape coefficient of elliptical curves [46]
n	-	Shape coefficient of elliptical curves [46]
p'	kN/m^2	Mean effective stress
p'°	kN/m^2	Initial mean effective stress
p'_{ref}	kN/m^2	Mean effective stress at reference level
p_{p}	kN/m^2	Pre-consolidation stress
q	kN/m^2	Deviatoric stress
r_{soil}	-	Reduction factor for the soil side area in SPCalc
$r_{\mathrm{str,out}}$	-	Reduction factor for the structure side area in SPCalc
s_{u}	kN/m^2	Undrained shear strength
$s_{\mathrm{u,tip}}$	kN/m^2	Undrained shear strength at the tip of the anchor
$s_{\mathrm{u}}^{\mathrm{C}}$	kN/m^2	Undrained shear strength in compression
$s_{\mathrm{u}}^{\mathrm{DSS}}$	kN/m^2	Undrained shear strength in direct simple shear
$s_{\mathrm{u}}^{\mathrm{E}}$	kN/m^2	Undrained shear strength in extension
u	kN/m^2	Pore water pressure
u_{x}	m	Displacement in x direction
u_{y}	m	Displacement in y direction
u_{z}	m	Displacement in z direction
x_{max}	m	Maximum boundary of finite element domain in x direction
x_{min}	m	Minimum boundary of finite element domain in x direction
y_{max}	m	Maximum boundary of finite element domain in y direction
y_{min}	m	Minimum boundary of finite element domain in y direction
z_{cl}	m	Center line loading depth
z_{max}	m	Maximum boundary of finite element domain in z direction
z_{min}	m	Minimum boundary of finite element domain in z direction
z_{p}	m	Depth of the padeye
z_{ref}	m	Reference depth

Latin upper case symbols

Symbol	*Unit*	*Explanation*
A	m^2	Cross sectional area of suction anchor
A_{se}	m^2	External shaft surface area
A_{si}	m^2	Internal shaft surface area
C_c	-	Compression index
C_s	-	Swelling index
D	m	Diameter of suction anchor
D_e	kN/m^2	Elastic constitutive matrix
D_e	m	External diameter of suction anchor
D_{max}	m	Maximum displacement of suction anchor in SPCalc
E_u	kN/m^2	Undrained Young's modulus
F_c	KN	Chain force acting at the padeye in SPCalc
G	kN/m^2	Linear elastic shear modulus
G_{MC}	kN/m^2	Shear modulus of Mohr - Coulomb model
G_{SS}	kN/m^2	Shear modulus of Soft Soil model
H	kN	Horizontal capacity of suction anchors
H_{ult}	kN	Ultimate horizontal capacity of suction anchors
$H_{ult,\beta}$	kN	Ultimate horizontal capacity of suction anchors at β angle
$H_{ult,\beta=0^\circ}$	kN	Ultimate horizontal capacity of suction anchors at $\beta = 0^\circ$
K	kN/m^2	Linear elastic bulk modulus
K_o	-	Lateral earth pressure coefficient
K_o^{tot}	-	Lateral earth pressure coefficient for total stress analysis
K_o^{nc}	-	Lateral earth pressure coefficient in normal consolidation
K_{ur}	kN/m^2	Bulk modulus for unloading - reloading
L	m	Length of suction anchor
L_{cog}	m	Length of center of gravity of a suction anchor in SPCalc
L_f	m	Vertical coordinate of the load attachment point in SPCalc
M	-	Critical state line of Cam - Clay model
$M_{Soft\ Soil}$	-	Critical state line of Soft Soil model
M_{max}	kNm	Torsional capacity of suction anchors in SPCalc
N_c	-	Reverse end bearing factor
N_h	-	Lateral bearing capacity factor [45]
N_{inc}	-	Number of load increments in SPCalc
N_p	-	Lateral bearing capacity factor [38]
Q_b	kN	Reverse end bearing capacity of the suction anchor
Q_s	kN	Bearing capacity due to the skin friction along the shaft of the suction anchor
R_{inter}	-	Interface strength reduction factor in Plaxis
S_0	kN/m^2	Interpolation function of NGI-ADP model in SPCalc
S_1	kN/m^2	Interpolation function of NGI-ADP model in SPCalc
S_2	kN/m^2	Interpolation function of NGI-ADP model in SPCalc
T	kNm	Torsional capacity of suction anchors
T_{ult}	kNm	Ultimate torsional capacity of suction anchors
V	kN	Vertical bearing capacity of suction anchors
V_{ult}	kN	Ultimate vertical bearing capacity of suction anchors
W'_{plug}	kN	Effective weight of the soil plug

Greek lower case symbols

Symbol	*Unit*	*Explanation*
α	-	Adhesion factor
α	$^\circ$	Angle between σ_1 and the z axis in SPCalc
α_{e}	-	Coefficient of external shaft friction
α_{i}	-	Coefficient of internal shaft friction
$\alpha_{\mathrm{inclination}}$	$^\circ$	Angle of loading in vertical plane in SPCalc
α_{out}	-	Set-up skirt - wall friction factor of SPCalc
α_{res}	-	Modified set-up factor of SPCalc
β	$^\circ$	Angle of misalignment
γ'	kN/m^3	Effective unit weight ($=\gamma_{\mathrm{sat}} - \gamma_{\mathrm{w}}$)
γ^{p}	-	Plastic shear strains
γ_{sat}	kN/m^3	Saturated unit weight
γ_{w}	kN/m^3	Unit weight of the water
ϵ_{v}	-	Volumetric strains
$\epsilon_{\mathrm{v}}^{\mathrm{e}}$	-	Elastic volumetric strains
$\epsilon_{\mathrm{v}}^{\mathrm{p}}$	-	Plastic volumetric strains
$\epsilon_{\mathrm{xx}}^{\mathrm{p}}$	-	Plastic volumetric strains in x direction
$\epsilon_{\mathrm{yy}}^{\mathrm{p}}$	-	Plastic volumetric strains in y direction
$\epsilon_{\mathrm{zz}}^{\mathrm{p}}$	-	Plastic volumetric strains in z direction
ϵ_{x}	-	Axial strains at x direction
ϵ_{y}	-	Axial strains at y direction
ϵ_{z}	-	Axial strains at z direction
θ	$^\circ$	Loading angle in the vertical plane
κ^*	-	Modified swelling index of Soft Soil model
λ^*	-	Modified compression index of Soft Soil model
ν'	-	Poisson's ratio for undrained effective stress analysis
ν_{u}	-	Poisson's ratio for undrained total stress analysis
ν_{ur}	-	Poisson's ratio for unloading/reloading
ξ	-	Reduction factor due to open crack in SPCalc
σ_{xx}	kN/m^2	Total stress in x direction
σ_{zz}	kN/m^2	Total stress in z direction
σ_1	kN/m^2	Maximum principal compressive strength
σ_1'	kN/m^2	Vertical principal effective stress
σ_3'	kN/m^2	Horizontal principal effective stress
τ	kN/m^2	Maximum shear stress
τ_{f}	kN/m^2	Shear strength at failure
τ_{m}	kN/m^2	Mobilised shear strength
τ_{xz}	kN/m^2	Shear stresses present in the x - z plane
τ_{yx}	kN/m^2	Shear stresses present in the x - y plane
τ_{yz}	kN/m^2	Shear stresses present in the y - z plane
ϕ'	$^\circ$	Effective angle of friction
ϕ_{u}	$^\circ$	Angle of friction for undrained total stress analysis ($= 0^\circ$)
ψ	$^\circ$	Dilatancy angle

Abbreviations

Symbol	*Explanation*
DPA	Dynamically Penetrating Anchors
DSS	Directi Simple Shear Test
ESP	Effective Stress Paths
FEM	Finite Element Method
FPS	Floating Production System
FPSO	Floating Production Storage and Offloading
GBS	Gravity Base Structure
HV	Horizontal - Vertical
MC	Mohr - Coulomb failure criterion
MODU	Mobile Offshore Drilling Platform
NC	Normally Consolidated
NGI	Norwegian Geotechnical Institute
OTRC	Offshore Technology Research Center
SEPLA	Suction Embedded Plate Anchors
SS	Soft Soil constitutive model
SPAR	Seagoing Platform for Accoustic Research
TSP	Total Stress Paths
TXC	Triaxial Compression Test
TXE	Triaxial Extension Test
TLP	Tension Leg Platform
UWA	University of Western Australia

Chapter 1

Introduction

In the contemporary era, one of the major issues faced by the world is the constantly increasing demand of energy. As the main resources of the world's energy are oil and gas deposited in the offshore environment, a remarkable advancement in the offshore geotechnical engineering field has been observed over the past decades. Although these resources are abundant, especially in deep waters, their extraction in offshore conditions is challenging and requires scientific research. In this industry, anchoring systems are essential for the stabilisation of the offshore floating platforms.

In particular, suction anchors are increasingly deployed in order to stabilise and connect the floating platforms to the seabed. In this context, geotechnical engineering aims to secure that the anchors are able to withstand horizontal - vertical (HV) loads coming from the inclined loading imposed by the mooring lines. The presence of torsional loading is often a common phenomenon that stems from imperfections during installation. In this case, the line of force action does not pass through the vertical axis of the anchor, leading to the so-called misalignment.

The main aim of this research is to investigate and quantify the influence of torsional loading on the bearing capacity of suction anchors. In particular, light is shed on the bearing capacity of misaligned suction piles that are embedded in clay through the comparison of three distinctive numerical approaches.

1.1 Research objectives

Finite element modelling is the most convenient contemporary method employed nowadays for the prediction of the bearing capacity of suctions anchors. The numerical representation of this physical problem necessitates several simplifications and assumptions regarding the soil behaviour and the soil - structure interaction. The main purpose of this study is to reveal if simplifying aspects of the problem for numerical convenience is towards safety by comparing the preliminary results of a benchmark study [39] with a more complicated and a simpler numerical approach of the same problem.

The first objective of this research is to investigate whether the bearing capacity of misaligned suction anchors resulting from a numerical analysis that follows a total stress approach (TSA) is comparable to the anchor capacity stemming from an analysis that follows an effective stress approach (ESA). For this purpose, a research is carried out about the most appropriate calibration of the constitutive soil model that reflects the soil conditions of the benchmark study and the potential failure mechanisms that develop while loading.

The second objective of this study involves a research on the prediction of the bearing capacity of a misaligned suction anchors in clay by a simplified two dimensional finite element software that simulates the misalignment effect with a reduction of the soil -

anchor interface strength. Hence, the performance of this numerical tool can be evaluated with the presence of torsional loading around an anchor's central axis that stems from the misalignment effect.

1.2 Methodology

In order to achieve all the objectives described in the previous section, finite element models involving misaligned suction anchors founded in clay were created within two finite element softwares, Plaxis 3D and SPCalc. The numerical analyses carried out with the help of these numerical tools are equivalent to the analyses conducted by the benchmark study of this research. This preliminary study includes several anchor loading scenarios and provides undrained horizontal - vertical (HV) interaction diagrams for three length - to - diameter ratios ($L/D = 1.5$, 3 and 6) and a whole range of misalignment angles from 0° to 90°.

The first part of this comparative study aims to unveil the similarities and dissimilarities between an undrained effective (ESA) and a total stress analysis (TSA) of this specific problem within Plaxis 3D. For this purpose, the finite element models created for the benchmark study, which undertakes a TSA, were modified accordingly to involve the presence of the water and the generation of (excess) pore water pressures during undrained loading. In this context, a Cam - clay constitutive type model, known as the Soft Soil model, is adopted for the current effective stress analysis in contrast to the benchmark study that embraced a simplified Tresca failure criterion. The proper comparison between the two approaches has as a prerequisite an appropriate calibration of the new soil model to represent the soil conditions of the benchmark study under different loading scenarios. A number of calibrations were realised with an emphasis to capture the distinctive failure mechanisms observed under different types of loading. Thus, HV interaction diagrams are derived and compared for 5 calibrations, three aspect ratios (L/D =1.5, 3 and 6) and two misalignment angles ($\beta = 0^\circ$ and 10°)

The second part of this comparative research focuses on the investigation of strengths and weakness involved in the adoption of a simplified two dimensional approach of the same problem for numerical convenience. For this reason, the special purpose geotechnical tool, named SPCalc, is used that was developed in order to calculate the bearing capacity of suction anchors accounting for 3D effects. In this approach, misalignment is modelled through the reduction of soil - anchor interface resistance. Numerical calculations were carried out with special focus to reflect the conditions of the benchmark study [39] with respect to anchor geometry, loading methods, soil conditions and soil - structure interaction. Hence, HV interaction diagrams are derived and compared with this preliminary study for three length - to - diameter ratios ($L/D = 1.5$, 3 and 6) and three misalignment angles ($\beta = 0^\circ, 5^\circ$ and 10°).

1.3 Structure of the report

The present report consists of the following main sections covering the basic topics of this MSc thesis.

Chapter 2 provides a brief overview of the various types of offshore geotechnical applications and focuses on the description and presentation of the design principles of suction anchors under vertical, horizontal and combined loading. It also introduces the significant effect of torsional loading on the suction piles due to misalignment.

Chapter 3 elaborates on the current numerical approaches of the bearing capacity of misaligned suction anchors in clay and reveals their most important features and the incentives that triggered their realisation.

Chapter 4 focuses on the presentation of the numerical models created within Plaxis 3D and provides details concerning the essential calibrations of the currently adopted constitutive model. Additionally, it discusses the numerical results and makes respective comparisons with the benchmark study.

Chapter 5 outlines the basic principles that are adopted by SPCalc and presents results that are followed by discussion and several relative comparisons with the three dimensional of the benchmark study.

Chapter 6 concludes the findings of this study and proposes further relevant research.

Chapter 2

Offshore Geotechnical Engineering

2.1 Introduction

This chapter provides an overview of the different types of contemporary offshore geotechnical structures that aim to support the oil and gas extraction activities. In the last century, the constantly increasing energy demands of the world led to a noteworthy evolution of the offshore geotechnical engineering field. This is evident if one considers that the first offshore platform was installed in 1947 and, nowadays, more than 7.000 offshore platforms operate worldwide. Furthermore, not only the number of the offshore platforms has rapidly increased, but also the operating depths have remarkably expanded. In particular, during the 1970s, the majority of platforms was installed in less than 50 meters depth, whereas, nowadays, operations at "ultra-deep water" of 1.500 meters depth are regarded as feasible as pointed out by [35]. Figure 2.1 depicts the significant development that the offshore industry has gone through over the past years.

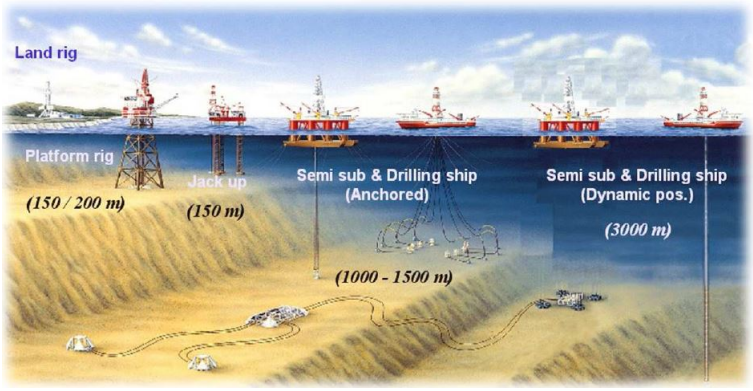

Figure 2.1: Evolution of the operational depths of offshore field [43]

The technical and operational complexity of developing a structure in the offshore environment is an order of magnitude greater than for onshore applications. The harsh offshore environmental conditions require the foundation of the offshore structures to be able to withstand large amplitude loads coming from the wind, ice, sea currents and waves, as well as loads resulting from the unpredictable geological conditions. As offshore geotechnical site investigations are considered expensive, significant uncertainty governs the design of offshore constructions.

The geotechnical applications constructed offshore play a crucial role for the foundation and anchoring of the floating facilities. Following a brief summary of the types of offshore geotechnical constructions, attention is drawn to the types of anchoring systems. As suction anchor piles founded in clay is the main topic of this research, they are discussed

thoroughly with special focus on the existing ways of predicting their operational bearing capacity under different loading scenarios. As revealed by the relevant literature review, horizontal (H) - tensile (V) interaction diagrams are the most convenient way to evaluate the ultimate bearing capacity of suction anchors under combinations of loadings. Finally, the issue of misalignment effect is addressed and reference is made to respective past studies that disclose its non-negligible impact on the overall anchor capacity.

2.2 Types of offshore geotechnical applications

In recent times, several types of offshore geotechnical applications were developed and several more that were improved. The majority of these structures are constructed for the foundation and anchoring of offshore platforms and floating drill units. All of them can be divided in five major categories that are presented in this section. The most important characteristics of these categories are reported. As far as the anchoring systems are concerned, a whole different section follows with their description as they are the main subject of research of the current thesis.

2.2.1 Shallow foundations

Offshore shallow foundations are bigger than the foundations that are constructed onshore. This is attributed to the fact offshore foundations have to support larger structures in challenging environmental conditions that impose large moments on them. The development of offshore foundations was initiated in the Golf of Mexico, where soft clays are present, and spread to the North Sea, where dense sands are found. Depending on the soil conditions and their use, different alternative applications of shallow foundation have been developed over the years and a number of them can be seen in Figure 2.2. However, all of them share one common characteristic having an embedment depth to foundation diameter ratio less than one.

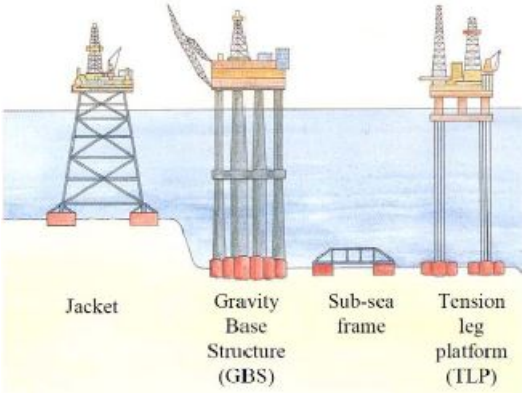

Figure 2.2: Applications of offshore shallow foundations [34]

The types of offshore shallow foundations be divided into three main categories as listed below.].

- Gravity based foundations

  According to [35], the first gravity based platform was constructed in the North Sea in 1973. This type of foundations are large concrete gravity bases that support offshore platforms as shown in Figure 2.2. As stated by [35], the most common characteristic of these structures is their huge weight and size, which are the features that make them able to tolerate the big lateral and moment loading that originates from the

environmental conditions. To further enhance their stability and transfer the loads deeper in the soil, skirts are often employed on them. Their length depends on the soil conditions expected on the site.

- Bucket foundations

  Bucket foundations, or caissons, are mainly constructed for the support of jackets, wind turbines and deep water manifolds as depicted in Figure 2.2. They are permanent or temporary constructions and are manufactured either from concrete or steel. They have a cylindrical shape and they are closed at the bottom and open at the top. These hollow structures are also used as anchors for floating platforms, which are discussed separately in section 2.2.5 as their bearing capacity is studied extensively in the context of this study.

- Spudcans

  Spudcans are also a permanent type of shallow foundation that are used for the support of mobile drilling rigs and are presented in more detail in section 2.2.3.

2.2.2 Piled foundations

Deep piled foundations are most preferable in comparison to shallow foundations in the case where soft soils are present close to the seabed. Due to their great length, they can sustain high lateral loads without sliding. Offshore pile foundations can be found in a variety of diameters that primarily relies on their actual application. For instance, piles with diameters of approximately 0.76 meters are used for the support of wellhead conductors, while piles with diameters of around 4 meters are suitable for monopiles of offshore wind farms. Currently, they are also extensively used for the foundation of steel jacket structures with diameters lying in the aforementioned range. In Figure 2.3, an example of a jacket structure is depicted.

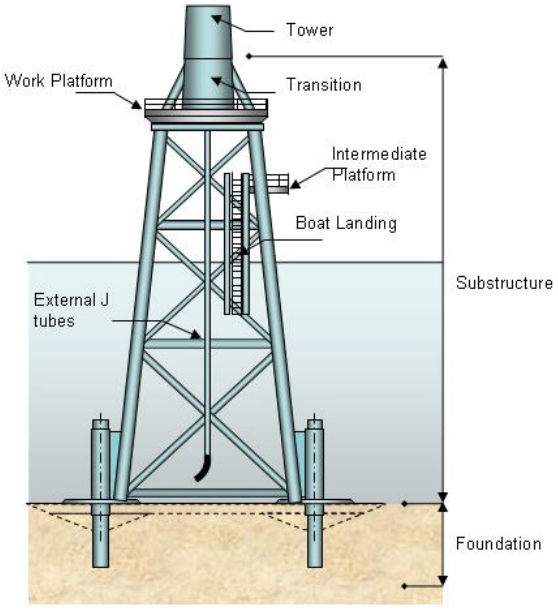

Figure 2.3: Deep piled foundation for the support of a steel jacket structure [50]

The length of the piles is diverse and hinges on the size of the structure to be supported, the magnitude of the environmental loads and moments expected . as well as the geological conditions encountered on site. As published by [32], the tallest offshore pile structure ever built is situated in the Golf of Mexico. It is 529 meters high and is constructed in

412 meters of water depth. Twenty eight piles were installed for the foundation of this outstanding construction that have a diameter of approximately 2 meters and a length of 165 meters.

Piled foundations are divided in two categories based on their construction method.

- Driven steel piles

  This type of piles are steel cylindrical piles that are open at the bottom. Their installation aims to assist the temporary seabed support of anchor piles. [34] notes that, currently, they are installed by being pushed into the soil by hydraulic (deasel or steam) hammers that are designed to work underwater.

- Drilled and grouted piles

  The offshore piles of this category are made of steel and have a turbular shape. However, they are placed into an already existing grouted hole as described by [34]. The additional procedure of drilling a hole constitutes them a more expensive and time consuming solution than driven piles.

Evidence from a wide number of studies, including [31] and [33], indicates that there has been an extensive research concerning the prediction of the bearing capacity of offshore piles under lateral loading in diverse soil conditions. Moreover, [35] has drawn attention to the fact that the axial and horizontal pile capacity is determined through guidelines that comprise empirical correlations. As a consequence, a number of assumptions and extrapolations are necessary for the prediction of their bearing capacity. Section 2.3.1 reviews in detail the topic of vertical and lateral capacity of the offshore suction piles that are installed in soft clays and studied thoroughly under the scope of this research.

2.2.3 Footings for Jack-up platforms

Jack-up platforms constitute the latest advancement of mobile offshore drilling units (MODU). Jack-ups play a fundamental role in the offshore industry as they are a flexible, stable and relatively economical solution. What distinguishes them from the rest of offshore foundations is their capability to be self installed. The first jack-up rigs were installed in 1954. Nowadays, more than 540 jack-ups operate worldwide. They are found in different sizes and their capabilities vary significantly. Nevertheless, the general trend for these units is to enlarge and become more expensive as the drilling and marine capability increases. Today, they can be used until 150 meters of water depth.

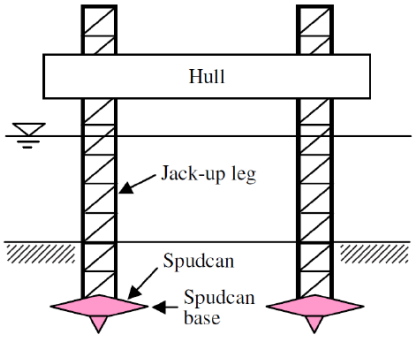

Figure 2.4: Jack-up platform with spudcan foundation [29]

Figure 2.4 shows a schematic overview of a jack-up rig after its installation. They are composed by a buoyant hull and a set of (usually 3) independent legs. Due to the buoyant hull, the structure can float easily at the point where it will be installed. What is

remarkable about these units is the procedure of their self-installation. The legs, that are fitted on the hull, can be lowered and have the ability to penetrate into the seabed. Once this step is accomplished, the hull, which is supported by the legs founded on the seabed, is raised to the required elevation above the sea surface.

The footings of a jack-up rig, also widely known as spudcans, are an integral part of this set up. As noted by [34], spudcans have a special shape that could be described as a a shallow inverted cone with a sharp protruding spigot. Today, their diameter can be more 20 meters.

2.2.4 Submarine pipelines

The transport of oil and gas products between wells, in-field processing facilities and to shore is accomplished through a number of submarine pipeline networks as depicted in Figure 2.5. Offshore pipelines are a vital part of the offshore industry.nThe geological hazards linked to the submarine pipelines are usually initiated from the problematic condition of the seabed indicated by the presence of faults and sand waves, the occurrence of rock fall, debris flows and soil liquefaction, as well as the seismic activity. To avoid all the aforementioned issues, detailed and extensive geological site investigations are required along the path designed to be followed by the offshore pipelines. Thus, the soil - structure interaction can be determined with greater accuracy.

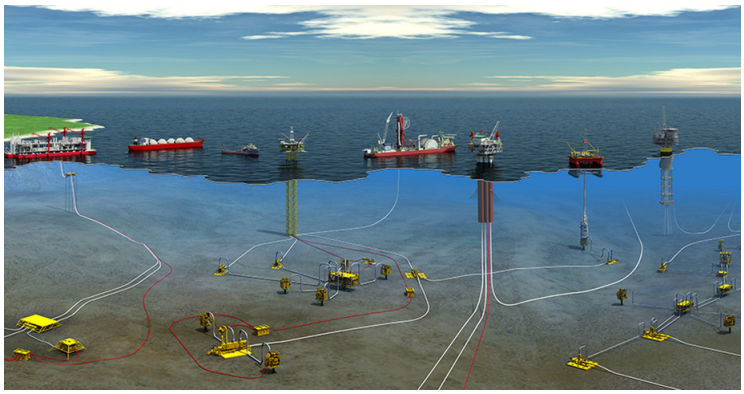

Figure 2.5: Submarine pipeline networks [21]

The pipes can be assembled either onshore or offshore and, for both cases, they are laid on the seabed from a vessel, using an S-lay, J-lay or reel lay configuration. Today, as mentioned by [35], pipelines are divided in the two subsequent categories that are linked to the material from which they are manufactured.

- Rigid pipelines

  This category of pipelines are made from steel. in order to be protected from the harsh environmental conditions during operation, they consist of layers of internal and external ncoating. In this way, effects from corrosion and abrasion are minimised. Moreover, thermal insulation and weight for improved stability is added to them. Their diameter ranges from 0.1 to 1.5 meters.

- Flexible pipelines

  This type of pipelines are manufacture from metal and polymer as wound strips of metal are placed in between layers of polymer. This layered structure makes them a more expensive solution than rigid piles, but their flexibility leads to a rapid lay. The diameters available fluctuate between 0.1 and 0.5 meters.

2.2.5 Anchoring Systems

Anchoring systems are essential for the stabilisation of buoyant facilities. They are composed of mooring lines of steel wire or synthetic ropes that are linked to the seabed through anchors. There are several configurations in which this connection can be accomplished and this is primarily dependent on the type of the floating platform to be supported. In Figure 2.6, there is an overview of buoyant platforms used nowadays. As it can be seen, mooring lines can be catenary (FPS), taut or semi-taut (FPSO) and vertical (SP), which all end to anchors installed in the seabed.

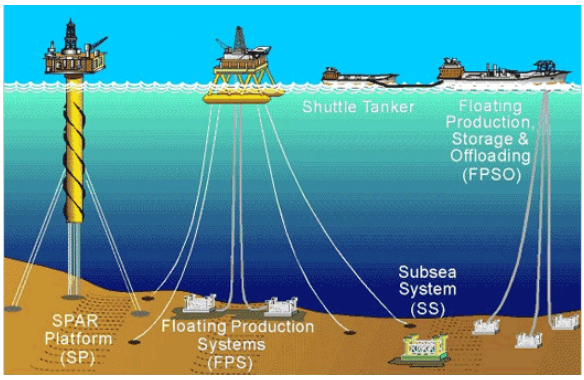

Figure 2.6: Offshore floating platforms [5]

Currently, there is a variety of anchors used to secure the stability of floating production platforms, which can be divided in surface (or gravity) and embedded anchors. The first category includes box, grillage and berm anchors. This type of anchors have limited capacity and are only suitable for shallow waters as their stability primarily depends on their weight and and the base friction generated between the anchor and the seabed. In extreme cases, where significantly higher capacity is needed for the support of a buoyant platform, embedded anchors are preferred. The main types of embedded anchors used in practice are listed below and presented in Figure 2.7.

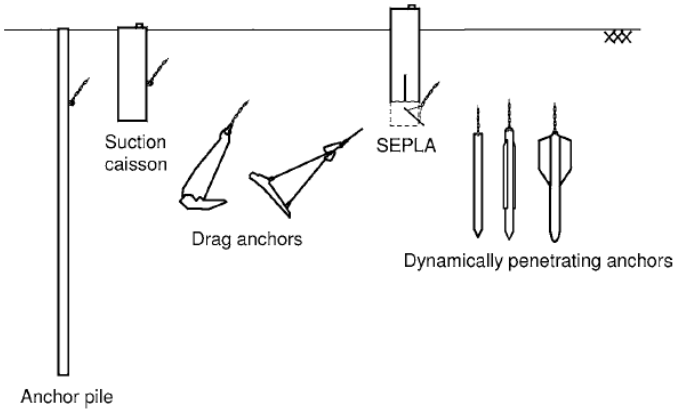

Figure 2.7: Types of embedded anchors [35]

Anchor piles

Anchor piles have the highest vertical and horizontal capacity of all the embedded anchors. They are long cylindrical hollow structures made of steel with an aspect ratio of 60 approximately. They are installed in the same way as deep piled foundations for fixed bottom structures as described in Section 2.2.2.

Suction - installed anchors

Suction - installed anchors can be described as large steel cylindrical structures that are open at the bottom and closed at the top. What distinguishes them from the rest of the anchors is the special way in which they are installed. Initially, the cap is vented and the first part of the penetration is accomplished only through the self weight of the structure. As a second and final step, a pump is connected in the top cap of the caisson and the remain penetration is achieved through the application of suction. As water is pumped out of the anchor, a downward pressure is created at the top of the anchor that forces it into the seabed.

The loads carried by the mooring are applied to the anchor on the padeye, which is attached to the side of the anchor. It is positioned at a depth of approximately 70 per cent of the length so that the bearing capacity of the anchor is maximised. In this way, the pile translates horizontally and does not rotate.

Suction - installed anchors have diameters between 3 and 8 meters and they are divided in two categories depending on their aspect ratio. When the length to diameter ratio, L/D, is less close to 1, then they are called suction caissons. When the length to diameter ratio is higher, but less than 6, they are called suction piles. The suction anchors studied in this research also belong to this category and a typical example of them is illustrated in Figure 2.8.

Figure 2.8: Suction pile [5]

Drag anchors

As depicted in Figure 2.7, drag anchors are composed of a broad fluke that is connected to a shank. They are regarded as an evolution of the conventional ship anchors. They are pushed in the seabed and rotation of the fluke happens after the mooring force is applied.

Suction embedded plate anchors (SEPLA)

This type of anchors is illustrated in Figure 2.7. They are installed in the same way as the suction installed anchors described previously. They also have a similar shape with the suction anchor apart from the fact that a plate anchor is slotted into their toe. The anchor is installed and then uninstalled following the same reverse procedure of pumping but the plate anchor stays in the ground and is rotated after the application of the chain load.

Dynamically penetrating anchors

This type of anchor is still under trials. It is interesting to note that they are developed so that they can be self-installed in the seabed under free fall. For this reason, they are designed to have the shape of a rocket.

2.3 Suction anchor piles

With the term suction piles, one refers to deep foundation units that are installed with the application of suction and have a length to diameter ratio more than one. These slender structures are the main subject analysed under the scope of this study. Therefore, special attention is given to the aspects that govern their operation and the prediction of their ultimate capacity under inclined and torsional loading.

2.3.1 Operation of suction piles

The safe operation of suction piles hinges principally on the accurate prediction of the vertical and horizontal capacity. It was not until recently that formal design principles were established. Nowadays, documented installation and capacity design methods are provided by [2] and [4]. The aforementioned methods are based on limit equilibrium analyses. It is a common practice that these methods are often supported by numerical analyses involving finite element computations. Additional information concerning the methods used for the calculation of vertical and horizontal capacities are elaborated in the following paragraphs.

Vertical capacity

The uplift capacity of a suction pile is crucial when suction anchors support TLP structures where vertical mooring is employed (Figure 2.2). There is a number of past studies ([19], [42], [3], [49], [17], [13]) that reveal the existence of three potential "pull-out" mechanisms, which are schematically presented in Figure 2.9 and described in the subsequent paragraphs. At this point, it should be clarified that the weight of the caisson always enhances the vertical capacity but it will not be taken into account in the calculation of V_{ult} as only the investigation of geotechnical terms is meaningful to this study.

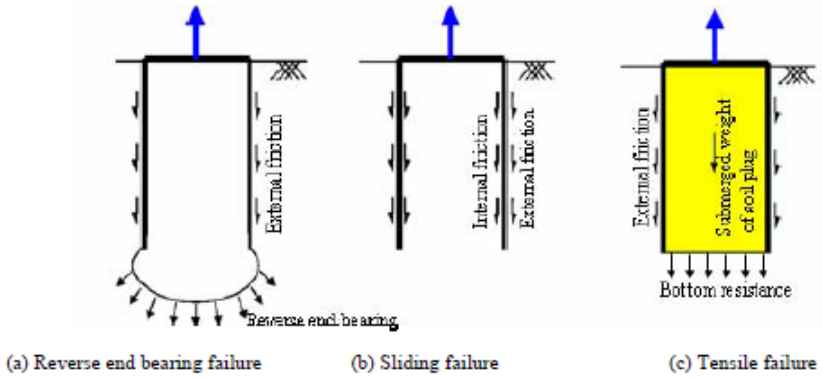

Figure 2.9: Failure modes for vertical resistance of suction piles [45]

a) Reverse end bearing

The characteristic of this failure mechanism is that the top cap is sealed and passive suction is generated inside the caisson. As a consequence, the soil plug is forced to move vertically along with the caisson and, as the caisson displaces vertically, inward soil flow takes place at the bottom of the caisson. The calculation of the vertical capacity V_{ult}, as shown in Equation 2.1, involves the sum of two distinctive components, including the external shaft friction and the reverse end bearing.

$$V_{ult} = A_{se}\ \alpha_e\ \overline{s}_{u(t)} + N_c\ s_u\ A_c \tag{2.1}$$

The reverse end bearing is expressed through the end bearing factor, N_c, that can be determined analytically, numerically or experimentally. Many researchers focused on the determination of N_c values. [45] provides an overview of the relevant past studies. Some of them are summarised in the table that follows. It should be made clear that direct comparison cannot be made between these studies due to variations in soil type (overconsolidation ratio, soil strength profiles etc) and length to diameter ratio of the caissons. As proposed by [37], a value of N_c equal to 9 is widely considered as an appropriate and conservative solution.

Table 2.1: End bearing factor, N_c, from several studies

Authors	N_c [-]	Type of study
[37]	9	analytical (upper bound approach)
[45]	10.14 - 10.48	numerical (finite elements)
[39]	4.61 - 12.41	numerical (finite elements)
[27]	9 - 12	experimental (centrifuge tests)
[16]	13.8	experimental (centrifuge tests)
[20]	8.1 - 10.6	experimental (1-g laboratory & centrifuge tests)

b) Sliding failure

Sliding failure occurs when no passive suction is applied at the top cap of the anchor. The suction anchor is pulled out of the soil and is no longer considered attached to the soil plug. Consequently, the uplift capacity consists of two separate components, referring to the external shaft friction and the internal shaft friction, as expressed by Equation 2.2.

$$V_{ult} = A_{se}\ \alpha_e\ \overline{s}_{u(t)} + A_{si}\ \alpha_i\ \overline{s}_{u(t)} \tag{2.2}$$

c) Tensile failure

Tensile failure takes place when no passive suction is applied at the top cap of the anchor. In contrast to the sliding failure, the caisson moves together with the soil plug out of the seabed when it fails. The external wall friction and the soil plug weight comprise the vertical capacity as the mathematical formulation of Equation 2.3 reveals.

$$V_{ult} = A_{se}\ \alpha_e\ \overline{s}_u + W'_{plug} \tag{2.3}$$

The parameters implemented in the Equations 2.1, 2.2 and 2.3 are explained below.

- A_{se} and A_{si}: external and internal shaft surface area, [m^2]
- A_e: external cross-sectional area, [m^2]
- α_e and α_i: coefficient of external and internal shaft friction (i.e. steel to soil), [-]
- N_c: reverse end bearing factor [45], [-]
- s_u: representative undrained soil shear strength at tip level, [kN/m^2]
- $\overline{s}_u$: average undrained soil shear strength over penetrated depth at time t after installation, [kN/m^2]
- W'_{plug}: effective weight of the soil plug, [kN]

Finally, it is important to note that the reverse end bearing mechanism is the most common failure mode to be encountered in the application of suction anchors and, therefore, this type of failure will be considered for calculation of bearing capacity.

Lateral capacity

Suction piles are usually used as anchors for catenary mooring lines that support floating production facilities. Figure 2.10 illustrates schematically the attachment point and the direction of the load coming from the chain. As cited by [37], a load is applied at the padeye with a loading angle that deviates around 10° from the horizontal direction in the case of catenary mooring. As far as taut wire moring lines are concerned, the load inclination is expected to be 20° approximately.

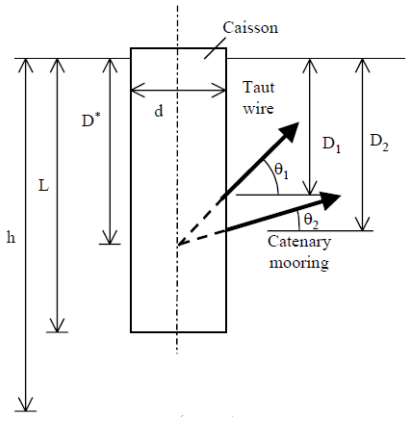

Figure 2.10: Suction anchor load due to taut wire or catenary mooring [37]

The failure mechanism that develops when suction anchors are subjected to horizontal loading depends significantly on the position of the padeye. Past studies conducted by [31], [37] and [6] unravelled two complex potential failure mechanisms that are demonstrated in Figure 2.11. The first one (2.11a) involves a conical wedge that forms close to the surface [31] and a flow region below this wedge [36]. The second lateral collapse mechanism (2.11b) consists of a rotational soil flow around the bottom of the anchor [37].

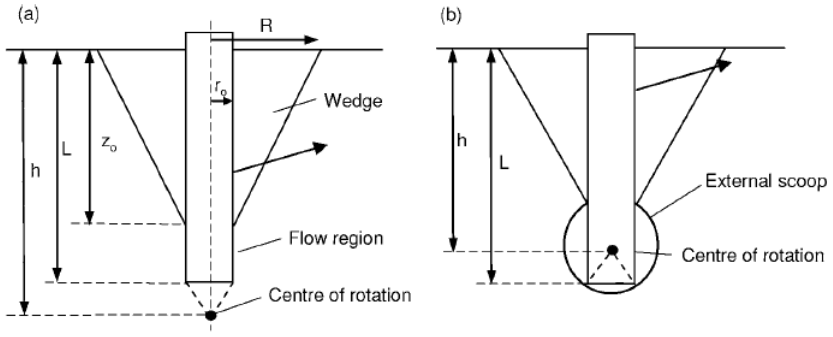

Figure 2.11: Failure mechanisms for horizontal resistance of suction anchors (a) conical wedge and flow region and (b) external base rotational scoop [35]

The works by [38], [1] and [14] report that the horizontal capacity of an anchor is maximised when the anchor does not rotate due to the horizontal loading but only translates as a rigid body. Following the work of [2], it is suggested that for normally or over - consolidated clays, where the shear strength increases with depth, the depth of the padeye

to achieve the maximum horizontal capacity is 0.65 - 0.7 of the pile embedded length. This effect of padeye on lateral capacity is also apparent in Figure 2.12 that shows results of anchors loaded with an angle of 30° within a normally consolidated strength profile [2].

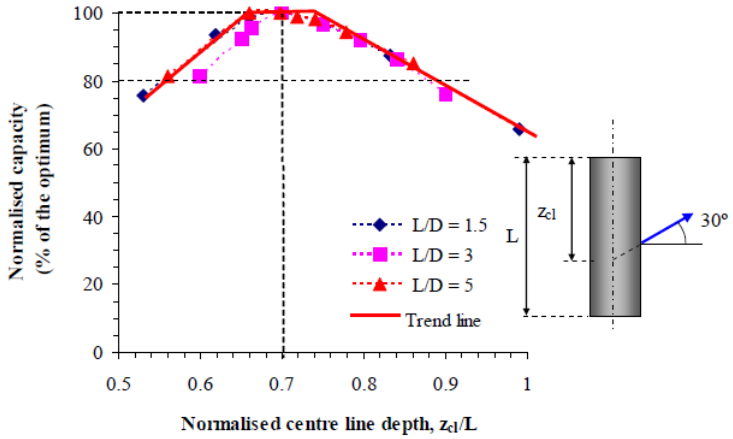

Figure 2.12: Effect of padeye depth on horizontal capacity [45]

[38] suggests that, if the anchor is assumed to translate as a single "black box" and the padeye is located at the optimum depth, the ultimate lateral capacity can be approximated as:

$$H_{\text{ult}} \approx L \cdot D_{\text{e}} \cdot N_{\text{p}} \cdot \overline{s}_{\text{u}} \tag{2.4}$$

Where L and D are the embedded length and diameter of caisson, N_{p} is the lateral bearing capacity factor (different to N_{h}) and $\overline{s}_{\text{u}}$ and undrained shear strength averaged over the penetration depth.

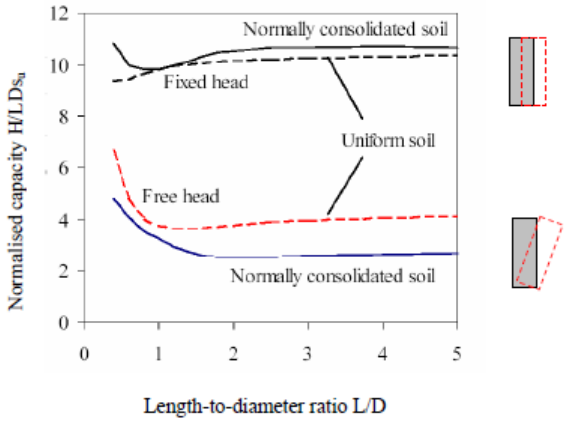

Figure 2.13: Effect of soil strength profile and aspect ratio on N_{p} [25]

The lateral bearing factor N_{p} depends on several factors and, especially, on the position of the padeye, as well as the soil strength profile. In Figure 2.13, there is a graph presenting anchor capacity results obtained by [25] for anchors loaded at the optimum depth and at the mudline for different aspect ratios and soil strength profiles.

However, a more recent study by [45] proposes that the lateral bearing capacity should be calculated through the following equation that involves two terms referring to the the resistance provided by the soil around the shaft (Q_{s}) and the base friction or adhesion (Q_{b}).

$$H_{\text{ult}} = Q_{\text{s}} + Q_{\text{b}} = DN_{\text{h}} \int_0^L s_{\text{u}}(z)\, dz + \frac{\pi D^2}{4}\, s_{\text{u,tip}} \tag{2.5}$$

Where N_{h} is a lateral bearing factor reflecting the magnitude of the normalised horizontal capacity and $s_{\text{u,tip}}$ is the undrained shear strength of the soil at the tip of the anchor. [45] found that N_{h} depends on the length to diameter ratio of the caisson, as well as the adhesion factor, and fluctuates between 8.49 and 11.01.

Inclined capacity

In the challenging and harsh offshore environment, the loading conditions of suction piles are not only described by uniaxial vertical or uniaxial horizontal loading. As pointed out by [35], the ultimate bearing capacity of an anchor should explicitly consider the interaction of all the load components acting on it.

Past studies by [37], [51] and [40] demonstrate that when horizontal and vertical loads act on the anchor simultaneously, the pure horizontal and vertical capacities are reduced. Nowadays, the most convenient way to model this phenomenon is through interaction diagrams, or failure envelopes, in horizontal, horizontal, torsional (V, H, T) load space. Any load combination that lies within the failure locus is safe for the structure.

These aforementioned failure envelopes can be determined experimentally, analytically or numerically. Experimental determination involved centrifuge tests. Analytical determination involves upper boundary and lower boundary plasticity solutions. Numerical determination involves finite element calculations as the approach adopted in the context of this study.

In Figure 2.14, HV failure envelopes coming from four different finite element capacity calculations are presented that show the actual influence of the different loading combinations on the bearing capacity of the anchor. These results were obtained from the numerical analyses of a suction anchor of 5 meters diameter that was founded in normally consolidated clay and was loaded at the padeye with an angle varying from 0° to 90°. The sources of the depicted resutls include the Norwegian Geotechnical Institute (NGI) that used the in house code BIFURC 3D, the Offshore Technology Research Center (OTRC) and the University of Western Australia (UWA) that used ABAQUS (HKS, 2002) and Plaxis 3D Foundation version 2.2 results.

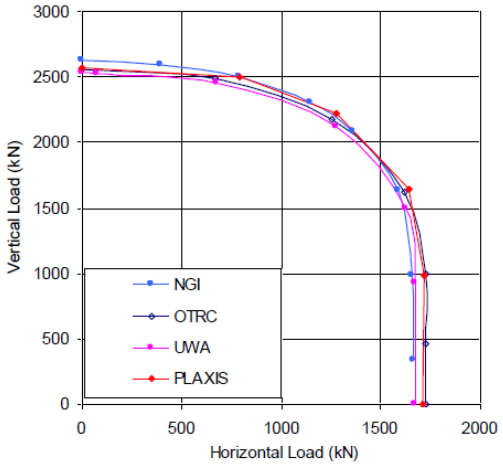

Figure 2.14: Failure envelopes of suction caisson for inclined loading [18]

[35] correctly states that the shape of a failure envelope depends on a variety of conditions, including whether failure takes place undrained or drained, the degree of shear

strength heterogeneity, foundation – soil interface roughness and foundation shape andembedment. [45] claims that the normalised failure envelope for a caisson with a certain aspect ratio that is subjected to inclined loading can be expressed through a simple elliptical curve fit defined by Equation 2.6. This elliptical curve involves the coefficients, a and b, that govern the shape of the ellipse.

$$\left(\frac{H}{H_{\text{ult}}}\right)^{\text{a}} + \left(\frac{V}{V_{\text{ult}}}\right)^{\text{b}} = 1,\ a = \frac{L}{D} + 0.5,\ b = 4.5 - \frac{L}{3D} \tag{2.6}$$

2.3.2 Misalignment effect

It has been observed that anchors founded in the seabed are not perfectly aligned with the production facilities that aim to support. This is due to a rotation taking place in the horizontal plane during installation. [28] claims that this can be attributed to the difficulty involved in the precise control of installation due to lack of anti-twist mechanism in the rigging system (especially for long piles with a length to diameter ratio more than 6). Misorientation might also be caused by subsea currents that act on the pile forcing it to rotate as shown in Figure 2.15.

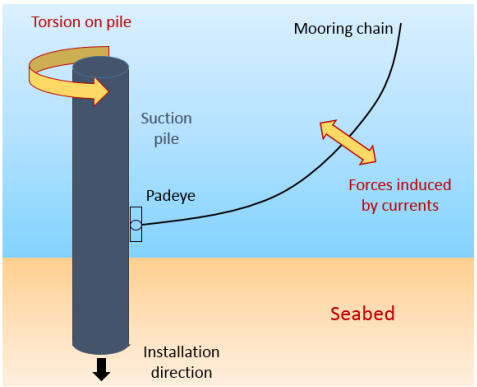

Figure 2.15: Torsion induced by sea currents on the suction pile

Nowadays, it is common practice that, in cases where the observed rotation of the pile after installation exceeds the typical allowable rotation of 7.5°, piles have to be extracted. In this way, catastrophic consequences that might result from the induced torsion are prevented. At this point, it is also interesting to note that significant torsional loading might also be observed when suction anchors are used to support tall structures that are subjected to large eccentrically applied forces, such as the wind turbines [47]. Therefore, torsional loading is a parameter that should never be neglected during the design of suction anchors.

Important research has been carried out on the undrained HV capacity of misaligned suction anchors. [7] presents a rigorous analytical solution for piles, with the help of the upper bound element method, predicting the pile - soil interactive performance under torsion, while [15] and [23] use a discrete element approach of the same problem in order to determine the (pure) torsional capacity of the pile. A finite element approach of the problem has been adopted by [46], [47] and [44] that investigated the undrained ultimate bearing capacity of suction piles under the combination of inclined and torsional loading. It is noteworthy that all of these studies reveal significant effects of misalignment on the HV capacity of suction anchors.

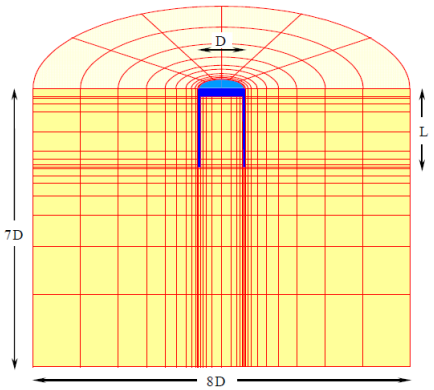

Figure 2.16: Finite element modelling of a suction anchor by [47]

The work of [47] involves displacement-controlled analyses of a suction anchor with $L/D = 2$, where a vertical or torsional displacement was applied to the foundation at the ground level, or a lateral displacement was applied at various locations along the skirt of the foundation below the ground level. The soil was modelled with a uniform undrained shear strength. A series of results obtained from this study were presented in the form of axial-torsional-lateral interaction diagrams as illustrated in Figure 2.17a. The results depicted propose that both vertical and horizontal capacities are influenced by the increase of misalignment. More precisely, an increase in rotation imposed at the top cap, leading to an increase in the torsion induced in the pile, makes the failure envelopes shrink and, therefore, bearing capacity decreases.

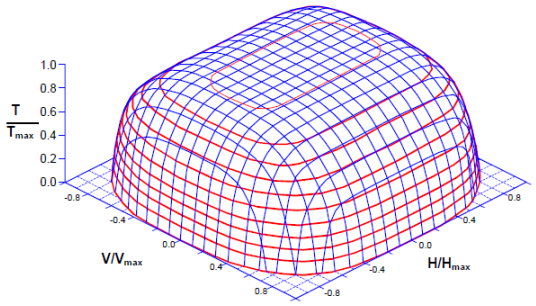

(a) Three dimensional failure loci in the non-dimensional VHT space

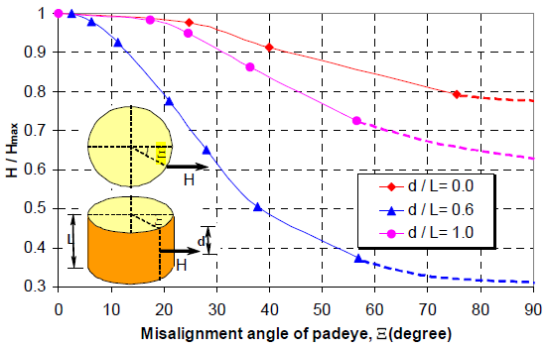

(b) Effects of padeye misalignment on the ultimate lateral capacity

Figure 2.17: Results of the 3D finite element approach adopted by [47]

Following the same study, it is also reported that the reduction of the horizontal capacity is a function of both the misalignment angle and the location of the padeye. A closer observation of Figure 2.17b unravels that the maximum reduction in the ultimate lateral capacity occurs when the torsional load is applied at a depth below the ground line that is equal to 60 percent of the anchor length.

[46] conducted 3D finite element parametric load - controlled analyses with anchors of varying aspect ratios that are founded in homogeneous soil. As far as the soil conditions are concerned, two alternatives were examined involving a uniform undrained shear strength, s_u and one increasing with depth. Additionally, as presented in Figure 2.18a, the capacity of the anchor was examined for two different load attachment points, one at the top of the anchor and one at the padeye at a depth of 70 percent of the anchor length. This study revealed that the torsion induced the padeye reduces both vertical and horizontal

capacity as depicted in Figure 2.18b.

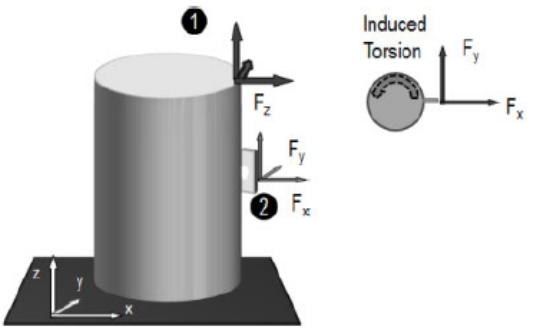

(a) Loading attachment points on the suction pile finite element model

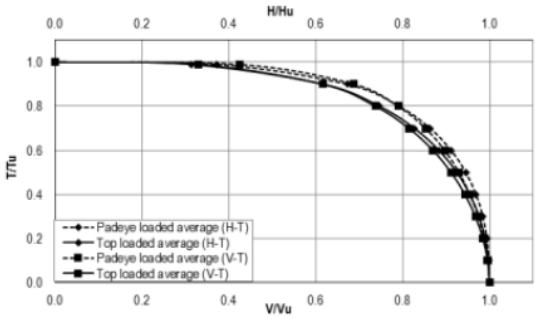

(b) HVT failure envelopes for two attachment points

Figure 2.18: 3D finite element approach adopted by [46]

Ultimately, it was proposed by the same author that the two subsequent equations can capture the effect of aspect ratio and load application point on the HT and TV capacities of anchors. The shape coefficients, m and n, are also provided in Table 2.2. The presented values are determined through the analytical interpolation of the numerical data with elliptical curves and averaged for all the aspect ratios and soil strength profiles.

$$\left(\frac{V}{V_{\text{ult}}}\right)^{\text{m}} + \left(\frac{T}{T_{\text{ult}}}\right)^{\text{n}} = 1 \tag{2.7}$$

$$\left(\frac{H}{H_{\text{ult}}}\right)^{\text{m}} + \left(\frac{T}{T_{\text{ult}}}\right)^{\text{n}} = 1 \tag{2.8}$$

Table 2.2: Averaged values for m and n coefficients [46]

Condition	Load application	m [-]	n [-]
V - T	Top	2.13	3.33
	Padeye	2.39	3.79
H - T	Top	1.82	3.61
	Padeye	1.79	4.71

A further investigation of the actual effect of misalignment on the undrained HV bearing capacity of suction anchors was attempted by [39] through the creation of a finite element model within Plaxis 3D. The most important aspects, findings and conclusions of this research are presented in Section 3.2 as it is the benchmark study of the current thesis. Following this recent approach of modelling misaligned suction anchors in clay, two additional numerical approaches are adopted and compared with the benchmark study. Important aspects that govern each one of these approaches are elaborated in the chapter that follows.

Chapter 3

Numerical analysis of misalignment effects

3.1 Introduction

The main objective of the current thesis is to approach the effect of misalignment from two additional perspectives. As a first step, the basic principles that govern the finite element modelling of suction anchors of the benchmark study are presented. In this way, it is made clear which aspects of the past research will be kept unchangeable in the analyses carried out for this study and which ones will be modified. Additionally, the motivations behind the new approaches will be unveiled.

The first approach of this problem involves the effective stress analysis of the misaligned suction anchors within Plaxis 3D. This method is considered to be very close to the prediction of the actual clay behaviour in contrast to the benchmark study that followed a simplified total stress analysis involving several assumptions about the soil behaviour. The second approach of this problem includes the two dimensional analysis of suction anchors within the finite element tool known as SPCalc including the investigation of misalignment. The main aspects of the numerical calculation procedure and modelling of misalignment of this software are presented so that the resemblances and discrepancies with the benchmark study are highlighted.

3.2 Benchmark study description

The MSc thesis study carried out by [39] constitutes the benchmark study of the current thesis research. This work involves the finite element modelling of misaligned suction anchors founded in clay. The numerical calculations were conducted with the use of Plaxis 3D Anniversary Edition. An effort to quantify the actual effect of torsion on the HV undrained ultimate capacity was made through the execution of several loading scenarios including horizontal, vertical and torsional loading within Plaxis 3D.

Three different suction anchors founded in homogeneous clay were analysed with the same diameter equal to 5 meters and three different lengths equal to 7.5, 15 and 30 meters. The numerical model was validated against already existing solutions established by [45] after the execution of displacement - controlled analyses.

3.2.1 3D FE modelling of suction anchors

In order to simulate each one of the suction anchors, two surfaces were created in Plaxis 3D. One cylindrical surface corresponding to the anchor shaft and one circular representing

the top cap. The weight of the anchor was neglected as the aim of the analyses was the computation of the geotechnical part of the anchor bearing capacity.

The suction anchor interfaces together with the soil plug volume were modelled as a rigid body with a reduced shear strength at the interface. Once, a rigid body is created in Plaxis 3D, the co-ordinates of a reference point have to be determined. This is essential as this is the only point at which loads/moments and/or displacements/rotations can be imposed on the rigid body and degrees of freedom can be specified.

In this case, the reference points of the soil plug and the anchor are chosen to be the same. Therefore, the soil plug behaves as being fully attached to the anchor and cannot move independently. Moreover, deformations of the nodes that belong to the anchor and the soil plug are not calculated during the numerical analyses and, thus, stresses remain unknown. Only contact stresses along the outer surface of the anchor shaft are available as an interface was employed. The reduction factor for the external shaft friction, R_{inter}, or adhesion factor, α, is assumed to be 0.65.

3.2.2 Total stress modelling of undrained clay behaviour

The most important aspects that influence the soil behaviour of the benchmark study are reported below. The suction anchors are founded in normally consolidated clay with undrained shear strength, s_{u}, increasing with depth. It was decided that soil behaviour would be simulated with the elastic - perfectly plastic Mohr - Coulomb model and the the variation of s_u with depth would be: $s_{\text{u}}(z) = 1.25z$. Undrained(C) drainage type is chosen which leads to a conventional total stress analysis with all parameters specified as undrained. The elastic stress - strain response of the constitutive model was defined through the undrained Young's modulus, E_{u}, which is proportional to the undrained shear strength: $500s_{\text{u}}$.

Setting the angle of friction, ϕ, equal to 0° and the cohesion, c, equal to the undrained shear strength, s_{u}, leads to an even more simplified failure criterion called Tresca failure criterion. Figure 3.1 illustrates two schematic overviews of the failure surface of this criterion in 2D and 3D space.

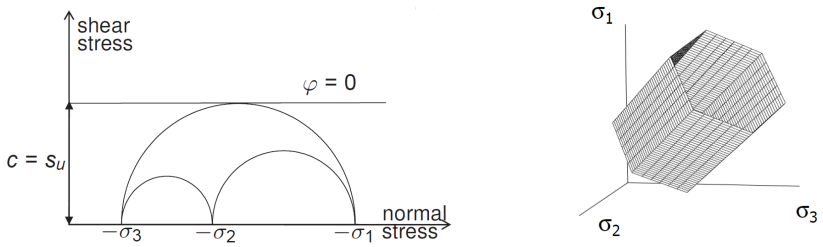

(a) 2D view (b) 3D view

Figure 3.1: Schematic overview of Tresca failure criterion in 2D and 3D space [11]

The analyses were conducted under undrained conditions by selecting the Undrained(C) option in Plaxis 3D. As a consequence, a total stress analysis is followed and only total stresses are calculated. Pore pressures and effective stress paths remain unknown. It should be highlighted that water is not present in the soil domain.

It is true that during an undrained analysis, no volumetric changes should take place. In order to make sure that volumetric strains are constrained in a this type of analysis, Poisson's ratio, ν_{u} was set equal to 0.495, and the dilatancy angle, ψ, has a zero value. Specifying $\nu_{\text{u}} = 0.5$ is avoided as it would result in the singularity of the stiffness matrix.

Additionally, since a total stress analysis is followed by the benchmark study, an initial total stress state is generated. Therefore, another assumption that was made for the numerical simulation of the offshore soil conditions of this problem is that the total lateral earth pressure coefficient, K_o^{tot} is equal to 1 as estimated by Equation 3.1. This assumption is based on the fact that, for deep water applications, pore water pressure (u) is dominant compared to the stresses coming from the soil overburden as depicted in Figure 3.2.

$$K_o^{tot} = \frac{\sigma_h}{\sigma_v} = \frac{\sigma'_h + u}{\sigma'_v + u} = \frac{\sigma'_h + \gamma_w(h_w + z)}{\sigma'_v + \gamma_w(h_w + z)} \approx \frac{\gamma_w(h_w + z)}{\gamma_w(h_w + z)} \approx 1 \tag{3.1}$$

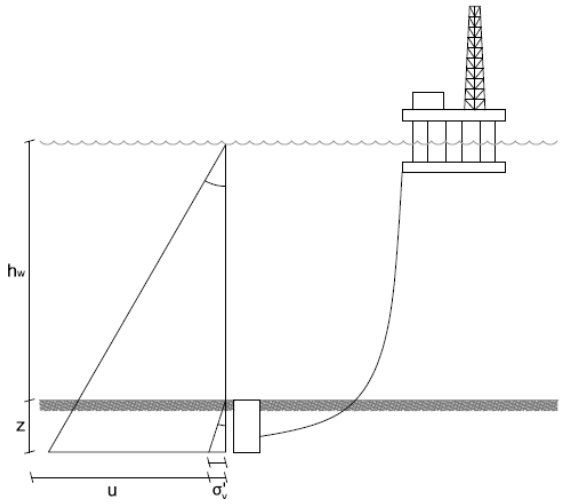

Figure 3.2: Schematic representation of offshore in situ stress state [39]

In order to verify whether this assumption has a significant influence on the results of the total stress approach regarding the undrained HV bearing capacity of suction anchors, additional analyses were conducted for the short anchor with a K_o^{tot} equal to 0.75. Figure 3.3 shows that the HV interaction diagrams coincide for both coefficients revealing that this assumption has no impact on the bearing capacity of the suction anchor.

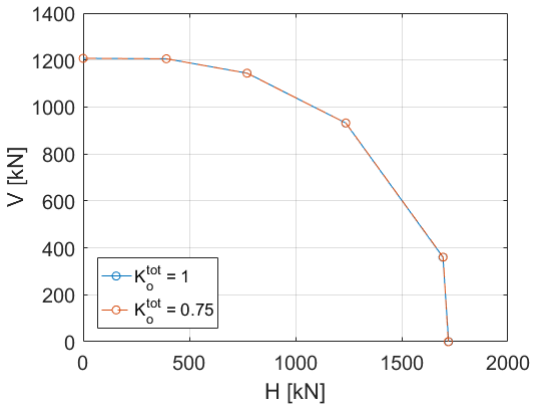

Figure 3.3: Comparison of HV failure envelopes for TSA using K_o^{tot} equal to 1 and 0.75

Finally, as noted by [35], it is generally acceptable that, in normally consolidated clays, gapping at the back side of the suction pile does not occur and, consequently, both wedges are formed at failure (Figure 2.11). This is considered to be true also for this analysis.

Table 3.1 constitutes a summary of the selected soil parameters of the benchmark study.

Table 3.1: Material properties of Tresca failure criterion

Parameter	Symbol	Unit	Value
Saturated unit weight	γ_{sat}	[kN/m^3]	16
Friction angle	ϕ	[°]	0
Dilatancy angle	ψ	[°]	0
Poisson's ratio	ν	[°]	0.495
Reference depth	z_{ref}	[m]	0
Undrained cohesion at z_{ref}	c_{ref}	[kPa]	0
Young's modulus at z_{ref}	E_u^{ref}	[kPa]	1
Undrained cohesion increment	-	[kPa/m]	1.25
Young's modulus increment	-	[kPa/m]	625
Lateral earth pressure coefficient	K_o^{tot}	[-]	1
Strength reduction factor	R_{inter}	[-]	0.65

3.2.3 Loading application methods

The creation of HV interaction diagrams was feasible after carrying out a series of numerical analysis within Plaxis 3D that involved loading scenarios with various loading angles, θ, in the vertical plane. The effect of misalignment was evaluated by conducting additional analyses for several misalignment angles, β.

The way in which the inclined loading was modelled is shown in Figure 3.4a. All the loads where applied at the padeye, which is located at the depth, z_p, that corresponds to 70 percent of the length of each anchor. . It is apparent that in order to model an inclined load (F), a vertical load (V) and a horizontal load (H) were applied at the anchor at the reference point (padeye).

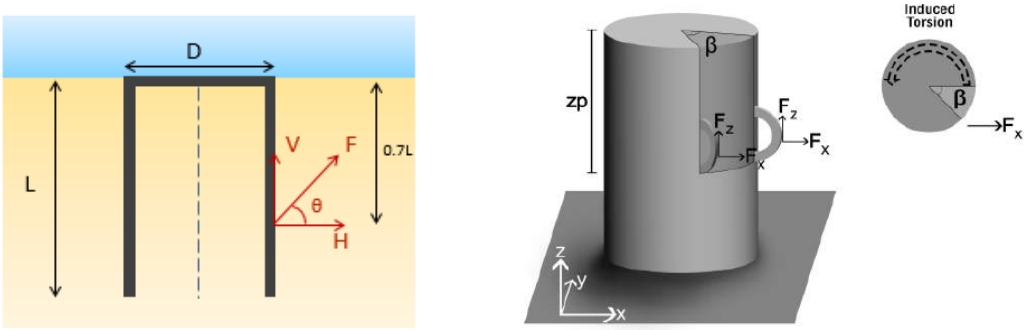

(a) Modelling of inclined loading

(b) Modelling of torsional loading [39]

Figure 3.4: Modellling of inclined and torsional loading scenarios in Plaxis 3D

Furthermore, Figure 3.4b depicts how the torsional loading was employed. To represent the real world scenario, where torsion is generated due to eccentric loading, the application of torsion is accomplished through a horizontal eccentric force on the anchor pile. This method was adopted by considering that a misalignment angle changes the load attachment point along the perimeter of the cylindrical shaft. Consequently, the projected force in the x-y plane always remains horizontal.

3.2.4 Relevant results

First of all, the results of this study revealed that the misalignment angle does not influence the pure vertical capacity of the suction anchors. Conversely, it has been observed that the pure lateral capacity is affected to a great extent. The actual influence of misalignment on the ultimate lateral capacity can be assessed once the ratio of the ultimate horizontal capacity at different torsional angles, β, by the ultimate horizontal capacity at $\beta = 0°$ is computed.

Figure 3.6 depicts the relation between the aforementioned ratio and the torsional angle. The trend of these curves indicates that that even low misalignment angles ($\leq$ 10°) might result in non - negligible reduction of the anchor pure lateral capacity at any aspect ratio. This evident decrease of lateral capacity is attributed to the torsional shear stresses that mobilise a successively increasing portion of the available shear strength. This statement is also enhanced by the relation of the lateral bearing factor, N_{h}, with torsional angle as depicted in Figure 3.5b.

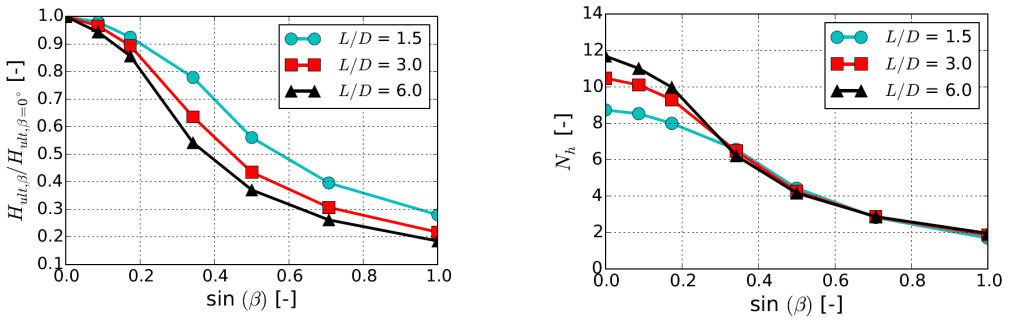

(a) $H_{\mathrm{ult},\beta}/H_{\mathrm{ult},\beta=0°}$ - $\sin\beta$ relation

(b) N_{h} - $\sin\beta$ relation

Figure 3.5: Misalignment effect on lateral capacity at different aspect ratios [39]

In addition, [39] has drawn attention to the fact that the elliptical curves expressed through Equation 2.6, which are used for the prediction of undrained bearing capacity of anchors, do not only depend on the length to diameter ratio, but also on the misalignment angle, β.

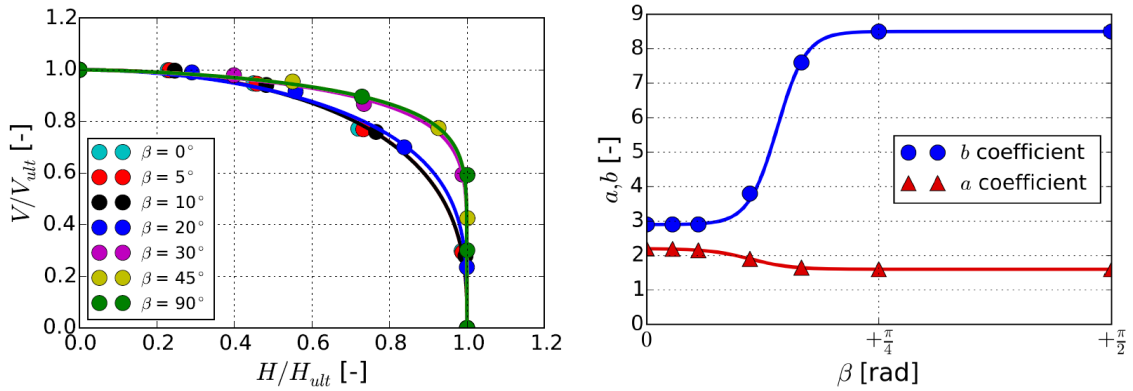

(a) HV interaction diagram

(b) a, b shape coefficients

Figure 3.6: Misalignment effect on HV interaction diagrams and a, b shape coefficients for short anchor ($L/D = 1.5$) [39]

In Figure 3.6a, the whole set of obtained results is presented for the short anchor. The numerical results have been analytically interpolated with elliptical curves through Equation 2.6. This was accomplished by adjusting the a and b coefficients to match the

HV failure loci shape at different values.

A more detailed look at these graphs reveals that, as the misalignment angle increases, the horizontal capacity is progressively less affected by the vertical one. Therefore, while increasing β angle, the horizontal translation seems to be less dominant over the torsional twist that takes place. As a consequence, HV shape coefficients, a and b, vary, not only with the aspect ratio but also with β angle as demonstrated in Figure 3.6b. Results for the medium and the long anchor can be found in the Appendix C.

3.3 Effective stress analysis in Plaxis 3D

As already described in Section 3.2.2, the numerical calculations of the benchmark study were all conducted following a total stress analysis and relative assumptions about soil behaviour. This type of analysis is used widely to tackle this type of offshore engineering problems as it is a fast method that produces reasonable results. However, it is known that a total stress analysis is only an approximation of the actual soil behaviour. In this section, the reasons why an effective stress analysis is more representative of the expected soil stress paths will be elaborated.

Generally, for every elastic medium there is a certain number of equations that is essential in order to define how it deforms and gets internally stressed due to external loading. These equations belong to the three categories listed below:

- equilibrium equations
- compatibility equations
- constitutive law equations.

As far as the drained statics of saturated soils are concerned, the aforementioned equations are adequate to make the problem solvable as the number of equations is equal to the number of unknowns.

When the undrained statics of saturated soils are considered, the generated pore water pressures are unknown. This means that an additional equation has to be established in order to solve this type of problems. It is true that, during undrained conditions, volumetric changes do not take place. Thus, Equation 3.2 is the missing equation that constitutes this problem solvable. Everything described above is also true during the numerical calculations of a finite element analysis. Therefore, during undrained loading, for every point of the finite element model, volumetric strains are constrained as it is true that:

$$\epsilon_{\mathrm{v}} = \epsilon_{\mathrm{x}} + \epsilon_{\mathrm{y}} + \epsilon_{\mathrm{z}} = 0 \tag{3.2}$$

At this point, it should be highlighted that, when a total stress analysis is followed, volume is conserved only if appropriate assumptions are made about the soil behaviour, like $\nu \simeq 0.5$. Therefore, in the case of the benchmark study, the use of a simplified Tresca failure criterion together with the Undrained(C) option in Plaxis 3D is followed by smart assumptions about the undrained behaviour of clay in order to achieve the volume conservation as described in Section 3.2.2.

Another shortcoming of the approach adopted by the benchmark study is described below. In Figure 3.7, there is a schematic presentation of a normally consolidated soil specimen under undrained triaxial compression and the corresponding expected effective (ESP) and total stress paths (TSP) in q - p' plane. There, it is clearly shown that the undrained shear strength of a soil medium depends on the effective stress path and cell

pressure. It is obvious that as the confinement pressure increases, s_u is expected to increase as well. The expected soil behaviour under an undrained triaxial compression test is used here as an example to show the discrepancy between total and effective stress paths but different stress paths would be expected under undrained direct simple shear and extension tests.

Emphasis should be given to the fact that, during for the effective stress approach of the benchmark study, pore water perssures are not calculated and effective stress paths remain unknown. Thus, the soil strength does not depend on pressure variations during the analysis. This dependency has to be introduced separately in the software for the benchmark study and this is accomplished by setting a variation of s_u with depth. Finally, it is worth noting that the undrained shear strength of clays is different under compression, extension and simple shear which is an aspect that is not captured by the Tresca failure criterion. Undrained shear strength is the same for all types of loading.

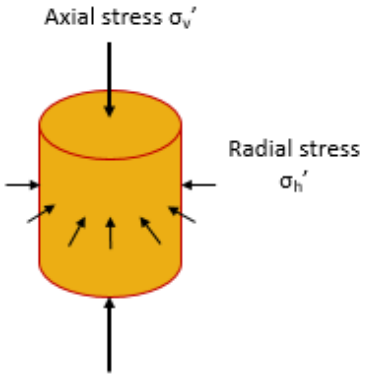

(a) Schematic representation of a TXC test on a soil specimen

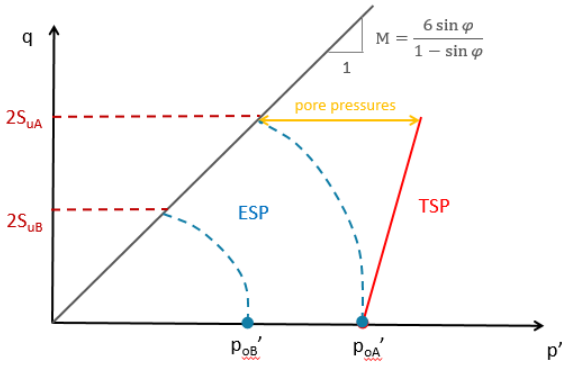

(b) Total and effective stress paths during a TXC test

Figure 3.7: Normally - consolidated soil response under an Undrained Triaxial Compression (TXC) test

All the aforementioned disadvantages of the approach followed by the benchmark study acted as a motivation and challenge for this current approach of the same problem. It was decided that an effective stress analysis would be followed by selecting the Undrained(A) option in Plaxis 3D. Thus,effective soil parameters should be introduced in the software and, based on them, undrained parameters of clay are computed. Additionally, the development of pore pressures can be captured and the effective stress paths are known. The way in which Plaxis manages to explicitly distinguish between effective stresses and (excess) pore pressures is by automatically adding the stiffness of water to the stiffness matrix.

From all the constitutive models for which the Undrained(A) option is available in Plaxis 3D, it was decided that the Soft Soil model is the most suitable one in this case for the following reasons. Firstly, it is an advanced model that is able to capture the behaviour of soft soils, like normally consolidated clays. Secondly, it has a Mohr - Coulomb type failure surface that has a deviatoric section which is comparable to the Tresca failure criterion of the benchmark study for low friction angles (Figure4.12).

Finally, due to everything described above, it is believed that the coupling of Undrained (A) with the Soft Soil model constitutes a more realistic simulation of the actual behaviour of soil. However, it is a method that is not widely used because effective strength parameters are not always available from geotechnical site investigation surveys. The features that characterise the Soft Soil model are described in the Section 4.4.1. The essential calibration of the Soft Soil model to represent the conditions of the benchmark study is

presented in Section 4.4.2 in detail. Comparative results between the two approaches are available in Section 4.7.

3.4 2D FE analysis with SPCalc

In offshore engineering projects that involve the design of suction anchors, the accurate prediction of the anchor bearing capacity is of profound importance. For this specific reason, a finite element application, named SPCalc, has been developed by Plaxis bv and the Norwegian Geotechnical Institute (NGI) under a joint venture known as XG Geotools bv.

This two dimensional special purpose finite element tool aims to specifically calculate the undrained load capacity of these structures. It is able to estimate the load factor for different sizes and shapes of suction anchors in multiple layers of soil in a realistic way through a robust numerical procedure. Moreover, it provides the evolution of stresses within the soil, as well as the displacements of the anchor at the failure state. All the aforementioned calculations are possible within less than a minute.

This approach constitutes the second part of the present study as it shares important common characteristics with the way in which the bearing capacity of misaligned suction anchors is modelled by the three dimensional approach of the benchmark study. This statement acted as a stimulation to compare the results of the two approaches. This comparison aims to reveal whether a simplified finite element approach developed for numerical convenience is sufficiently comparable to an equivalent three dimensional analysis.

In this section, a detailed reference is made to the limitations of this software, which are compared simultaneously to the conditions of the benchmark study. Additionally, a description of the way misalignment effect is modelled is provided. Further features governing the numerical calculations of SPCalc are provided in Chapter 5 together with the acquired results.

3.4.1 Assumptions

As stated by [12], there are certain assumptions on which this software is based. These assumptions are listed below together with comments concerning their importance under the scope of this study.

- SPCalc uses a 2D plain strain model that takes into account the side shear contribution present in the third direction. In this way, it can also account for 3D effects that have an impact on the anchor behaviour.
- Only suction anchors that have a top closed can be modelled, which is a feature that exactly matches this study.
- The surrounding soil is loaded under undrained conditions, which is again an aspect that suits this specific research. Moreover, using the NGI - ADP constitutive model allows for the clay strength anisotropy to be modelled.
- The soil plug and the structure act together as a rigid body. This condition is a limit of the software. However, this is not an issue for this research as the development of failure surfaces within the anchor interior are not considered.

3.4.2 Misorientation effect

Misorientation, or misalignment, effect is a common phenomenon in engineering reality. It is often observed that the chain force acting on the padeye is not perpendicular to the

surface of the anchor. This is due to the fact that the anchor has been wrongly installed in the first place and, thus, a torsion is induced around the centerline of the suction anchor as depicted in Figure 3.8.

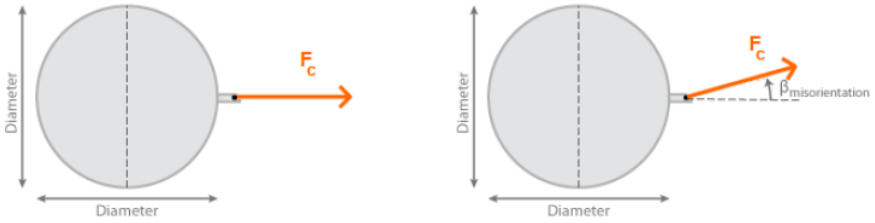

Figure 3.8: Misorientation (top view) [12]

To account for the misalignment effect on the overall bearing capacity, SPCalc adopts a very simple approach. The basis of this approach is the modification of the set-up, or adhesion, factor α_{out} for the outskirt soil - structure interface. To account for the torsional moment induced by the padeye misorientation, the adhesion is lowered. This leads to the reduction of the magnitude of the horizontal shear stresses acting on the anchor and, therefore, the overall bearing capacity decreases.

In the presence of a torsional angle, the modified set-up factor α_{res} is used given by:

$$\alpha_{\text{res}} = \alpha_{\text{out}} \cdot \sqrt{1 - \left[\frac{F_{\text{c}} \cdot \cos(\alpha_{\text{inclination}}) \cdot \sin\beta \cdot Offset}{M_{\text{max}}}\right]^2} \tag{3.3}$$

Where M_{max} is the torsional capacity computed by:

$$M_{\text{max}} = \frac{\pi D}{2} \sum_{n=1}^{i=1} \xi \cdot \overline{(s_{\text{u}}^{\text{DSS}})_i} \cdot (\alpha_{\text{out}})_i \cdot h_{\text{i}} \tag{3.4}$$

The parameters found in the above formulas are:

- D: diameter of the anchor [m]
- F_{c}: chain force acting at the padeye [kN]
- $\alpha_{\text{inclination}}$: angle between the chain force and the horizontal line [°]
- $\beta_{\text{mis-orientation}}$: misalignment angle between the chain force and the line that links the padeye with the centre axis of the anchor [°]
- Offset: depth of the padeye ($= 0.7L$) [m]
- $\overline{s_{\text{u}}^{\text{DSS}}}$: average undrained shear strength of a soil layer in direct simple shear [kN/m^2]
- ξ: reduction factor due to open crack at active side. Since no crack is considered in this study, ξ is taken as 1.
- h: height of a soil layer

If $\beta_{\text{mis-orientation}}$ is zero, then the set-up factor is not reduced and, consequently, the ratio $\alpha_{\text{res}}/\alpha_{\text{out}}$ is 1. It is possible to increase $\beta_{\text{mis-orientation}}$ until the value of 15° leading to the reduction of the ratio $\alpha_{\text{res}}/\alpha_{\text{out}}$ to a minimum value of 0.1.

Chapter 4

Numerical model in Plaxis 3D

4.1 Introduction

The first current numerical analysis is performed in Plaxis 3D AE following an effective stress analysis. The 3D finite element models are equivalent to the ones created for the benchmark study as described in Section 3.2. This allows for relevant comparisons to be made. The main discrepancy between the two analysis is that for the current one, water is present in the soil domain.

In this section, important aspects concerning the FE numerical modelling of the problem within Plaxis 3D are discussed. Furthermore, the basic principles governing the undrained effective stress modelling of clay behaviour are elaborated. Significant features of the Soft Soil constitutive model are described. Moreover, the procedure that was followed in order to accomplish the calibration of this model with respect to the benchmark study is explained in detail. In the context of this research, five calibrations were realised and each one of them aims to capture different aspects of the soil behaviour. Finally, the obtained results are presented and compared with the benchmark study.

4.2 Elements and Interfaces

In Plaxis 3D, the soil volume is presented through 10 - node tetrahedral elements with 4 - point Gaussian integration [11]. These soil elements are depicted in Figure 4.1a. They have three degrees of freedom (u_x, u_y, u_z) per node and can provide a second-order interpolation of displacements.

The soil - structure interaction is modelled by means of interface elements. The interface elements are 12-noded triangular elements (Figure 4.1b) with pairs of nodes instead of single nodes [11]. For this type of elements, 3 - point Gaussian integration is accomplished. Each one of the nodes has three degrees of freedom (u_x, u_y, u_z).

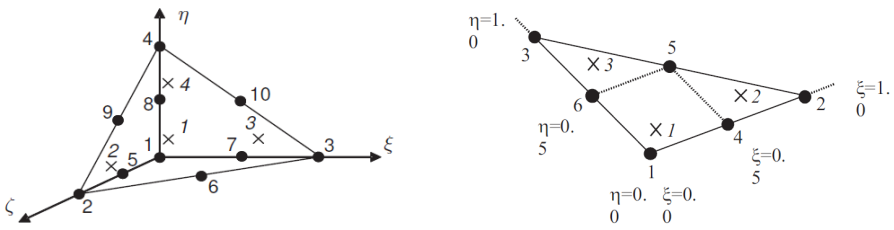

(a) Soil elements (b) Interface elements

Figure 4.1: Schematic representation soil elements and interface elements in Plaxis 3D [11]

In Figure 4.3a, a 3D view of the soil domain that is created in Plaxis 3D is available.

In the same figure, it can be seen that the suction anchor is centered in the model and the mesh becomes finer closer to it. This is also apparent in Figure 4.3b 4.3c and where a horizontal and vertical cross - section of the problem is depicted. Even though, for the benchmark study, it is true that the suction anchors are modelled as cylindrical rigid bodies including the soil plug (Section 3.2.1), this is not representative for the analyses of the current thesis that involve water. Therefore, the suction anchors are modelled as rigid bodies that are composed of only the surfaces of the cylindrical shaft and the top cap. In this way, the soil plug can deform and pore water pressures are allowed to generate within the shafts of the suction anchor. The finite element models created for the rest of the anchors with L/D = 3 and 6 are similar to the presented one.

Figure 4.2 illustrates the interfaces that are employed in the finite element model. In Figure 4.2a, the red surfaces represent the suction anchor and the brown cylindrical interface is used to model the soil - anchor interaction and the strength reduction along the outside surface of the cylindrical anchor shafts. The strength of this interface is determined through the strength reduction factor, R_{inter}, which is set equal to 0.65. Equation 4.1 reveals the correlation between the strength of the soil and the interface strength. Hence, the cohesion(adhesion) and frictional angle of the interfaces is reduced compared to the surrounding soil. No internal interface is created for the suction anchor as it is an additional feature that would not affect the results significantly and it would make the numerical calculations even more complicated.

$$c_{\text{i}} = R_{\text{inter}} \cdot c_{\text{soil}} \text{ and } \tan\phi_{\text{i}} = R_{\text{inter}} \cdot \tan\tan\phi_{\text{i}} \leq \phi_{\text{soil}} \tag{4.1}$$

As reported by [11], interfaces are also important when corners of stiff structures are present in a soil domain. These points need special attention as the abrupt changes in boundary conditions might lead to high peak stresses and strains, which are not realistic. This phenomenon can be prevented by specifying additional extended interface elements at the bottom of the anchor as depicted in Figure 4.2 where they are coloured in grey and green. A top view (Figure 4.2a) and a bottom view (Figure 4.2b) reveal their geometry. No strength reduction is applied for these additional interfaces, which are extended at a depth for which smooth results are obtained.

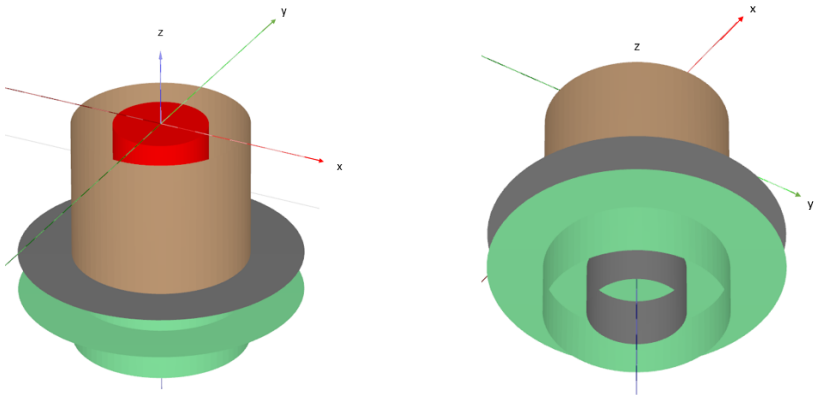

(a) Top view (b) Bottom view

Figure 4.2: Interfaces of the domain created for L/D =1.5

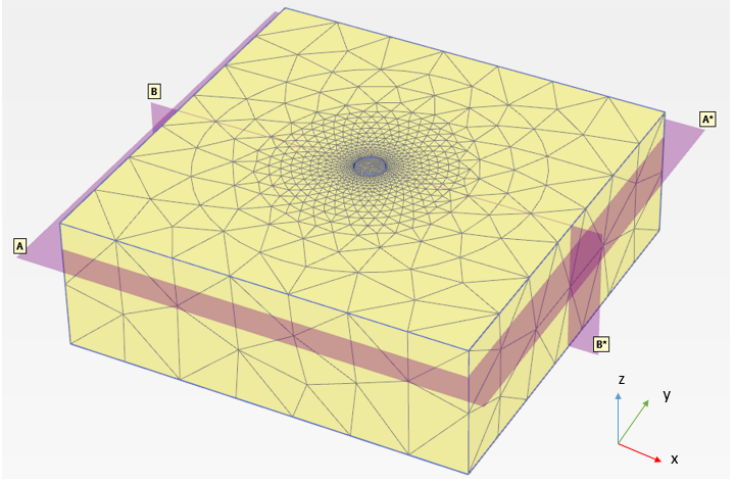

(a) 3D finite element mesh

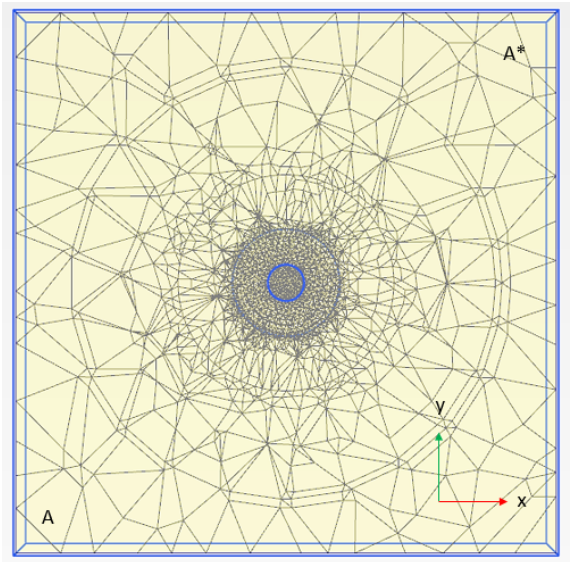

(b) Cross - section AA*

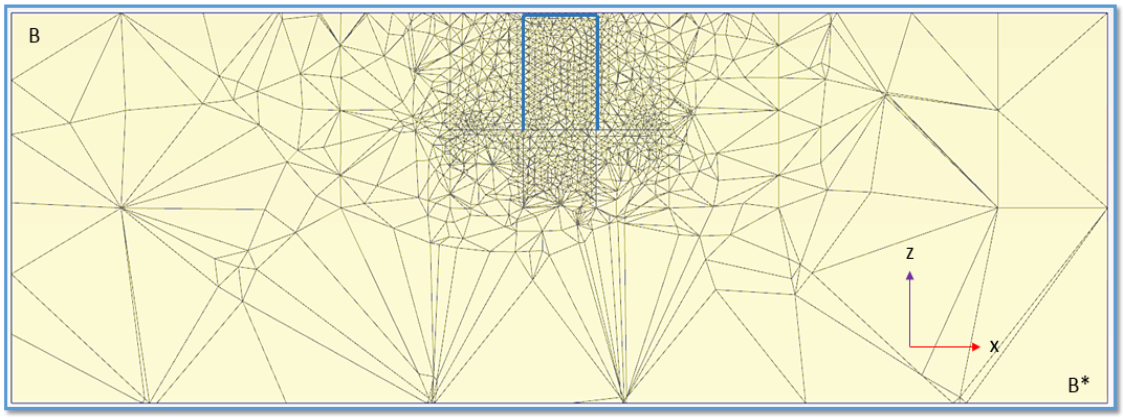

(c) Cross - section BB*

Figure 4.3: FE disctretisation of the domain created for L/D =1.5

4.3 Model sizes and FE discretisation

The numerical analysis of the undrained HV capacity of misaligned suction anchors in clay involves the creation of three different projects where three different suction anchors with three aspect ratios are placed in the middle as shown in Figure 4.3. The diameter is equal to 5 meters for all anchors and the chosen lengths are 7.5, 15 and 30 meters. The dimensions of the domains of these three numerical models were selected so that the boundary conditions do not affect the kinematics and failure mechanisms of this problem. Domain sizes are reported in Table 4.1. The vertical boundaries of all the domains are constrained against horizontal displacements, the base of the model is fully fixed and the seabed is free to deform in all directions.

Table 4.1: Plaxis 3D domain sizes for different aspect ratios

L/D [-]	x_{min} [-]	x_{max} [-]	y_{min} [-]	y_{max} [-]	z_{min} [-]	z_{max} [-]
1.5	-37.5	37.5	-37.5	37.5	-25.0	0.0
3	-32.5	32.5	-32.5	32.5	-40.0	0.0
6	-65.0	65.0	-65.5	65.0	-90.0	0.0

The model discretisation aims to produce satisfactory (converged) results. Very fine meshes were created for all the domains that were refined even more closer to the anchor. This was possible through the creation of 3 cylindrical surfaces around the pile as shown in Figure 4.4. The diameters of these surfaces are 3D, 6D and 12D and all of them have a length equal to $L+D$. Thus, the coarseness of the mesh can be increased manually as the radial distance from the caisson decreases. The coarseness factor of the external surface is 0.8, for the intermediate internal one is 0.2 and for the one closer to the anchor is 0.1.

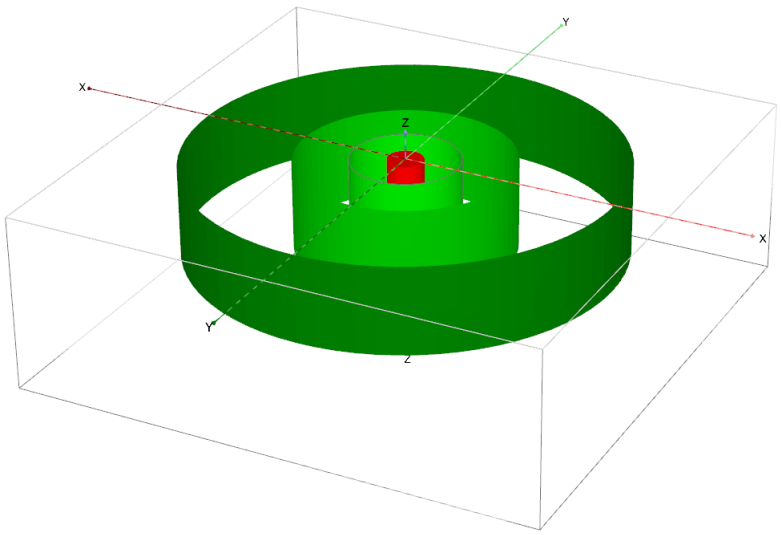

Figure 4.4: Cylindrical surfaces created for gradual mesh refinement (domain for $L/D = 1.5$)

In deep water applications, the water head might start hundreds of meters above the seabed. However, the water head in the the finite element models of this study starts at the seabed as the effective stresses are the same for any water depth and, therefore, the results are not influenced by the actual water head, as also stated by [41].

The number of elements and nodes created for each domain can be found in Table 4.2.

Table 4.2: Number of elements and nodes for all 3 created projects

L/D [-]	N° of elements	N° of nodes
1.5	87102	126166
3	116979	167868
6	157253	223602

4.4 Effective stress modelling of undrained clay behaviour

4.4.1 Soft Soil constitutive model

Soft Soil model is an advanced model that simulates the behaviour of soft soils, such as normally consolidated clays, clayey silts and peat. The selection of this model to carry out the effective stress analysis was based on three main reasons. Firstly, Undrained (A) type of loading is possible when using this model in Plaxis. Secondly, it is a constitutive model that is capable of predicting the undrained effective stress paths of soft soils. Thirdly, it has a Mohr - Coulomb yield criterion that is comparable to the shape of the Tresca failure criterion used in the benchmark study in the deviatoric plane. More details on this model are provided as follows.

The Soft Soil model is based on the Cam - Clay theory and was developed in order to capture the extreme compressibility that soft soils exhibit under compression. It is worth citing the work of [26] that demonstrates that normally consolidated clays can behave even 10 times softer than normally consolidated sands. To simulate this behaviour, the Soft Soil model assumes that there is a logarithmic relation between changes in volumetric strains, ϵ_{v}, and changes in mean effective stress. Equation 4.2 formulates this logarithmic relation that is true for virgin compression and λ^* is the modified compression index that determines the compressibility of a material in primary loading.

$$\epsilon_{\mathrm{v}} - \epsilon_{\mathrm{v}}^{\circ} = -\lambda^* \ln\left(\frac{p' + c\cot\phi}{p'^{\circ} + c\cot\phi}\right) \tag{4.2}$$

The plot of Equation 4.2 is a straight line that is depicted in Figure4.5. In the same figure, the path that is followed under isotropic unloading and reloading is also presented. This path is given by the formula that follows, where κ^* is the modified swelling index that determines the compressibility of a material in unloading and reloading. The loading/unloading lines depend primarily on the largest stress that has been experienced by the soil, which is the pre - consolidation stress, p_{p}. This pre - consolidation stress remains constant during unloading and reloading and increases during primary loading as irreversible plastic strains are generated.

$$\epsilon_{\mathrm{v}}^{\mathrm{e}} - \epsilon_{\mathrm{v}}^{\mathrm{eo}} = -\kappa^* \ln\left(\frac{p' + c\cot\phi}{p'^{\circ} + c\cot\phi}\right) \tag{4.3}$$

Equations 4.4 and 4.5 reveal the relationship of λ^* and κ^* with the internationally recognised parameters of 1D compression index, C_{c} and swelling index, C_{s}. All of these parameters can be determined through 1D compression tests.

$$\lambda^* = \frac{C_{\mathrm{c}}}{2.3(1+e)} \tag{4.4}$$

$$\kappa^* \approx \frac{2C_{\mathrm{s}}}{2.3(1+e)} \tag{4.5}$$

The Soft Soil model response is elastoplastic from the very beginning of loading and excess pore pressures are generated. However, the unloading - reloading response is purely elastic and is described by Hooke's law. Equation 4.6 unravels that there is a linear

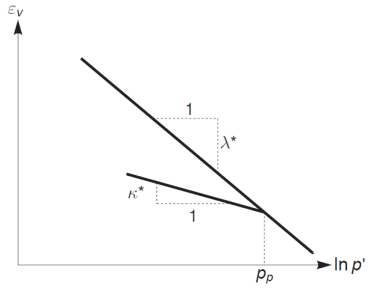

Figure 4.5: Logarithmic relation between volumetric strains and mean effective stress [11]

stress dependency of the bulk modulus and the stiffness. Both that bulk modulus for unloading/reloading, K_{ur}, and the Young's modulus for unloading/reloading, E_{ur}, are computed through ν_{ur} and κ^*.

$$K_{\mathrm{ur}} = \frac{E_{\mathrm{ur}}}{3(1-2\nu_{\mathrm{ur}})} = \frac{p'_{\mathrm{ref}} + c\cot\phi}{\kappa^*} \tag{4.6}$$

Where p'_{ref} is equal to the mean effective stress at a reference level.

The Soft Soil model has the special characteristic of having two yield functions that are illustrated in Figure 4.6 in 2D and 3D space.

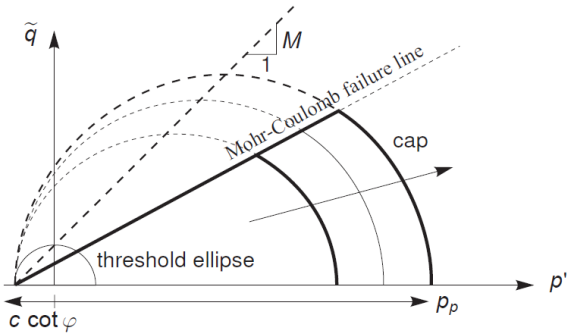

(a) Yield surface in q - p' plane

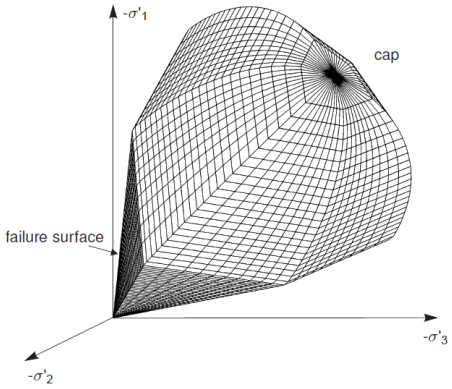

(b) Yield surface in principal stress space

Figure 4.6: Schematic representation of the yield surface of the Soft Soil model [11]

The one that represents the modified Cam - clay hardening ellipse (cap of the yield contour) is described by the following equations.

$$f_{\mathrm{c}} = \frac{q^2}{M^2} + p'(p' - p_c) \tag{4.7}$$

During primary compression, the cap expands and is pushed out. Consequently, plastic volumetric strains are accumulated leading to soil compaction, which is compensated by elastic expansion under undrained conditions as in this case total volumetric strains should be equal to zero. Plastic volumatric strains are generated according to the following formula, which is the hardening rule of this model.

$$d\epsilon_v^p = (\lambda^* - \kappa^*)\frac{dp_p}{\mid p_p \mid} \tag{4.8}$$

What distinguishes the Soft Soil model from the modified Cam - Clay model is the way failure is modellled. The failure state of Soft Soil is not related to critical state but it is modelled according to Mohr - Coulomb criterion and it is represented in the q - p' plane by a straight line given by Equation 4.9. Therefore, failure is fixed and is not dependent on the M line. In this way, softening behaviour is excluded by the model.

$$f_f = \tfrac{1}{3}(\sigma_3' - \sigma_1') + \tfrac{1}{2}(\sigma_3' + \sigma_1')\sin\phi' - c\cos\phi' \tag{4.9}$$

The combination of the yield functions described above defines the plastic behaviour of Soft Soil and leads to the total boundary of the elastic stress area. Stress paths within this area are elastic, whereas stress paths that tend to cross this area produce both elastic and plastic strains.

As reported by [11], the M line determines the shape of the yield cap and to a great extent the shape of the undrained effective stress paths during undrained loading. M is not directly involved in determining the shear strength as the failure is described by the Mohr - Coulomb failure criterion but it does affect the pore water pressure generation. In contrast to the Cam-clay theory, where M depends on the friction angle, ϕ', [10] computed that the M inclination of the Soft Soil model is given by the subsequent formula, involving the material parameters $K_{\mathrm{o}}^{\mathrm{nc}}$, $\lambda*$, $\kappa*$ and ν_{ur}.

$$M = 3\sqrt{\frac{(1-K_{\mathrm{o}}^{\mathrm{nc}})^2}{(1+2K_{\mathrm{o}}^{\mathrm{nc}})^2} + \frac{(1-K_{\mathrm{o}}^{\mathrm{nc}})(1-2\nu_{\mathrm{ur}})(\lambda^*/\kappa^*-1)}{(1+2K_{\mathrm{o}}^{\mathrm{nc}})(1-2\nu_{\mathrm{ur}})(\lambda^*/\kappa^*) - (1-K_{\mathrm{o}}^{\mathrm{nc}})(1+\nu_{\mathrm{ur}})}} \tag{4.10}$$

The parameters that are important for the formulation of the Soft Soil model in Plaxis 3D are summarised in the table that follows:

Table 4.3: Parameters of the Soft Soil model

Parameter	**Symbol**	**Unit**
Modified compression index	λ^*	[-]
Modified swelling index	κ^*	[-]
Lateral earth pressure coefficient in normal consolidation	$K_{\mathrm{o}}^{\mathrm{nc}}$	[-]
Poisson's ratio for unloading - reloading	ν_{ur}	[-]
$K_{\mathrm{o}}^{\mathrm{nc}}$ - parameter	$M_{\text{Soft Soil}}$	[-]
Effective cohesion	c'_{ref}	[kPa]
Friction angle	ϕ'	[°]
Dilatancy angle	ψ	[°]

4.4.2 Calibration of Soft Soil model

The comparison between the total and effective stress analysis requires the calibration of the Soft Soil parameters with special focus to create a soil domain that matches the conditions of the benchmark study [39]. In this way, the results can be compared and the differences between the two approaches can be evaluated. The calibrated parameters are selected so that the offshore soil conditions are represented in the best possible way. The calibration was performed with the help of the Soil Test Facility available by Plaxis 3D,

which is a convenient tool where numerical simulations of triaxial compression, triaxial extension and direct simple shear tests can be realised in a single stress point environment.

Figure 4.7 explains qualitatively the main principles of the Soft Soil model calibration. As stated in Section 3.2.2, the undrained shear strength, s_u, of the benchmark study varies with depth and during loading the total stress paths (TSP) are followed. The main purpose of this calibration is to create a soil with the same variation of s_{u} with depth that is accomplished through the effective stress paths. Attention should be given to the fact that the effective stress paths of the Soft Soil model will not commence from the isotropic axis as horizontal effective stresses are not equal to the vertical effective stresses. Hence, the soil is K_{o} - consolidated in the beginning. The three different depths (A, B and C) indicated in the same figure correspond to three different mean effective stresses (p'_{oA}, p'_{oA} and p'_{oC}) that should lead for both models to the same undrained shear strengths (s_{uA}, s_{uB} and s_{uC}) as demonstrated in the same figure.

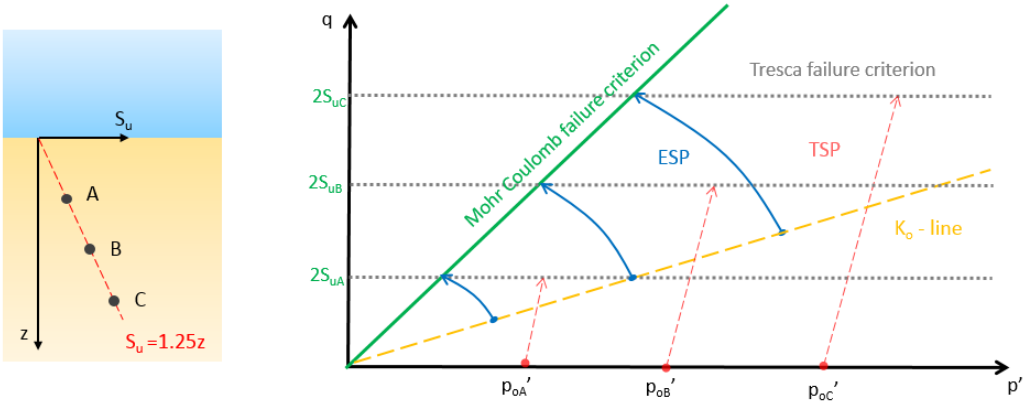

Figure 4.7: Qualitative representation of the Soft Soil model calibration concept

It should be highlighted that in order to achieve a representative calibration for the case where an anchor is loaded at the padeye, the failure mechanism that governs this specific problem has to be identified. As a suction anchor is loaded with varying inclinations in the vertical plane from 0° to 90°, it is hard to decide which is the dominant failure mode for all load inclinations. On one hand, undrained compressive and simple shear strength of the soil plays the most important role when the pile is loaded horizontally. On the other hand, when the pile is loaded vertically, the behaviour of soil under undrained extension and shear is expected to govern the failure mechanism.

In the context of this study, five different calibrations were conducted leading to five sets of Soft Soil parameters. All of them are accomplished following the same procedure and each one of them features a different aspect of the problem. The aforementioned calibrations can be divided in two separate categories. The first category aims to have values for the angle of friction, ϕ', and the lateral earth pressure coefficient, $K_{\mathrm{o}}^{\mathrm{nc}}$, of clays that are most commonly found in the offshore environment. This category involves Calibrations A and B.

The second category of calibrations intends to capture the different types of undrained stress paths that develop when the pile is loaded with different angles from horizontal to vertical direction. The calibrations that belong to this category are C, D and E. Details for each one of them are presented below.

Calibrations A and B: Matching compression

In this category, two calibrations are created with special focus on the adoption of the most representative values of friction angle, ϕ', and K_o^{nc} for offshore clays. For both of the calibrations, the undrained compressive and simple shear stress paths are considered as the ones that are most likely to be followed during loading. It should be highlighted that the calibration of the Soft Soil model parameters is not feasible unless a few reasonable assumptions are made about the soil properties as a start. Table 4.4 summarises that mandatory assumptions which are made with regard to the realistic representation of the normally consolidated clays' behaviour. All these assumptions remain true for all calibrations.

Table 4.4: Initial ssumptions regarding Soft Soil model material properties

Parameter	Symbol	Unit	Value
Saturated unit weight	γ_{sat}	[kN/m^3]	16
Poisson's ratio for unloading - reloading	ν	[°]	0.2
Effective cohesion	c'	[kPa]	0
Dilatancy angle	ψ	[°]	0
Strength reduction factor	R_{inter}	[-]	0.65

The way in which the Soft Soil model is structured does not allow for its calibration according to the benchmark study unless relatively low friction angles are chosen and, additionally, K_o^{nc} is chosen to be higher than the estimation stemming from Jaky's formula (Equation 4.11). Selecting a higher K_o^{nc} leads to effective stress paths with a more pronounced curvature and this is the only way that the magnitude of the undrained shear strength can be achieved with realistic values of ϕ'.

$$K_o^{nc} = 1 - \sin\phi' \tag{4.11}$$

Relevant literature from triaxial tests conducted on different types of offshore clays, including London clay, ([24], [9], [30], [48]) unravels that a value of 18° can be considered as a lower boundary for the friction angle, where as a value of 22° can be regarded as a mean boundary for offshore clays. Consequently, two calibrations (A and B) were accomplished with $\phi' = 18$ and 22°, which are the lowest and the highest frictional angles with which the two models can be in accordance. The goal of the calibrations is not only to match the strength of the soil of the benchmark study but also the stiffness upon loading. The way in which this is accomplished and the procedure that was followed for all the calibrations is explained in more detail in Appendix A.

Table 4.5 summarises the two sets of Soft Soil parameters determined for the two calibrations following the aforementioned procedure. The parameter $M_{\text{Soft Soil}}$ is calculated through Equation 4.10.

Table 4.5: Two sets of calibrated Soft Soil model parameters

Parameters	Symbol	Set A	Set B	Unit
Friction angle	ϕ'	18	22	[°]
Lateral earth pressure coefficient	K_o^{nc}	0.78	0.7925	[-]
Modified compression index	λ^*	0.109	0.24	[-]
Modified swelling index	κ^*	0.0183	0.0186	[-]
K_o^{nc} - parameter	$M_{\text{Soft Soil}}$	0.8539	0.8561	[-]

Figure 4.8 illustrates the stress paths that are followed when the two aforementioned calibrated models are subjected to undrained triaxial compression. Although the depicted stress paths correspond to a soil sample that is located at 30 m depth in the soil domain, the expected stress paths at any depth are qualitatively identical to these ones. It is apparent that the achieved values of s_u for both calibrations coincide and they are also equal to the s_u of the benchmark study that embraces a Tresca failure criterion. This figure explains how the same variation of s_u with depth can be accomplished with two different friction angles using the Soft Soil model. Thus, it is clarified that this hinges on the fact that during loading different stress paths can be followed that have a pre - determined curvature based on K_o^{nc}.

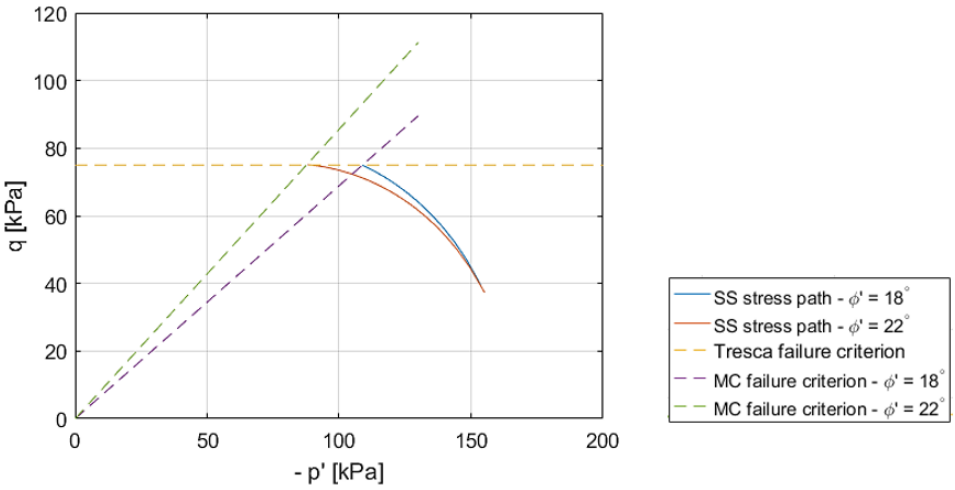

Figure 4.8: Compressive stress paths for Calibrations A and B

Figures 4.9, 4.11 and 4.10 illustrate the responses of the two sets of material properties determined for Calibrations A and B under undrained triaxial extension, triaxial compression and direct simple shear at a certain depth of 30m depth. This depth corresponds to the length of the longest suction anchor. The responses of the two models are qualitatively identical for all depths.

In Figures 4.9 and 4.11, it can be observed that soil strengths under triaxial compression and direct simple shear coincide. This is due to the fact that the selected angles of friction, 18° and 22°, are low and the Mohr - Coulomb deviatoric section of the Soft Soil model is very close to the one corresponding to the Tresca failure criterion. This is clearly illustrated in Figure 4.12 where the projections of the positive and the negative principal stress axes are drawn on the π plane. Additionally, it is interesting to note that the calibration with $\phi' = 22°$ produces more plastic strains and, therefore, more pore water pressures.

A more detailed look at Figure 4.12 reveals that, even though compression points of both criteria are perfectly matched, the extension points do not coincide. Consequently, as illustrated in Figure 4.10, s_u is significantly lower for extension for both calibrations compared to the benchmark study and this is explained by the irregular hexagonal failure criterion of Mohr – Coulomb implemented for the Soft Soil model. The inclination of the Mohr - Coulomb failure line for compression in q - p' stress space is given by: $6\sin\phi'/(3-\sin\phi')$, while for extension is computed by: $6\sin\phi'/(3+\sin\phi')$, which is lower and leads to lower s_u.

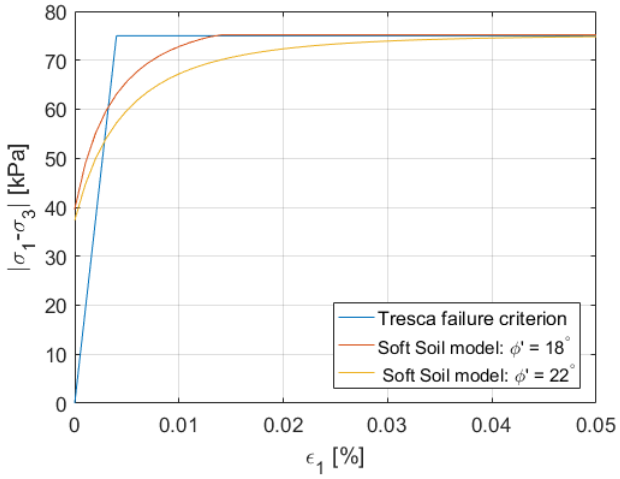

Figure 4.9: Response of the two calibrated Soft Soil models for $\phi' = 18$ and $\phi' = 22$ under undrained triaxial compression

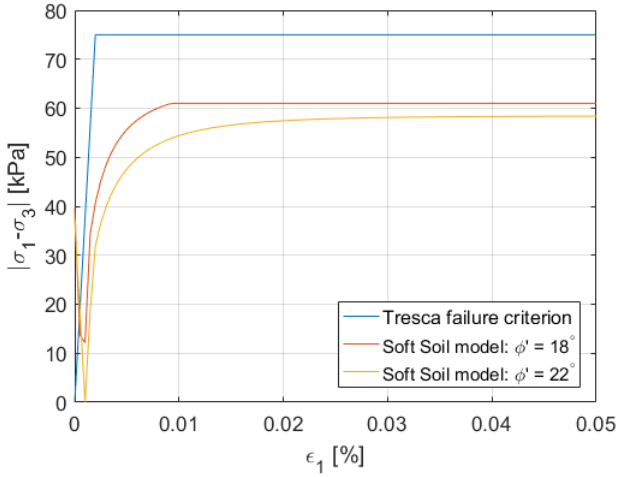

Figure 4.10: Response of the two calibrated Soft Soil models for $\phi' = 18$ and $\phi' = 22$ under undrained triaxial extension

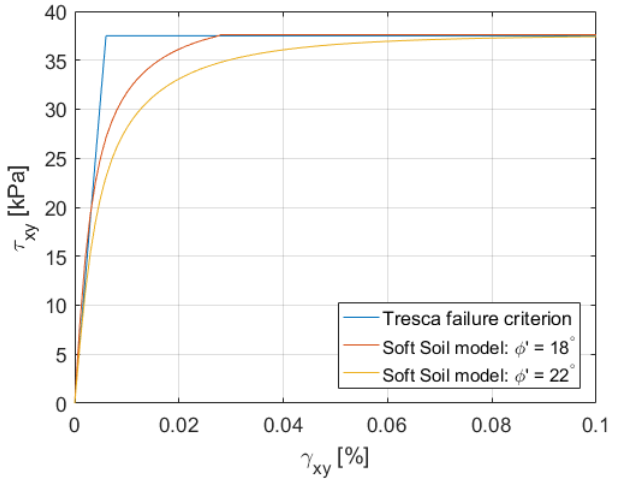

Figure 4.11: Response of the two calibrated Soft Soil models for $\phi 3' = 18$ and $\phi' = 22$ under undrained direct simple shear

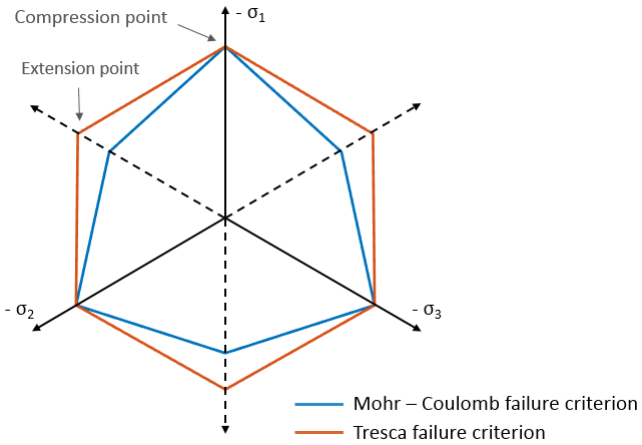

Figure 4.12: π - plane representation of Tresca and Mohr - Coulomb failure surface for $\phi' = 22°$

Figure 4.13 demonstrates the variation of s_u with depth for the three types of loading mentioned above. The blue line is the one that corresponds to the benchmark study and coincides with the variation of s_u for both of the Calibrations A and B under undrained triaxial compression and undrained direct simple shear. The difference between the two calibrations is apparent only for extension.

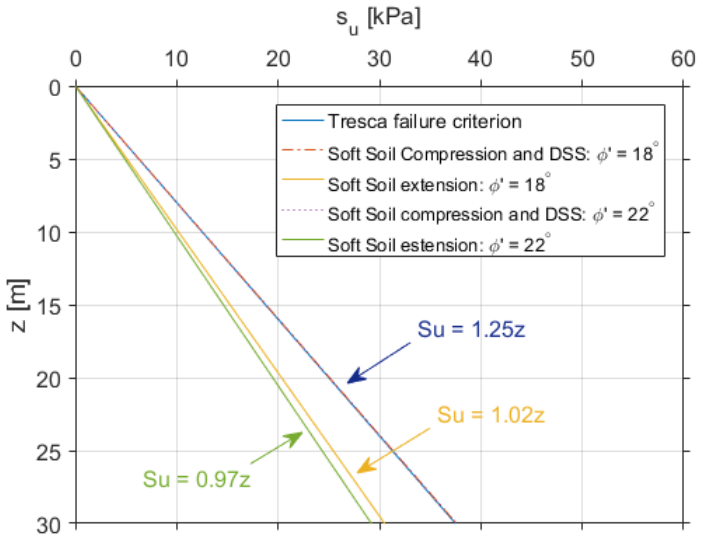

Figure 4.13: Variation of undrained shear strength with depth for the two calibrations with $\phi' = 18$ and $\phi' = 22$

Calibrations C: Matching extension

This Calibration aims to fit the benchmark study's soil conditions with the response of undrained triaxial extension. In this case, the use of $\phi' = 18°$ is not possible and this is attributed to the way in which the Soft Soil model actually works. More precisely, as illustrated in Figure 4.14, if $\phi' = 18°$ is selected in this case, the desired amplitude of the s_u coming from undrained triaxial extension could only be achieved if an almost vertical stress path is followed. Several trials in the Plaxis Soil Test Facility revealed that, in this setting, this could not be accomplished even for values of K_o^{nc} close to 0.5. Therefore,

choosing a higher value of ϕ' allows for the accomplishment of the desired s_u with a curved stress path.

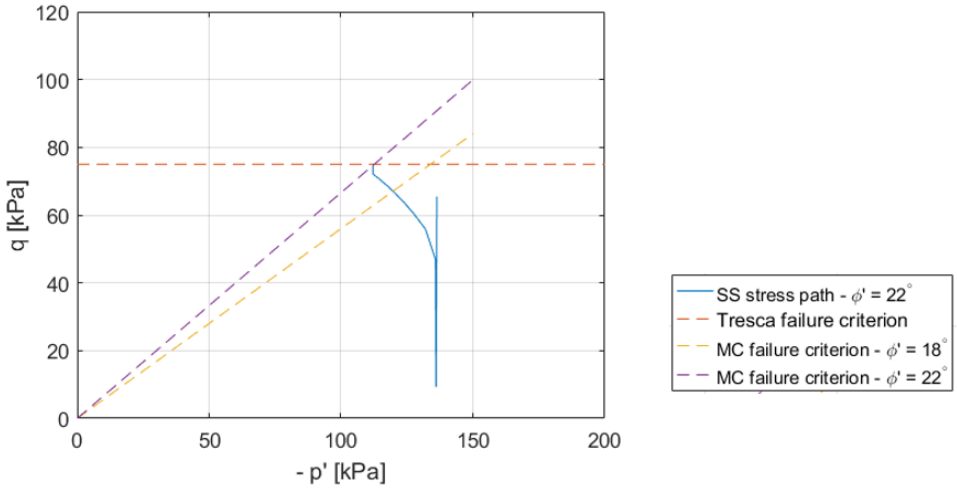

Figure 4.14: Extensive stress path for Calibration C using $\phi' = 22°$

As a consequence of everything described above, a value of 22° is chosen for this calibration so that comparisons with Calibration B can be made. The response of this calibration under triaxial extension, triaxial compression and direct simple shear can be found in Appendix B.

Figure 4.15 demonstrates the variation of s_u with depth for the three types of loading stemming from this calibration. The blue line is the one that corresponds to the benchmark study and coincides with the variation of s_u for Calibration C under undrained triaxial extension that is indicated with the yellow dotted line. The red curve represents undrained triaxial compression and direct simple shear. Table 4.6 presents the Soft Soil material parameters that were used for this calibrations (Set C).

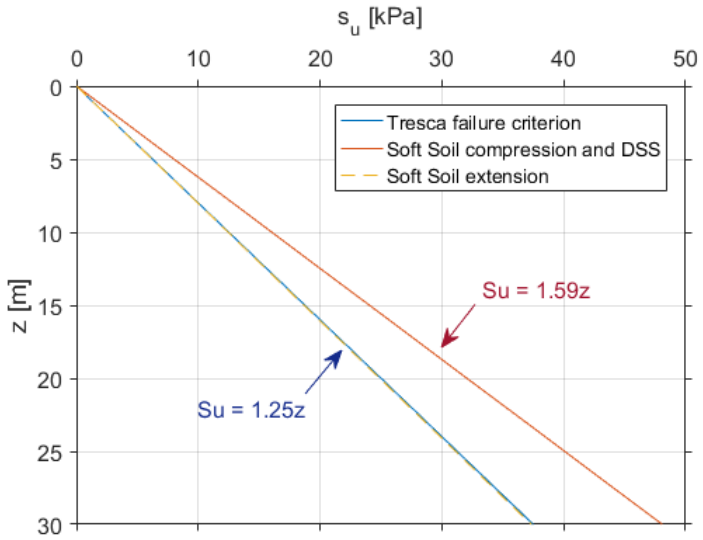

Figure 4.15: Variation of undrained shear strength with depth for the calibration matching the extensive behaviour of the benchmark study

Calibration D: Matching average of compression, extension and simple shear

Calibration D intends to match the average of the responses coming from triaxial extension, triaxial compression and direct simple shear of the Soft Soil model with the benchmark study. Again this is done for $\phi' = 22°$ so that relevant comparisons are possible.

The response of this calibration under triaxial extension, triaxial compression and direct simple shear can be found in Appendix B. Figure 4.16 illustrates the variation of s_u with depth for the three types of loading stemming from this calibration. The average of these three s_u variations is in perfect agreement the variation of the benchmark study (blue line) and s_u variation with depth from compression coincides with DSS (red line). A more detailed look at the graph reveals that the average variation is closer to compression and DSS in this case.

The determined Soft Soil parameters of this calibration can be found in Table 4.6 (Set D).

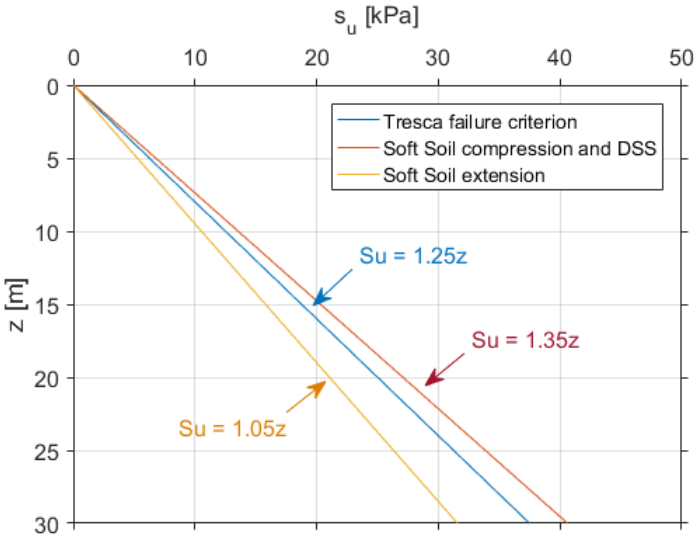

Figure 4.16: Variation of undrained shear strength with depth for Calibration D

Calibration E: Matching average of compression and extension

This calibration is very close to Calibration D and the purpose of its creation is to achieve a calibration that represents the average of only compressive and extensive beheviour. As it has already been explained above, the variation of undrained shear strength from direct simple shear coincides with the variation of undrained shear strength from triaxial compression. Therefore, this calibration can also be regarded as the average behaviour of direct simple shear and triaxial extension.

The soil parameters that were selected to accomplish this calibration can be found in Table 4.6 and correspond to Set E. The behaviour of the soil behaviour that is obtained by this set of parameters under triaxial compression, triaxial extension and direct simple shear is demonstrated in Appendix B.

The variation of the undrained shear strength with depth that stems from the material parameters of Set E is depicted in Figure 4.17. It is worth to note that in this case the variation of s_u with depth of the benchmark study falls extactly in the middle of the responses of compression (or DSS) and extension of the new calibrated model and coincides with their average response.

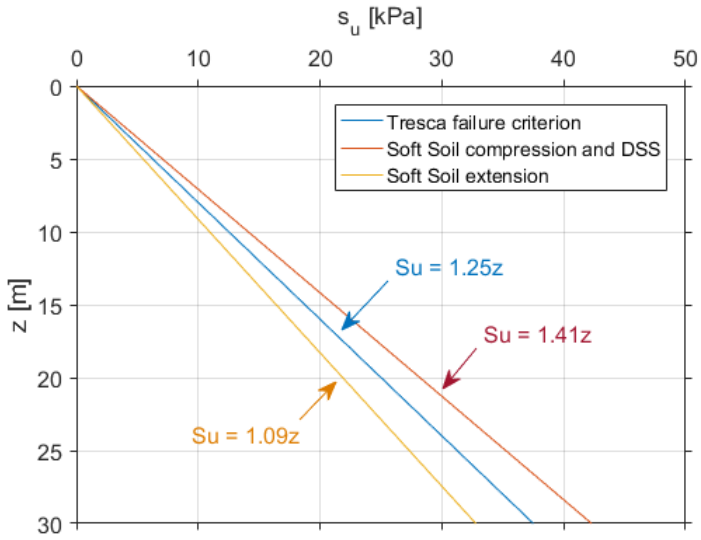

Figure 4.17: Variation of undrained shear strength with depth for Calibration E

Table 4.6: Two additional sets of calibrated Soft Soil model parameters

Parameters	**Symbol**	**Set C**	**Set D**	**Set E**	**Unit**
Friction angle	ϕ'	22	22	22	[°]
Lateral earth pressure coefficient	K_o^{nc}	0.6362	0.76	0.74	[-]
Modified compression index	λ^*	0.1	0.16	0.14	[-]
Modified swelling index	κ^*	0.0163	0.0181	0.0178	[-]
K_o^{nc} - parameter	$M_{\text{Soft Soil}}$	1.226	0.9266	0.9721	[-]

The HV interaction diagrams that result from all the aforementioned calibrations are presented in Section 4.7, where relevant discussion is made.

4.5 Loading application methods

The loads are applied in the exact same way as in the benchmark study, which is described in Section 3.2.3 following a load displacement procedure. The loading takes place under undrained conditions and all the loads are applied at the depth of the padeye. As the implementation of the Soft Soil model in Plaxis is more complicated than the Tresca failure criterion, the effective stress analyses take more than double time to complete. Therefore, only one realistic misalignment angle, $\beta = 10°$, was examined in the context of this study. The loading angles in the vertical plane, θ, are selected so that well defined curves of the HV failure loci are achieved. The θ angles differ for each aspect ratio. All of them are presented in Appendix C and D where the limit loads are also given.

During the numerical analyses, the loads are applied on the anchor in several increments until the failure load is reached and a well - defined plateau is formed. This is the point at which the ultimate bearing capacity of the anchor has been reached. To achieve that, Plaxis uses an automatic step size procedure coupled with an iterative solver. Thus, the load advancement procedure is significantly affected by the numerical control parameters which are presented in the following section. Load - displacement curves stemming from this analysis are presented in the Section 4.7.2 and Appendix D.

4.6 Numerical control parameters of the analyses

The numerical implementation of the advanced Soft Soil model within Plaxis 3D coupled with the created very fine finite element model, involving several interfaces and a great number of elements, constitute this project very demanding and difficult to solve within the software. Relatively fast analyses characterised by high accuracy can be accomplished with the adoption of the numerical control parameters found in 4.7. All of them were established through several trials.

Table 4.7: Numerical control parameters in Plaxis 3D

Parameter	**Value**
Solver type	Paradiso
Max cores to use	256
Max number of steps stored	1
Max steps	5000
Tolerated error	0.01
Max unloading steps	10
Max load fraction per step	0.02
Over - relaxation factor	1.2
Max number of iterations	100
Desired min number of iterations	60
Desired max number of iterations	80
Arc length control	On
Use line search	No
Use gradual error reduction	Yes

The tolerated error is set to the default value proposed by Plaxis that is equal to 0.01, as it has been observed that lower values would lead to time consuming analyses without any positive impact on the accuracy of the results. The accuracy of the numerical predictions is enhanced by selecting a very small load fraction per step that equals 0.02 leading to a step with a small size.

To prevent the analyses from stopping before the whole prescribed load is applied, maximum steps are defined as 5000 and maximum iterations, which take place within an individual step, are 100. Additionally, the maximum number of unloading steps is determined as 10, which means that there are 10 consecutive steps needed having less load than the previous step to indicate failure. In order to have a smooth load - displacement response of the system, over - relaxation factor is selected to be at the default value, which is 1.2, the arc length is on, the use line search is deactivated and the use of gradual error reduction is activated. Finally, with the implementation of these numerical parameters, the system is observed to be stable for the majority of the analyses as the number of iterations per step do not surpass the value of 3.

4.7 Results and discussion

The main purpose of this section is the presentation and discussion of the results that stemmed from the numerical calculations within Plaxis 3D following an effective stress analysis. First of all, the deformed state of all the anchors examined ($L/D = 1.5, 3$ and 6) is illustrated through figures that show the amplitude and the direction of the final mesh displacements for different loading inclinations. Additionally, the evolution of lateral and vertical limit loads while the anchor is loaded can be presented through load

- displacement curves. These curves are presented for various load inclinations of the short anchor in Section 4.7.2. The maximum loads that correspond to these curves are important for the creation of the HV failure envelopes. These HV failure loci are the most convenient way to compare the results with the benchmark study.

As stated in Section 4.6, an effective stress analysis requires complicated numerical calculations within the finite element software and, therefore, a significant amount of calculation time. For instance, it has been observed that the analysis of only one loading scenario of the smallest domain takes 4 hours in average to complete, whereas loading scenarios of the largest domain might take days to complete. As a consequence, even though five calibrations were made in the context of this study, the analysis of all three anchor aspect ratios was feasible only for the initial Calibration A. As far as the rest of the calibrations are concerned, the bearing capacity of only the short anchor will be investigated.

4.7.1 Deformed state at different loading inclinations

This section focuses on the presentation of the deformed state of the short suction anchor under different inclinations of loading. In this way, the failure mechanisms that develop when the anchor is loaded from 0° to 90° are visible. In order to get a better insight into the different patterns of motion followed by the anchor during loading, the magnitude and the direction of the final total displacements of the mesh are plotted. It is important to note that all the subsequent figures are actually detailed images of the suction anchor and the surrounding soil area that correspond to the vertical cross - section passing from the central axis and the padeye of the anchor. The cross - section described above is also presented in 4.3c.

Figures 4.18 and 4.19 illustrate the magnitude and the direction of the displacements of the mesh at the final step of the analysis when the anchor is loaded with a pure horizontal force at the depth of the padeye. In this setting, it is apparent that the anchor translates horizontally as a rigid body until failure is reached and no rotation takes place.

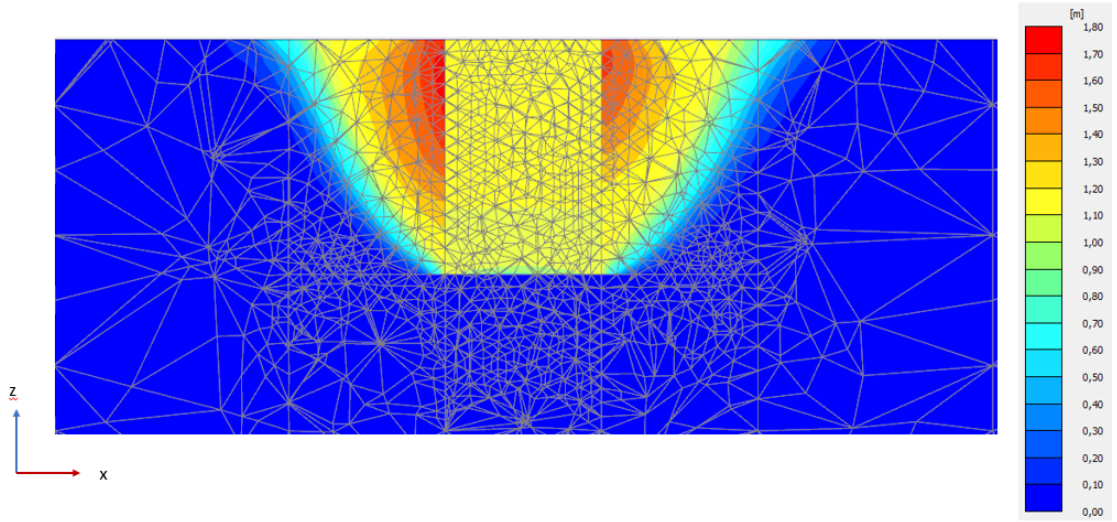

Figure 4.18: Displacements (shading) of short anchor due to horizontal loading (maximum displacement = 1.73 m)

As the inclination of the loading in the vertical direction increases, it is expected that a rotation of the anchor is likely to appear around y axis, which is perpendicular to the plane of the presented cross - sections. This phenomenon is obvious in Figures 4.20 and 4.21 that reveal the deformed state of the short anchor when the inclination of loading

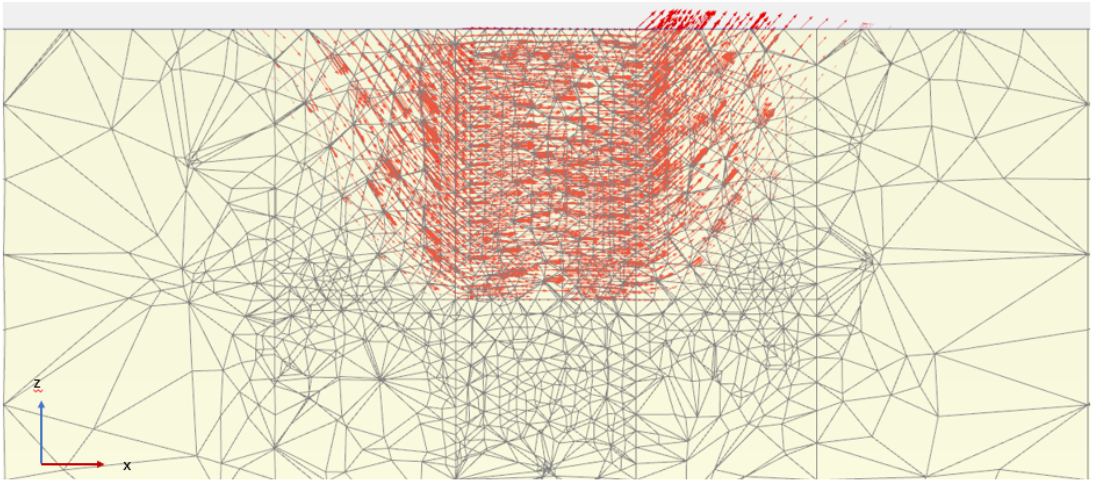

Figure 4.19: Displacements (arrows) of short anchor due to horizontal loading (maximum displacement = 1.73 m)

deviates from the horizontal direction and is equal to 56°. Therefore, in this case, the anchor is not displaced horizontally but rotates until the failure state.

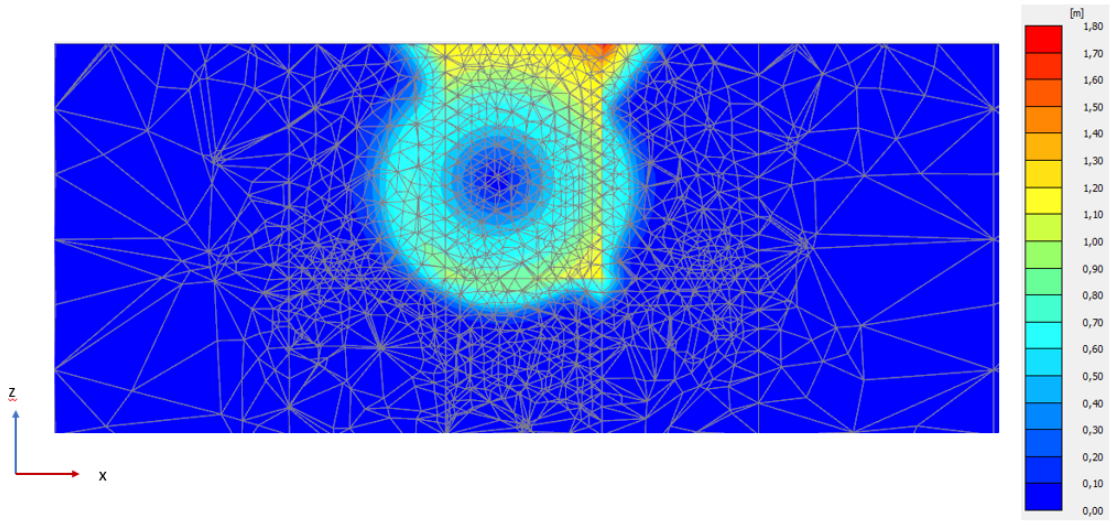

Figure 4.20: Displacements (shading) of short anchor due to loading of $\theta = 56°$ (maximum displacement = 1.7 m)

When a pure vertical loading of the suction anchor is considered at the depth of the padeye, Figures 4.22 and 4.23 unravel that the short anchor rotates around y axis until failure is reached. The main discrepancy between the failure mechanism that develops for a loading of $\theta = 56°$ and a pure vertical one is that the point around which rotation takes place is different for both cases. In the latter case, it corresponds to a point that is located closer to the bottom of the anchor.

As far as the medium and the long anchor are concerned, respective figures depicting the final displacements of the mesh can be found in Appedix D. It is interesting to highlight that as the anchor length increases, a vertical loading at the padeye is less likely to generate a rotation of the anchor. In the extreme case where the long anchor is subjected to a pure vertical load at the padeye, the anchor is translated vertically upwards without any rotation taking place. This phenomenon is apparent in Figure D.15 that shows the generated displacement of the long anchor when a vertical load is imposed on the padeye.

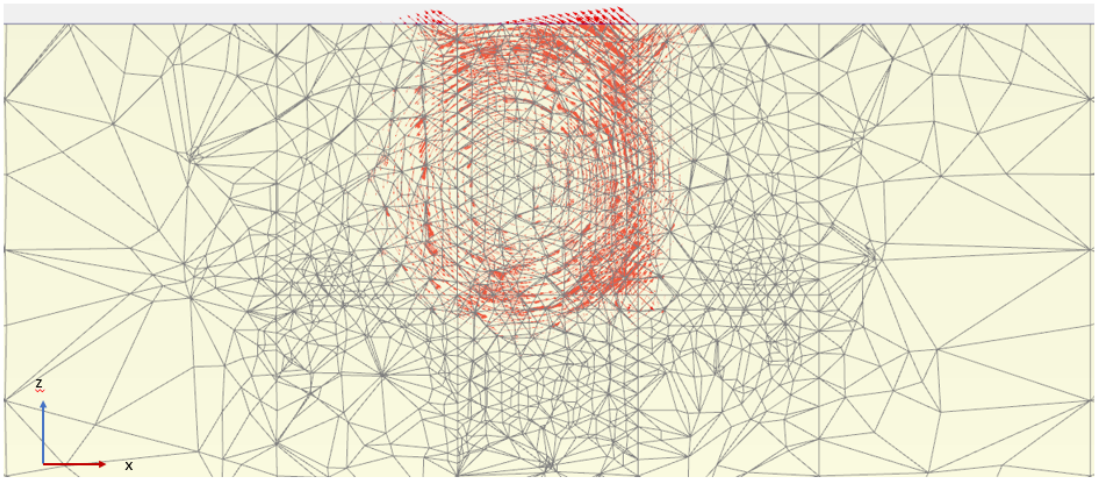

Figure 4.21: Displacements (arrows) of short anchor due to loading of $\theta = 56°$ (maximum displacement = 1.7 m)

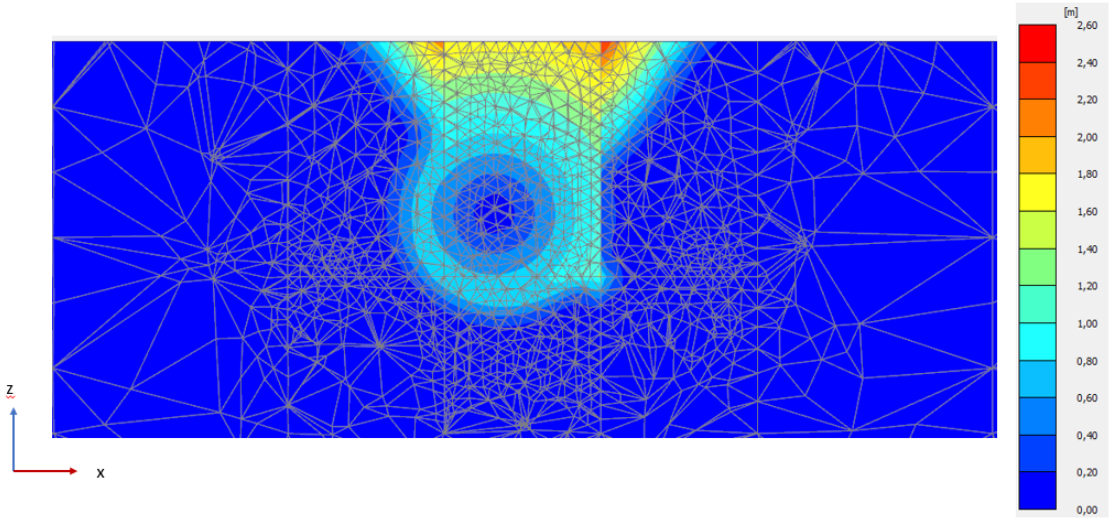

Figure 4.22: Displacements (shading) of short anchor due to vertical loading (maximum displacement = 2.4 m)

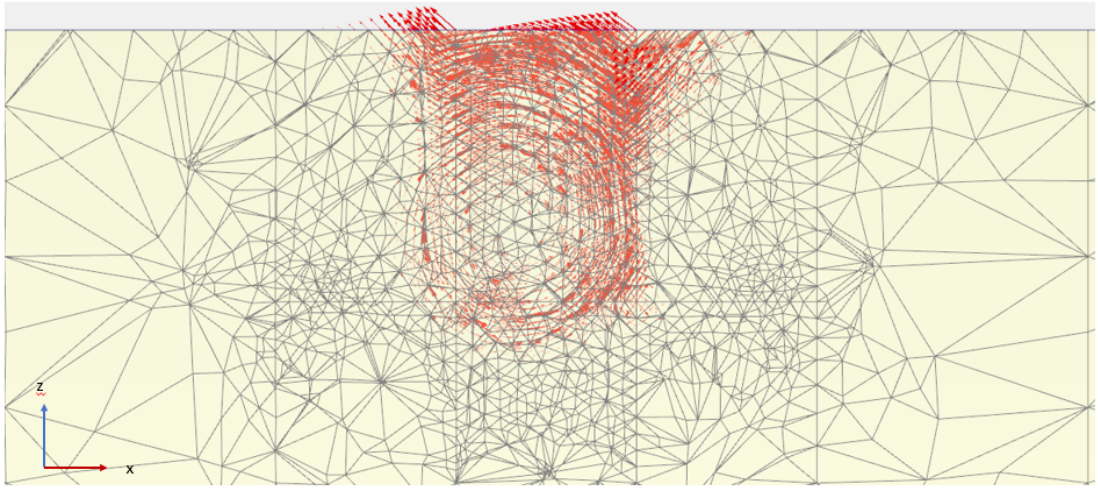

Figure 4.23: Displacements (arrows) of short anchor due to vertical loading (maximum displacement = 2.4 m)

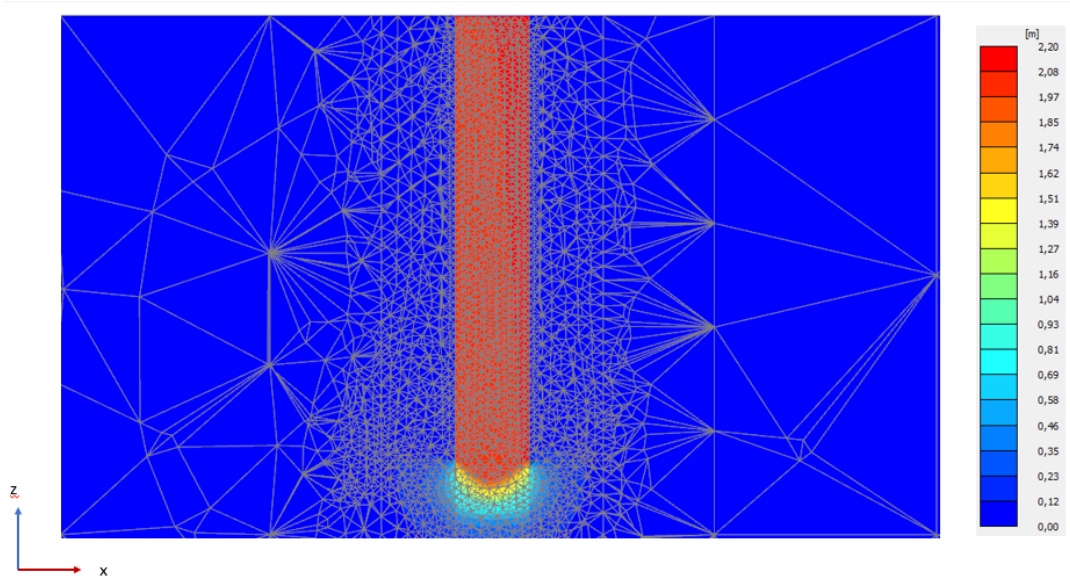

Figure 4.24: Displacements (arrows) of long anchor due to vertical loading (maximum displacement = 2.13 m)

4.7.2 Load - displacement curves

During the numerical computations of Plaxis 3D, the load is applied on the anchor in several steps. The load fraction induced at each one of the steps leads to a respective displacement of the anchor. This process continues until a failure state is reached where an infinitesimal load increment leads to an infinite displacement of the anchor. The evolution of this procedure can be visualised once load - displacement curves are plotted. In this way, the increment of the anchor bearing capacity with respect to its displacement can be evaluated and the kinematics governing the problem are revealed. The results demonstrated below are related to the short anchor and the analysis where no misalignment angle is present. Graphs for all anchor lengths and misalignment angles of Calibration A are available in Appendix D.

Figure 4.25 depicts the curves that are formed between the horizontal load and displacement of the anchor for loads with various angles, θ, in the vertical plane. The displacement corresponds to a point that is located at the center of the top cap of the anchor (seabed level). In this figure, it is apparent that the ultimate horizontal capacity progressively decreases as θ increases and it becomes equal to zero for a purely vertical load. Moreover, it is observed that when the anchor is loaded with a small inclination ($\theta \leq 12°$), the anchor displacements of the top cap are positive. This means that the suction anchor does not rotate but translates horizontally as a rigid body. Conversely, for $\theta > 12°$, the displacements of the top cap are equal to negative values. This phenomenon reveals that the anchor rotates backwards during loading.

Figure 4.26 shows the evolution of vertical bearing capacity during the loading of the anchor for different angles, θ. The curves drawn in this graph propose that the increase in vertical capacity is positively correlated with the increase of the loading angle, θ. As it was expected, for a purely vertical load, the vertical capacity is maximised.

The curve trends described above were expected prior to the numerical analysis and this denotes that the obtained results are logical. Additionally, these curves reveal the way in which the HV interaction diagrams presented below are drawn.

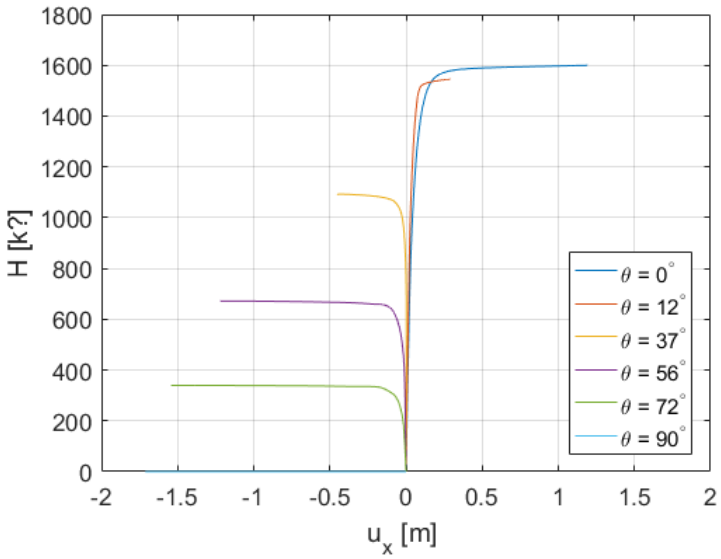

Figure 4.25: H - u_x curves for different load inclinations of suction anchor with $L/D = 1.5$ ($\beta = 0°$)

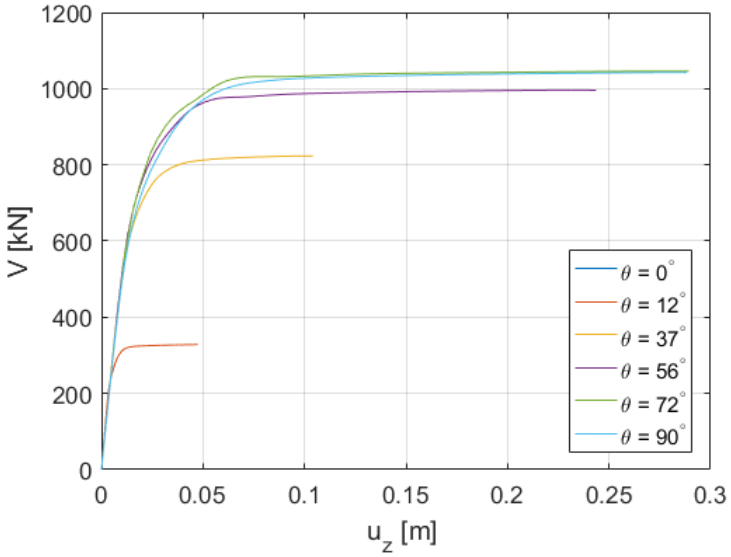

Figure 4.26: V - u_z curves for different load inclinations of suction anchor with $L/D = 1.5$ ($\beta = 0°$)

4.7.3 HV interaction diagrams

An overview of the effective stress analysis results is presented in this section. More precisely, results include the overall bearing capacity of suction anchors coming from Calibration A. Thus, HV failure loci of all aspect ratios are available, including the misalignment effect. Together with the presentation of results, relevant discussion is also made.

Calibration A

Calibration A is the initial calibration that is described in Section 4.4.2 and matches the compressive and shear behaviour of the benchmark study. It is the only calibration for which analyses were run for all anchor aspect ratios. In this section, HV interaction diagrams and normalised versions of them are presented with and without the effect of misalignment. In addition, elliptical fits that are integrated into the obtained data are available.

Figures 4.27a, 4.28a and 4.29a depict the HV failure loci for the three examined aspect ratios ($L/D = 1.5$, 3 and 6). These graphs show that an increase of the misalignment angle from 0° to 10° leads to a noteworthy decrease of the overall bearing capacity of the anchor as the failure envelopes shrink. To be more precise, although the ultimate vertical capacity remains uninfluenced by the increment of misalignment angle, the ultimate horizontal capacity decreases approximately 6%, 8% and 12% for the short, medium and long anchor respectively.

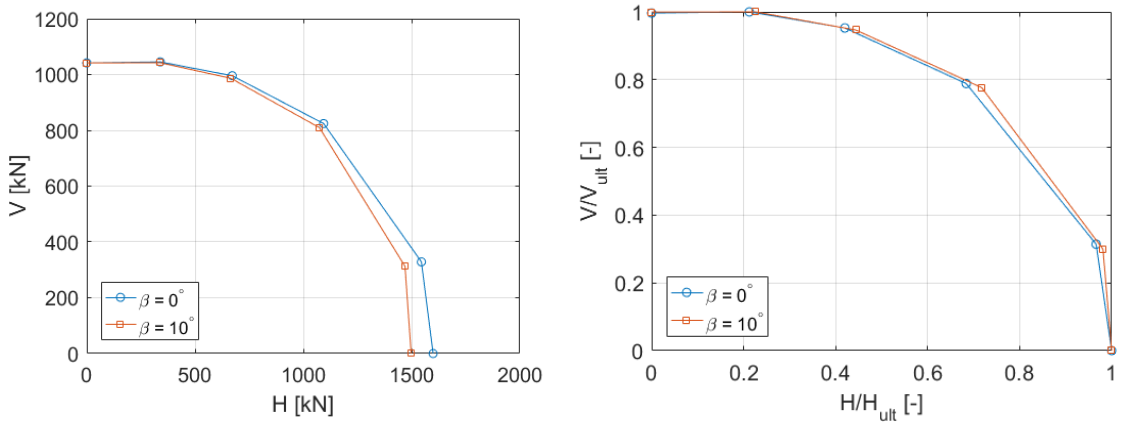

(a) HV interaction diagram

(b) HV normalised interaction diagram

Figure 4.27: Plaxis 3D results for L/D = 1.5 of Calibration A

Furthermore, the variation in misalignment angle does not have a remarkable impact on the normalised failure envelopes as it is proven by Figures 4.27b, 4.28b and 4.29b. In these graphs, normalised failure envelopes coincide for all aspect ratios. The values of these diagrams are computed by dividing the anchor bearing capacities of different load inclinations with the ultimate one. This means that H_{ult} corresponds to a purely horizontal load of 0° inclination and V_{ult} is correlated with a purely vertical load with an inclination of 90°.

Moreover, it is interesting to mention that a change in the length of the suction piles has an impact on the shape of the interaction diagrams. At this point, it should be clarified that the steep inclination presented in the upper part of the failure envelopes of

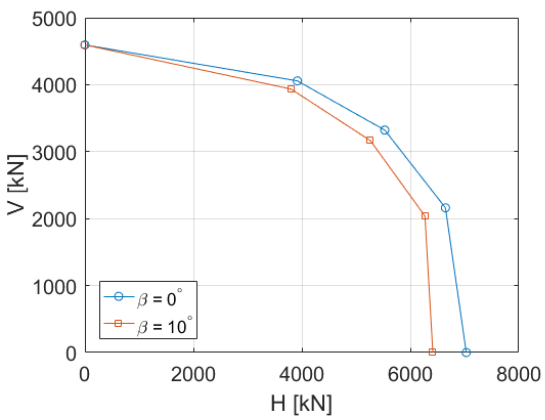

(a) HV interaction diagram

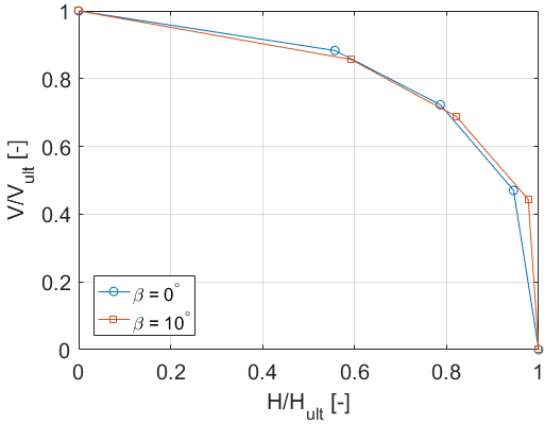

(b) HV normalised interaction diagram

Figure 4.28: Plaxis 3D results for L/D = 3 of Calibration A

the longest anchor (Figures 4.29a and 4.29b) is due to the lack of available results from the benchmark study for this range of loading angles. It is believed that results would be smoother if additional numerical data existed for this aspect ratio.

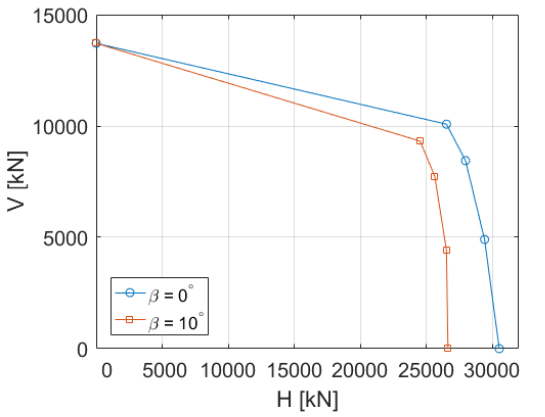

(a) HV interaction diagram

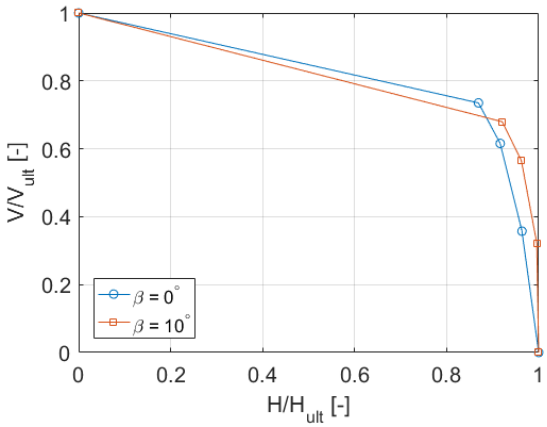

(b) HV normalised interaction diagram

Figure 4.29: Plaxis 3D results for L/D = 6 of Calibration A

The elliptical curves that are integrated to the acquired data through Equation 2.6 are plotted in Figures 4.30a, 4.30b and 4.30c. The elliptical interpolation was accomplished by modifying accordingly the shape coefficients, a and b (Table 4.8).

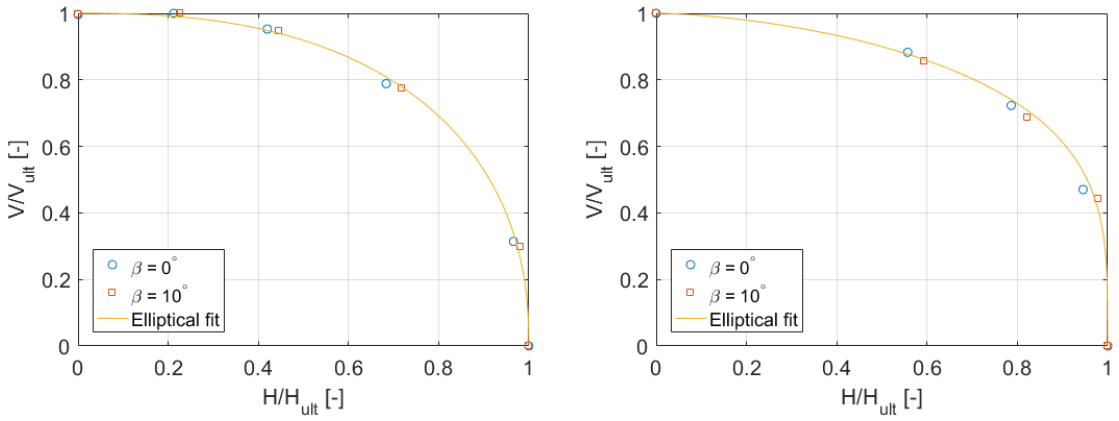

(a) L/D = 1.5

(b) L/D = 3

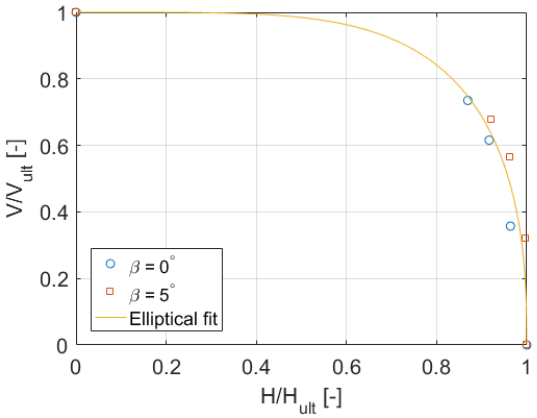

(c) L/D = 6

Figure 4.30: Elliptical curves integrated for the numerical data of all aspect ratios of Calibration A

Calibrations A and B

Calibration B was created with a special focus to match the undrained compressive and shear soil behaviour of the benchmark study and, in addition, to produce a Soft Soil calibration that has a more realistic value for the angle of friction, ϕ', equal to 22°. The results for this calibration are presented in this section. Results only for the short anchor are available including a misalignment angle of 10°.

Figure 4.31 demonstrates a comparison between the results obtained from Calibrations A and B in the form of HV interaction diagrams. These figures unveil that in terms of bearing capacity, the two aforementioned calibrations produce exactly the same results with and without the presence of misalignment. This is explained by the fact that the bearing capacity of a pile is most importantly influenced by the peak strength of the soil that coincides for these two calibrations. Thus, the fact that more pore water pressures and plastic strains are generated for Calibration B does not influence the final results that are related to the anchor capacity.

As the results obtained from these two calibrations can be assumed to coincide, from now on only results of Calibration B will be used for comparisons with the results of the rest calibrations. Calibrations B is chosen because, for this set of material parameters, ϕ' is equal to 22° and this is also true for the rest of the calibrations.

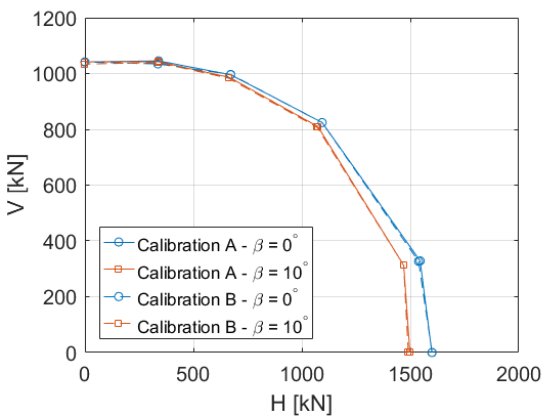

(a) HV interaction diagram

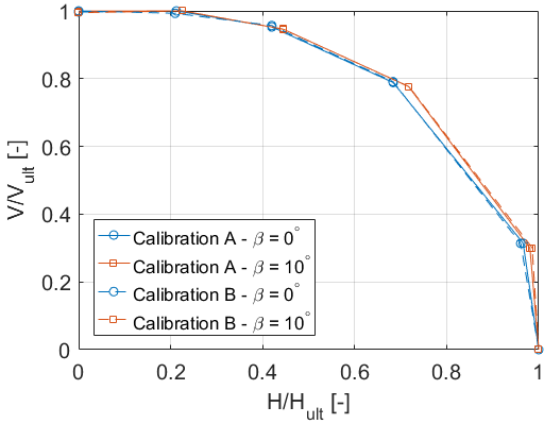

(b) HV normalised interaction diagram

Figure 4.31: Plaxis 3D results for L/D = 1.5 of Calibrations A and B

Calibrations C, D and E

Calibrations C, D and E were realised with special care to reproduce the soil conditions of the benchmark study under different types of loading. Results only for the short anchor are computed, including a misalignment angle of 10°. As the presentation of results from these calibrations is more interesting in comparison with the results from the benchmark study, they are available in the next section where they are simultaneously compared to the results from the total stress analysis.

4.8 Comparison between total and effective stress approach

The main objective of this section is to present the obtained results from the finite element analysis conducted within Plaxis 3D and, simultaneously, compare them with the results coming from the benchmark study. In this way, the discrepancies between the effective and total stress analysis can be evaluated. Moreover, the calibration that is more representative of this problem can be determined and, consequently, the dominant failure mechanism of this particular problem of suction anchor loading with various inclinations is unraveled.

As the analyses that are involved in this study require significant computational time, it was impossible to obtain results for all anchor lengths and all aspect ratios in the context of this study. Only in the case of Calibration A the analyses of all three aspect ratios were undertaken. For the rest of the calibrations (B, C, D and E), results are available only for the short anchor.

4.8.1 Calibration A

The results of the initial calibration of this study that follows an effective stress analysis (ESA) are presented in the form of HV interaction diagrams and, at the same time, they are compared to the results of the benchmark study that follows a total stress analysis (TSA). Figures 4.32a, 4.33a and 4.34a unveil that the suction anchor capacity, as predicted by the effective stress analysis, is lower for all aspect ratios compared to the total stress analysis. This observation is true when there is no misalignment angle inserted in the problem and when the misalignment angle is 10°.

This evident difference in the obtained results might be attributed to the fact that the soil behaviour under undrained triaxial extension plays a more important role in this problem than it was initially believed. As presented in Figure 4.13, the variation of s_u

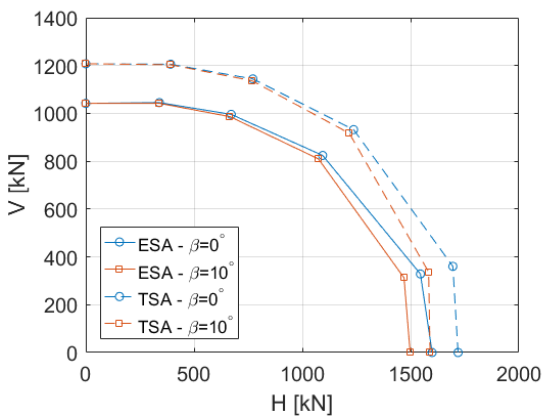

(a) HV interaction diagrams

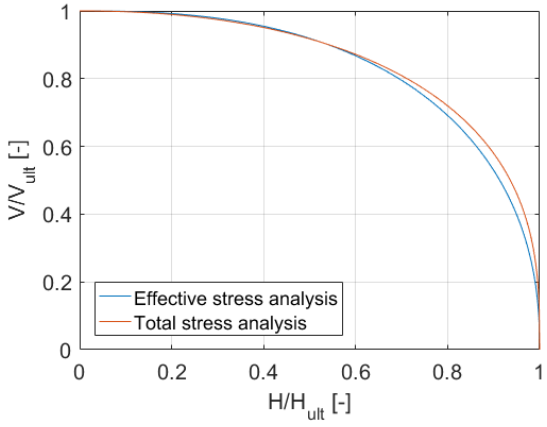

(b) Elliptical curves

Figure 4.32: Comparison of total and effective stress analysis for L/D = 1.5 (Calibration A)

from undrained triaxial extension with depth for this calibration is significantly lower with respect to the variation of the benchmark study. Thus, it is highly possible that by not regarding the matching of extensive behaviour as a priority for this calibration, the overall capacity with the calibrated model is underestimated. This observation could be validated by a thorough investigation of the stress paths that are followed in the model close to the area surrounding the embedded suction anchor, but this was not researched further in the context of this study.

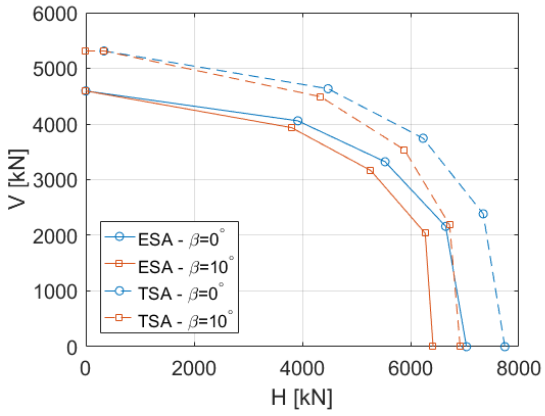

(a) HV interaction diagrams

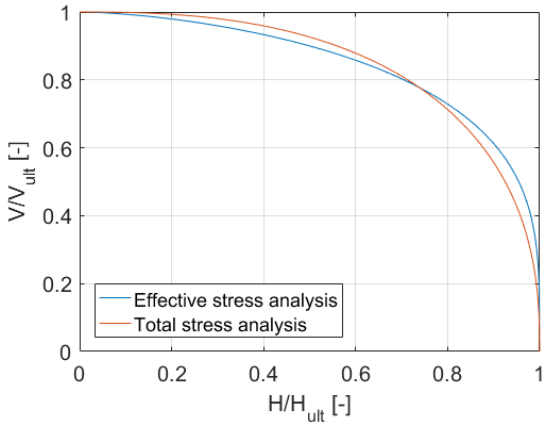

(b) Elliptical curves

Figure 4.33: Comparison of total and effective stress analysis for L/D = 3 (Calibration A)

Furthermore, Figures 4.32b, 4.33b and 4.34b present the curves that stem from the elliptical interpolation of the numerical data of both analyses through Equation 2.6. In these graphs, it can be easily seen that, for all the aspect ratios, the elliptical curves of the two approaches are extremely close. This remark suggests that the noticeable difference of the HV interaction diagrams between the two approaches arises from the difference in the prediction of the pure horizontal and vertical bearing capacity of the anchor. The determined values for a and b are presented in Table 4.8 in comparison to the ones stemming from the total stress analysis of the benchmark study.

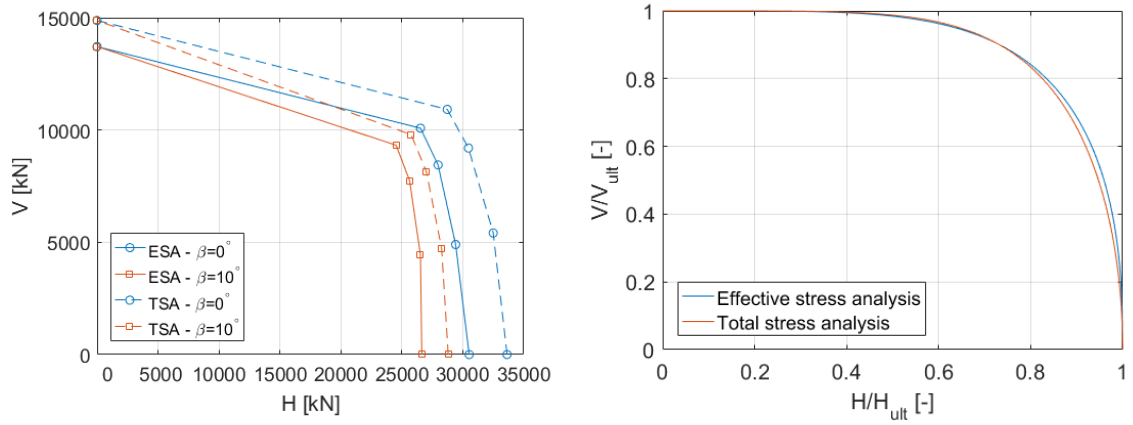

(a) HV interaction diagrams

(b) Elliptical curves

Figure 4.34: Comparison of total and effective stress analysis for L/D = 6 (Calibration A)

Table 4.8: Shape coefficients, a and b, for all aspect ratios of Total and Effective Stress Analysis results

Aspect ratio	**Effective stress analysis**		**Total Stress Analysis**	
L/D [-]	a [-]	b [-]	a [-]	b [-]
1.5	2.5	2.3	2.18	2.9
3	1.6	3.8	2.54	2.48
6	4.7	2.5	5.33	2

The observations described above unveil the incentive behind the creation of the rest of the calibrations that aim to capture different failure mechanisms that take place within the soil domain during the loading of the anchor with different load inclinations from horizontal to vertical direction.

4.8.2 Calibrations B and C

The pronounced difference in the obtained results between the TSA and ESA acted as a motivation for the creation of additional calibrations to further investigate this problem. Matching the extensive behaviour of the benchmark study was not set as a priority for the initial calibrations A and B. Therefore, Calibration C concentrates on making the extensive behaviour of these two models equivalent. A good estimate of the similarities and dissimilarities between Calibration B (matching compression and DSS) and Calibration C (matching extension) is provided through the subsequent comparative graphs. Numerical analyses were conducted only for the short anchor (L/D = 1.5) for these calibrations.

Figures 4.35a and 4.35b illustrate the HV failure loci without the presence of misalignment and with a misalignment angle of 10°. It is apparent that, irrespective of the misalignment effect, the benchmark study results lie between the results of these two calibrations. This observation unravels that a calibration matching the average of the undrained compressive, shear and extensive behaviour of the soil would produce results that are closer to the total stress analysis. Based on this idea, Calibrations C and D are created and results are available in the next section.

A closer look at the same graphs reveals that the curve of the total stress analysis is closer to Calibration B when pure lateral loading is considered. On the contrary, as the vertical loading increases, the ellipse of the total stress analysis approaches the ellipse of Calibration C. This remark suggests that when the suction anchor is loaded laterally,

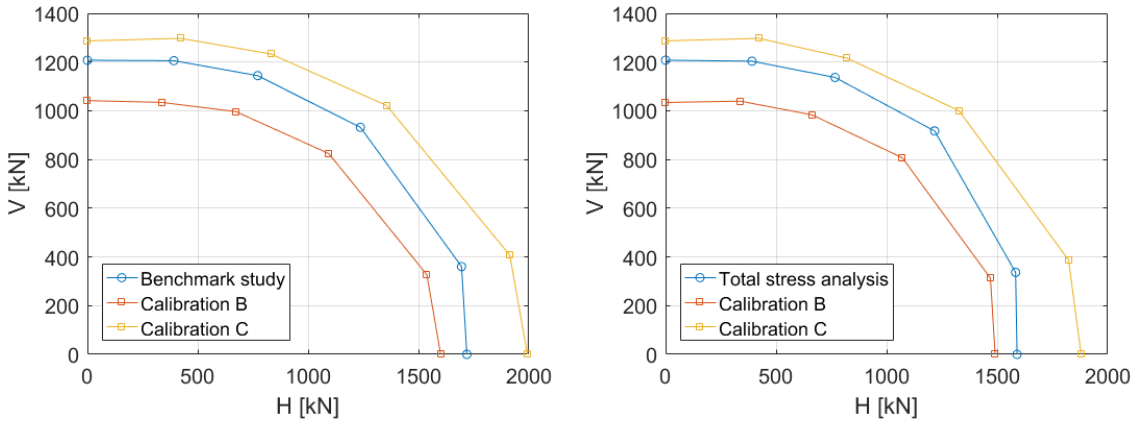

(a) $\beta = 0°$ (b) $\beta = 10°$

Figure 4.35: HV interaction diagrams of total and effective stress analysis for Calibrations B and C

compressive and shear soil resistance govern the evolution of the failure mechanisms. Conversely, extensive soil resistance appears to play a more important role when the suction anchor is pulled - out when loaded vertically.

At this point, it should be highlighted that the anchor is loaded at the depth of the padeye. Thus, when the vertical load is applied at this depth, the suction anchor does not only move vertically upwards but it also rotates backwards. This means that also compressive and shear resistance of the soil affects the bearing capacity and this might be the reason why the benchmark study curve does not coincide with Calibration C for purely vertical loading.

Figures 4.36a and 4.36b consist of the HV normalised failure envelopes without the presence of misalignment and with a misalignment angle of 10°. These graphs disclose that, regardless of the calibration, results coincide with the benchmark study with or without rotation being induced in the problem.

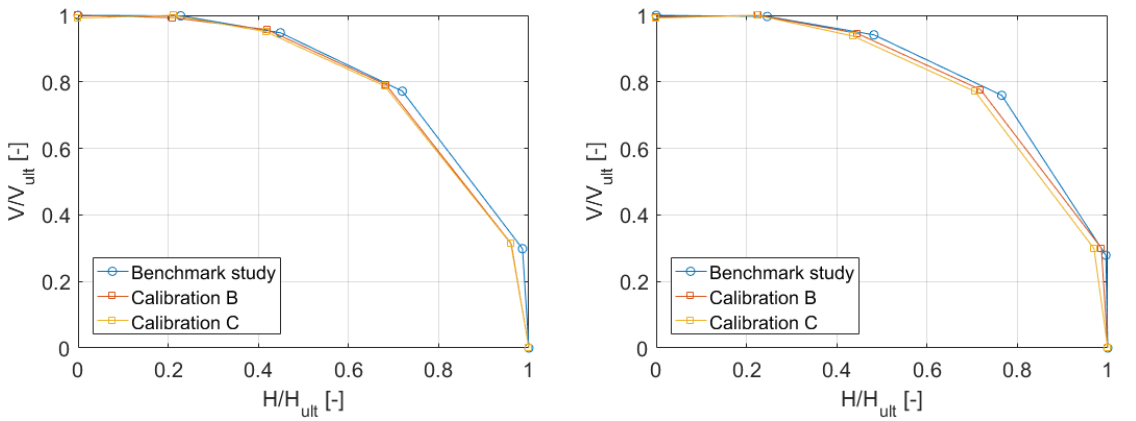

(a) $\beta = 0°$ (b) $\beta = 10°$

Figure 4.36: HV normalised interaction diagrams of total and effective stress analysis for Calibrations B and C

4.8.3 Calibrations D and E

The inspiration to create these two calibrations came from the results presented for Calibrations B and C. The goal was to create two calibrations that would have an average soil behaviour from undrained triaxial compression (TXC), extension (TXE) and direct simple shear (DSS) that is in accordance with the soil behaviour of the benchmark study. As explained in Section 4.4.2, Calibration D has the average behaviour of TXC, TXE and DSS equivalent to the benchmark study soil behaviour, whereas Calibration D has the average of TXC (or DSS) and TXE analogue to the benchmark study soil response. Apparently, the Soft Soil model parameters of these two calibrations are very close.

Numerical analysis results are presented below for the short anchor ($L = 7.5$m) in the case where no misalignment is induced in the problem and in the case where misalignment is equal to 10°. Comparative graphs from the results are drawn so that resemblances and deviations between the results of the adopted approaches can be easily evaluated. Figures 4.37a and 4.37b show that the failure loci of Calibrations D and E are very close to the bearing capacity predictions of the benchmark study.

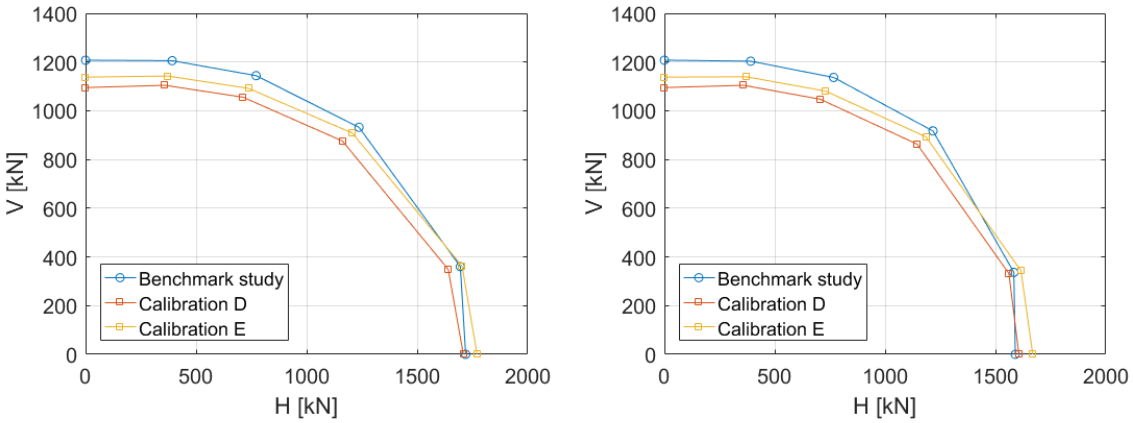

(a) $\beta = 0°$ (b) $\beta = 10°$

Figure 4.37: HV interaction diagrams of total and effective stress analysis for Calibrations D and E

As far as Calibration D is concerned, a more detailed look at these graphs uncovers that Calibration D matches precisely the benchmark study for pure lateral loading. Furthermore, it can be seen that as the vertical loading increases, Calibration D gives progressively lower bearing capacity for the anchor compared to the benchmark study. Thus, the pure vertical capacities of this calibration and the benchmark study deviate significantly. This aspect of the outcome was expected in a way as extensive soil strength plays a dominant role when the anchor is pulled - out compared to shear and compressive strength.

All of the statements made above can be regarded as true in the cases where misalignment is present and absent from the problem. When misalignment is imposed on the suction anchor, the pure lateral bearing capacity of Calibration D is slightly higher compared to the benchmark study indicating that the influence of shear soil strength is slightly greater in this case.

When Calibration E is considered, pure horizontal capacity is slightly overestimated. A perfect match with the benchmark study is accomplished when a load of 12° inclination is applied on the suction pile without misalignment. Moreover, it is apparent that as the vertical loading increases, Calibration E corresponds to a progressively lower anchor bearing capacity compared to the benchmark study. The values of the pure vertical

capacities of the two approaches are not the same but they can be regarded as very close compared to the results of all the rest of the calibrations. The aforementioned notes might be a sign that when a suction anchor is loaded with a small inclination of 12°, compressive, extensive and shear behaviour of the soil are equally important for the determination of the anchor bearing capacity.

When a misalignment angle of 10° is induced in the suction anchor at the location of the padeye, the pure horizontal capacity corresponding to Calibration E is observed to be higher than the one resulting from the benchmark study. Furthermore, it is interesting to note that, when a load of 12° inclination is imposed on the suction anchor, the result of the total stress analysis lies in between the two examined calibrations. This might indicate that the bearing capacity of the anchor is influenced to the same extent by the expensive, compressive and shear resistance of the soil. However, this assumption could only be validated with an extensive investigation on the stress paths that are followed by the points located around the anchor during this loading scenario which was not realised in the context of this study.

Figures 4.38a and 4.38b show that the normalised HV diagrams are almost identical for $\beta = 0°$ and 10° revealing that the normalised curves are not significantly influenced by the discrepancies between the two calibrations and, in addition, they are not affected by the low misalignment angle of 10°.

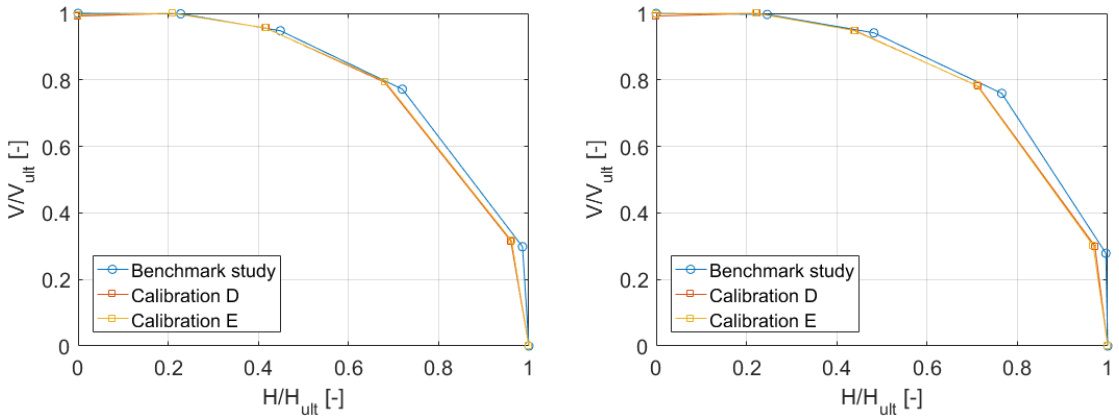

(a) $\beta = 0°$ (b) $\beta = 10°$

Figure 4.38: HV normalised interaction diagrams of total and effective stress analysis for Calibrations D and E

The limit loads that were obtained for the effective stress analysis of all calibrations within Plaxis 3D can be found in Appendix D.

Chapter 5

Numerical model in SPCalc

5.1 Introduction

In this chapter, there is a thorough description of the two dimensional approach of the undrained bearing capacity of misaligned suction anchors in clay. This approach is accomplished with the use of the geotechnical computational tool named SPCalc, which was designed especially for the calculation of the undrained bearing capacity of suction anchors.

As a start, basic features regarding the numerical modelling and computational procedures implemented in the software are available. The type of elements, the solution algorithm, the implemented constitutive model and the convergence criteria are a few of the topics discussed that reveal important aspects regarding the function of the tool.

Moreover, details concerning the actual way the suction piles are modelled using the aforementioned application are presented. All of the features that comprise the input are reported. These features consist of parameters that refer to the soil behaviour, the geometry of the structure, the loading conditions and the simulation of soil - structure interaction. Thus, similarities and discrepancies between this analysis and the one followed by the benchmark study are revealed.

Finally, the outcomes of this analysis are preseneted in the form of HV failure envelopes and are compared with the benchmark study. In this way, it can be assessed whether such a simplified approach produces trustworthy results and models satisfactorily the misalignment effect.

5.2 Description

SPCalc is a finite element software developed specifically for geotechnical applications. The software provides a convenient and user - friendly interface that enables the user to quickly define all the material and geometrical properties of the problem to be solved. It also allows for a fast generation of finite element models and offers output facilities where the computational results are shown.

The analyses conducted with this finite element tool are under 2D plane strain conditions. However, with the use of a certain type of interfaces and the implementation of specific reduction factors, SPCalc is able to account for 3D effects as well. Hence, the soil flow around the suction anchor during its loading can be captured. The comparative results with the benchmark study will unravel if the 3D effects are encompassed sufficiently by this tool.

5.2.1 Elements and interfaces

Type of elements

The soil elements of SPCalc are 8 - node isoparametric serendipity elements as reported in the work of [52]. This is is the only type of element that can be used for soil modelling by the application. As depicted in Figure 5.1, these elements are modified so that they can account also for side friction. To achieve that, an element thickness is included in y direction. Thus, these elements are suitable for the calculation of shear stresses, τ_{yx} and τ_{yz}, on the two surfaces normal to the y-axis.

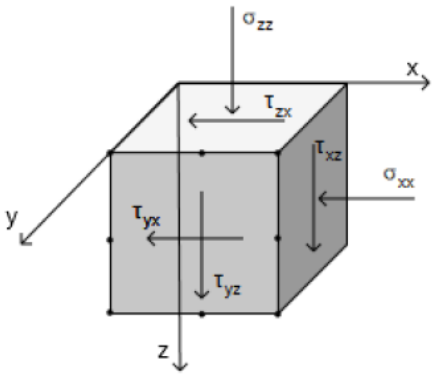

Figure 5.1: 8 - noded plane element with side friction [12]

It is noteworthy that sliding can occur only between the two fixed vertical surfaces (parallel to the x-z-plane) that have a distance equal to the element thickness.

Type of interfaces

The soil - structure interaction within SPCalc is simulated by interface elements. SPCalc is capable of using two types of interfaces.

- 6 - noded isoparametric interface elements

  The 6 - noded isoparametric interface elements, which are described by [8], are implemented in SPCalc in order to model the sliding between two 8 - noded elements. Figure 5.2 is a schematic overview showing the possible places where this type of elements are included in an SPCalc analysis. The interfaces present at the front and back side of the anchor may be modelled with non - linear normal stiffness and their performance is dependent on the set - up factor α_{out}. For all other interfaces present in the mesh, a linear normal stiffness is used coupled with a roughness factor equal to 1 representing the soil-soil contact.

- 2x8 - noded interface elements

  As shown in Figure 5.3, this type of elements are used so that the side shear in the third direction is modelled. In this way, 3D effects can be taken into account in a plane strain condition. One of the side of them is attached to an 8-noded element and one is fully fixed. These interfaces depend primarily on the reduction factors, $r_{str,out}$ and r_{soil}, that are explained in Section 5.3.

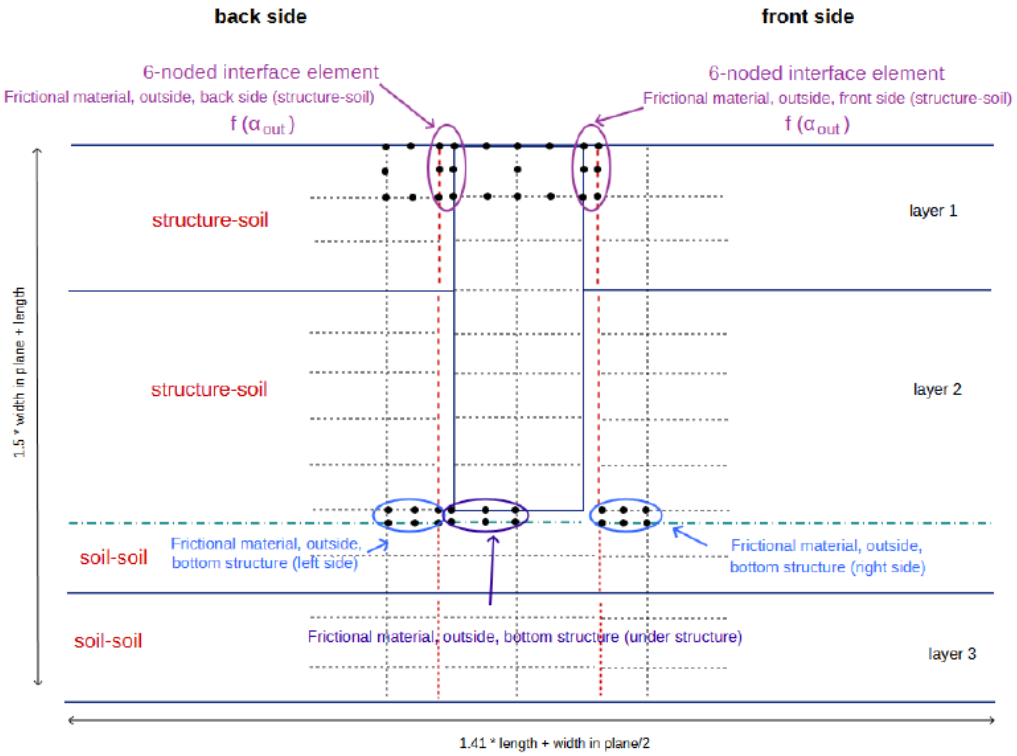

Figure 5.2: Interfaces, 2D view [12]

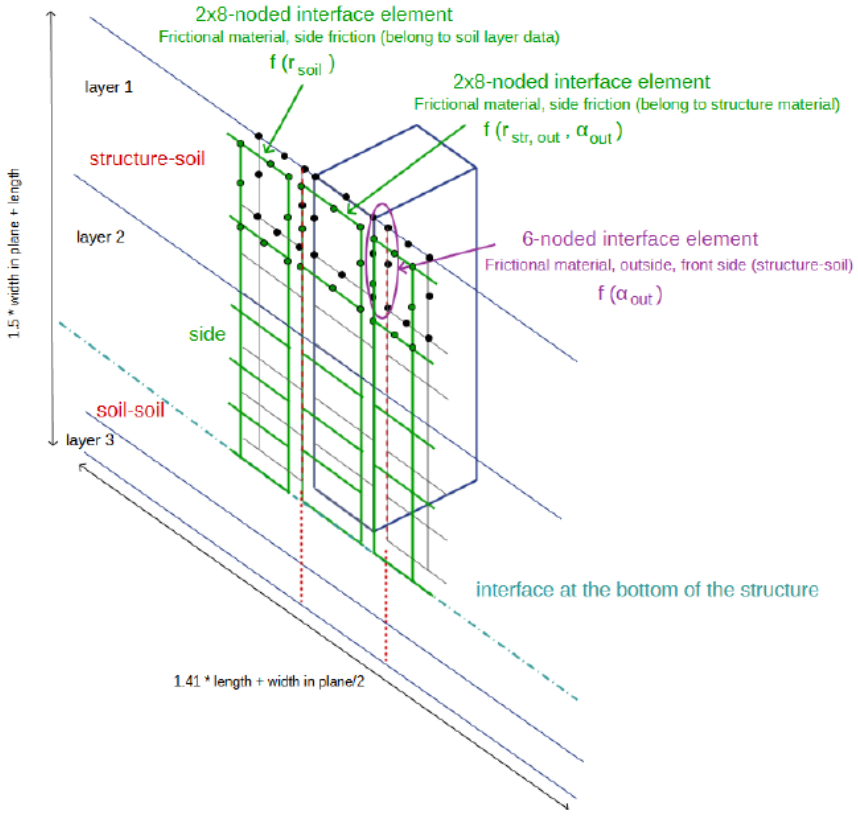

Figure 5.3: Interfaces, 3D view [12]

5.2.2 Mesh generation

The first step of the computational procedure is the finite element mesh generation, which is conducted by SPCalc automatically. It primarily depends on the geometrical characteristics of the pile and the soil stratigraphy. A relatively coarse mesh is used, which cannot be refined by the user. Additionally, the model dimensions depend on the suction anchor dimensions and are computed through the following formulas. The depth of the model in the case of a cylindrical structure is given by:

$$model\ depth = (1.5 \cdot diameter) + length \tag{5.1}$$

The vertical boundaries of the model are given by:

$$x = \pm \left(1.41 \cdot length + \frac{diameter}{2}\right) \tag{5.2}$$

Consequently, the horizontal ($z_{\min}$, $z_{\max}$) and vertical ($x_{\min}$, $x_{\max}$) boundaries of the models created for this study are given in Table 5.1.

Table 5.1: Domain sizes for SPCalc investigation

L/D [-]	$z_{\min}$ [m]	$z_{\max}$ [m]	$x_{\min}$ [m]	$x_{\max}$ [m]
1.5	0	15	-13.08	13.08
3	0	22.5	-23.65	23.65
6	0	37.5	-44.80	44.80

The finite element mesh consists of horizontal and vertical grid lines that divide the model in approximately square elements. The positioning of the horizontal lines depends on the soil layering and the base of the structure, whereas the vertical layering depends on the model boundaries and the geometry of the embedded structure.

As far as the boundary conditions are concerned, the nodes at the bottom boundary are fully fixed, while the nodes on the vertical boundaries are only fixed in the horizontal direction. The interface elements are positioned at the sides and the skirt tip level of the pile as shown in Figure 5.2.

5.2.3 NGI - ADP constitutive model

The modelling of the undrained behaviour of clay within SPCalc is accomplished through the NGI-ADP constitutive model. A plane strain version of this model is implemented in the software and it is the only material model available by SPCalc. It is considered appropriate for capacity, deformation and soil-structure interaction problems that include undrained loading of soil [12].

The work of [22] indicates that soft clays exhibit an anisotropic behaviour under different loading conditions that is captured in the most representative way by the NGI-ADP model. Its name comes from the ADP approach that was developed by the Norwegian Geotechnical Institute (NGI). The basis of the ADP approach is the simulation of the anisotropic behaviour of soft clays under Active, Direct simple shear and Passive loading.

As it is true for every constitutive model, the NGI-ADP model is composed by the following basic features.

Elastic law

The elastic constitutive matrix, D^{e}, is used for the correlation of the increment of elastic strains, de^{e}, with the increment of stresses, $d\sigma$, as seen below.

$$de^{e} = [D^{e}]^{-1} * d\sigma \tag{5.3}$$

Where:

$$D^{e} = \begin{bmatrix} K + \frac{4}{3}G & K - \frac{2}{3}G & 0 \\ K - \frac{2}{3}G & K + \frac{4}{3}G & 0 \\ 0 & 0 & G \end{bmatrix} \tag{5.4}$$

G is the linear elastic shear modulus and K is the linear elastic bulk modulus. During unloading, a pure elastic response is also adopted. The unloading modulus is taken equal to the initial shear modulus.

Yield function

In order to represent the boundary between the elastic and the plastic domain, a yield criterion based on the Tresca criterion is used. However, it is modified accordingly so that it can take into account the different undrained shear strengths under compression, direct shear and extension. Since a Tresca yield function is also used in the Benchmark study [39], the results are directly comparable. The benchmark study represents the simplest case of the NGI-ADP model as the undrained shear strength is the same for all types of loading.

The yield function f is described by the following formula.

$$f = \tau - \tau_f(\alpha) = 0 \tag{5.5}$$

Where τ is the maximum shear stress in the x - z plane that is equal to the radius of the Mohr circle:

$$\tau = \sqrt{\left(\frac{\sigma_{xx} - \sigma_{zz}}{2}\right)^2 + \tau_{xz}^2} \tag{5.6}$$

As shown in Equation 5.5 and Figure 5.4, the shear strength at failure τ_f is contingent on the angle α. The angle α is equal to the angle between the maximum principal compressive strength, σ_1, and the vertical z axis.

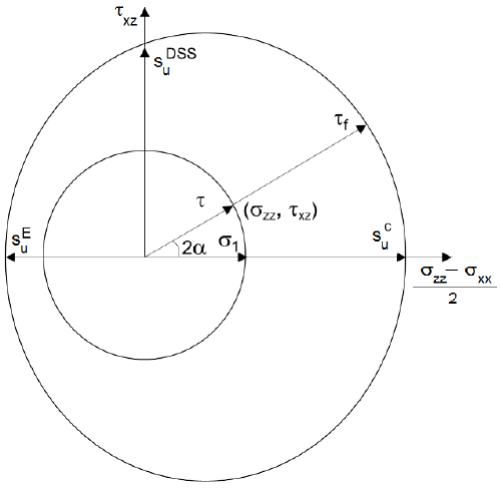

Figure 5.4: NGI - ADP yield function [12]

The three subsequent distinctive cases for this angle clarify the way in which this constitutive model works.

- For $\alpha = 0°$, the vertical stress coincides with the the maximum principal compressive stress, σ_1. Thus, the shear stress, τ_f, is equal to the undrained shear strength under triaxial compression, $s_{\mathrm{u}}^{\mathrm{C}}$.
- For $\alpha = 45°$, the shear stress, τ_{f}, is equal to the undrained shear strength under direct simple shear, $s_{\mathrm{u}}^{\mathrm{DSS}}$.
- For $\alpha = 90°$, the horizontal stress coincides with the the maximum principal compressive stress, σ_1. Hence, the shear stress, τ_f, is equal to the undrained shear strength under triaxial extension, $s_{\mathrm{u}}^{\mathrm{E}}$.

For arbitrary values of α, τ_{f} is determined through the following expression.

$$\tau_{\mathrm{f}} = S_0 + S_1 \cos(2\alpha) + S_2 \cos(4\alpha) \tag{5.7}$$

Where S_0, S_1 and $S_{2\mathrm{tgb}}$ are interpolation functions for plastic failure strains and for shear strengths along arbitrary stress paths and are given by the subsequent formulas.

$$S_0 = 0.25 \cdot (s_{\mathrm{u}}^{\mathrm{C}} + 2s_{\mathrm{u}}^{\mathrm{DSS}} + s_{\mathrm{u}}^{\mathrm{E}}) \tag{5.8}$$

$$S_1 = 0.5 \cdot (s_{\mathrm{u}}^{\mathrm{C}} - s_{\mathrm{u}}^{\mathrm{E}}) \tag{5.9}$$

$$S_2 = 0.25 \cdot (s_{\mathrm{u}}^{\mathrm{C}} - 2s_{\mathrm{u}}^{\mathrm{DSS}} + s_{\mathrm{u}}^{\mathrm{E}}) \tag{5.10}$$

Flow rule

The direction and intensity of the increment of plastic strains, de^{p}, is defined by an associated flow rule. This means that the plastic potential function g and the yield function f are assumed to coincide as expressed by Equation 5.11. As a consequence, the direction of the increments of plastic strains, de^{p}, are always normal to the yield surface.

$$d\epsilon^{\mathrm{p}} = d\lambda \frac{\partial g}{\partial \sigma} = d\lambda \frac{\partial f}{\partial \sigma} \tag{5.11}$$

In the mathematical expression shown above, $d\epsilon^{\mathrm{p}} = [d\epsilon_{\mathrm{xx}}^{\mathrm{p}},\ d\epsilon_{\mathrm{zz}}^{\mathrm{p}},\ d{\gamma_{\mathrm{xz}}}^{\mathrm{p}}]^T$ is the incremental plastic strain vector, $d\lambda$ is the positive plastic multiplier and $\sigma = [\sigma_{\mathrm{xx}},\ \sigma_{\mathrm{zz}},\ \tau_{\mathrm{xz}}]^T$.

Hardening rule

Once plasticity has been reached, the yield surface may change size, shape and position. The potential changes of the yield surface are controlled by the hardening rule. In this way, the evolution of stresses and other internal variables during plasticity is feasible. In this case, the hardening rule is based on a relation between the mobilised shear strength, τ_{m}, and the plastic shear strain, γ^{p}. The mobilised yield surface, f, is defined as:

$$f(\sigma, \gamma^{\mathrm{p}}) = \tau - \tau_{\mathrm{m}}(\gamma^{\mathrm{p}}) = 0 \tag{5.12}$$

5.2.4 Calculation process

The SPCalc calculation process involves a solution algorithm and certain stopping criteria. The purpose of the solution algorithm is the derivation of the load - displacement curve from the initial undeformed state to a steady -state failure condition as illustrated in Figure 5.5. This is achieved through the gradual increment of loads until failure.

This equilibrium curve is defined by finite element equations that aim to balance the internal forces of the system with the external applied force. This is accomplished with an incremental procedure that starts from the initial configuration and continues with the rest of the equilibrium points. A predictor - corrector scheme coupled with an automatic step size procedure makes sure that no deviation from the curve occurs during the procedure.

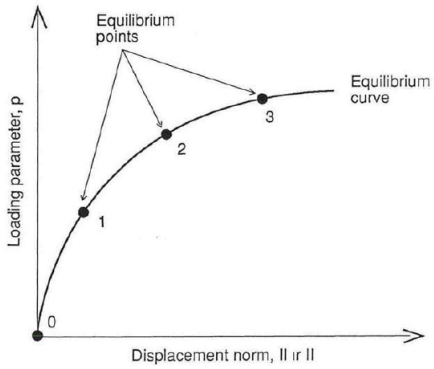

Figure 5.5: SPCalc solution curve [12]

It is true that when a non-linear analysis is carried out, there is an expected deviation of the results from the exact solution. In order to limit the equilibrium errors, SPCalc is designed to continue the iterations until the calculated errors are smaller than the convergence tolerance. The default value of convergence tolerance is 0.001 to produce a quick and accurate solution for the majority of calculations. The computational calculations finish when one of the following criteria when the failure condition has been reached and a well-defined yield plateau has been developed. In this case, the current stiffness parameter of the system becomes lower than a specified value set internally by SPCalc. This is true at the end of all the analyses carried out in this research. A maximum calculation time of 60 seconds is set for every calculation.

5.3 Input parameters

The SPCalc input parameters were chosen so that they represent the benchmark study [39] in the best possible way. Thus, comparisons of the two dimensional and the tree dimensional approach are feasible. To achieve that, special attention waas paid to the simulation of the soil stratigraphy, the geometry of the structure, the soil-structure interaction and the loading conditions.

Three projects were created in SPCalc suitable for the analyses of the suction anchors with three different aspect ratios (L/D = 1.5, 3 and 6). The parameters selected for each project are elaborated in the following paragraphs. They are divided in three categories (soil, structure and calculation mode) as it is also done for the creation of a project in SPCalc.

5.3.1 Material properties

All of the three examined anchors are embedded in homogeneous normally consolidated clay with undrained shear strength linearly increasing with depth as described by the

equation $s_u = 1.25z$. Therefore, only one single layer is adequate to represent the soil stratigraphy of each projects. The unit weight of the water is taken as 10 kN/m^2. The saturated unit weight of the NC clay is 16 [kN/m^3] for all projects. No open crack at active side is considered. The rest of the material parameters are specified as explained in the following paragraphs.

At the top of all layers $s_u^C = 0$, while at the bottom the values reported in Table 5.2 are defined based on the size of the domain in Plaxis 3D analyses. In this way, the linearly increasing strength with depth is modelled.

Table 5.2: s_u^C at the bottom of the layers

L/D [-]	z_{bottom} [m]	$s_{u\ bottom}^C$ [kN/m^2]
1.5	25	31.25
3	40	50.00
6	90	112.50

Moreover, the definition of the ratio of the undrained shear strength in direct simple shear over the undrained shear strength in compression and the ratio of the undrained shear strength in extension over the undrained shear strength in compression is mandatory. Both of them are set equal to 1 for all three projects. This is attributed to the Tresca failure surface used in the benchmark study.

Finally, The parameter α_{out} is set to a value of 0.65 as it is considered to be equal to the strength reduction factor R_{inter} used in Plaxis 3D analyses. In this way, the soil-structure interaction is modelled at the sides of the anchor taking care of the influence of adhesion.

5.3.2 Suction anchor properties

As far as the geometry of the anchor is concerned, the diameter (D = 5m) is the same for all three cases. The lengths are set to 7.5, 15 and 30 meters for the three projects respectively. The suction anchor is assumed to be placed with no tilt. The ratio of the depth of the center of gravity of the structure, measured along the structure centreline, over the length of the structure, L_{cog}/Length, can also be determined. Due to the fact that the suction pile has fully penetrated into the ground, it is set equal to the default value which is 0.5.

The material of the suction anchor is described through the anisotropic shear strength constitutive model implemented for the soil (NGI-ADP model). The only difference is that a very high shear strength is used during the calculation process. The submerged weight of the anchor is taken to be 0 as in the Plaxis 3D analyses.

It is noteworthy that the software requires that the stiffness parameters are defined, even though they do not affect the ultimate holding capacity calculation as pointed out by [12]. The elastic stiffness properties of the suction anchor are specified by:

- K/G: ratio of bulk over shear modulus, [-]

  In the benchmark study, a fully incompressible behaviour is adopted with the use of $\nu_u = 0.49$. Therefore:

$$\frac{K}{G} = \frac{3(1+\nu)}{3(1-2\nu)} = 49.67 \tag{5.13}$$

- $G/G_{soil,bottom}$: ratio of shear modulus of the structure over shear modulus of the soil at the structure tip, [-]

This ratio is set equal to 100 as the soil plug and the structure are modelled as rigid bodies in Plaxis 3D and, therefore, they are also given a very high stiffness compared to the adjacent soil in this analysis.

The anchor loading can be described by a chain load F_c applied at the padeye of the anchor, which is assumed to be positioned exactly on the wall of the anchor at a depth of $0.7L$. Subsequently, this load is translated to a vertical (F_V), horizontal (F_H) and moment load (M) at the top of the anchor as illustrated in Figure 5.6. The derivation of HV failure loci is accomplished through the application of loads with different angles $\alpha_{\text{inclination}}$ from 0° to 90°. The investigation of the influence of misalignment on the anchor bearing capacity is accomplished by creating and comparing HV diagrams for $\beta_{\text{mis-orientation}} = 0°$, 5° and 10°. In SPCalc, the range of $\beta_{\text{mis-orientation}}$ is between 0° and 15° as stated in Section 3.4.2.

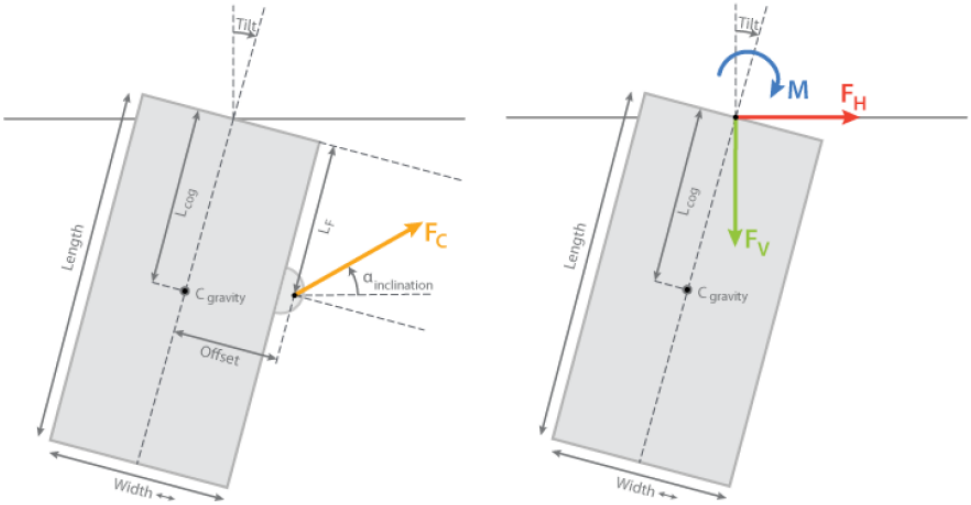

Figure 5.6: Loading conditions using SPCalc [12]

5.3.3 Reduction factors for 3D effects

SPCalc accounts for 3D effects through the implementation of two reduction factors, $r_{\text{str,out}}$ and r_{soil}, that are employed for the out of plane interfaces as illustrated in Figure 5.3. Both factors are important in order to capture the different failure mechanisms that develop when an anchor is loaded with different inclinations between the horizontal and the vertical direction. The factor $r_{\text{str,out}}$ is used to simulate the reduction of the interface shear strength on the out of plane structure area as depicted in Figure 5.3. Respectively, the factor r_{soil} is used to model the reduction of interface shear strength on the soil side area.

For a pure vertical load, the factor $r_{\text{str,out}}$ plays a more significant role on the determination of the anchor bearing capacity compared to r_{soil} as the bearing capacity of the pile hinges primarily on the shaft friction. For a pure horizontal loading, the factor r_{soil} becomes more important for the calculation of the bearing capacity with respect to $r_{\text{str,out}}$ as a larger area of soil flows around the anchor during loading. In any case, if values less than 1 are implemented for the reduction factors described above, a reduced interface shear strength in the aforementioned planes is modelled.

SPCalc proposes two default values for the reduction factors, which are $r_{\text{str,out}} = 0.73$ and $r_{\text{soil}} = 0.6$. These values are calibrated according to 3D finite element analyses for different soil profiles, loading conditions and anchor shapes. They are also validated with the experience gained by NGI from several projects and tests. A new calibration would be required only in the case of special soil profiles. Therefore, the default values are also used for this study.

5.3.4 Numerical control parameters

The numerical calculations realised with SPCalc are dependent on the numerical control parameters. The values that were chosen under the scope of this study are presented in Table 5.3. The first one refers the convergence tolerance which is equal to the default value 0.001. Lower values cannot be specified as in this case the software produces an error indicating that the minimum allowable load increment has been reached, see Section 5.2.4.

The load factor is a load multiplier that reveals the percentage of the chain force that has been applied on the pile when failure is reached. The load factor starts from a value of 0.01 and constantly increases during the iteration procedure. The maximum load factor is set to 3 and cannot be modified by the user. If this value is reached, it means that the project should be considered safe for the current applied load, which is not true for any of the analyses of this study.

A maximum anchor displacement $D_{\max}$ of 1.5 meters is determined as proposed by SPCalc. It has been observed that analyses beyond this maximum displacement are considered time - consuming and unnecessary as the full capacity of the anchor has been mobilised within this magnitude of displacement.

Table 5.3: Numerical control parameters of SPCalc

Parameter	**Value**
Convergence tolerance	0.001
Initial load factor	0.01
$D_{\max}$	1.5
N_{incr}	200

5.4 Results and discussion

The results obtained from the numerical calculations of SPCalc are presented in the convenient form of horizontal - tensile (HV) failure envelopes that reveal the influence of various loading combinations on the anchor bearing capacity. In this way, the influence of misalignment as well as the anchor length on the load bearing capacity can also be evaluated. The loading scenarios involve three different misorientation angles ($\beta = 0°, 5°$ and $10°$) and three distinctive aspect ratios (L/D = 1.5, 3 and 6). Additionally, normalised HV interaction diagrams are presented. The values of these diagrams are computed by dividing the anchor bearing capacities of different load inclinations with the ultimate one. This means that H_{ult} corresponds to a pure horizontal load of 0° inclination and V_{ult} is correlated with a pure vertical load with an inclination of 90°.

Figures 5.7a, 5.8a and 5.9a depict the aforementioned HV interaction diagrams for all aspect ratios. For each one of the aspect ratios, HV interaction diagrams corresponding to different misalignment angles are also drawn so that relevant comparisons can be made. A more detailed look at the same graphs reveals that the failure envelopes for all aspect ratios tend to shrink as the angle of misalignment increases, which means that misalignment has a negative impact on the bearing capacity of the anchors. It is interesting to note that the ultimate vertical capacity coincides for all misalignment angles, which indicates that the pull - out capacity is not influenced by the presence of torsion as it was also observed in the Plaxis 3D analysis of the benchmark study, where a wider range of misalignment angles were examined from 0° to 90°.

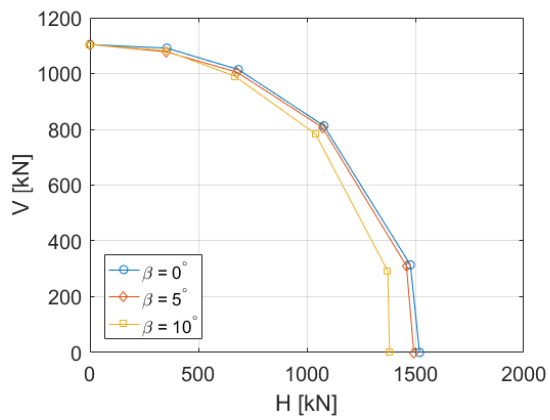

(a) HV interaction diagram

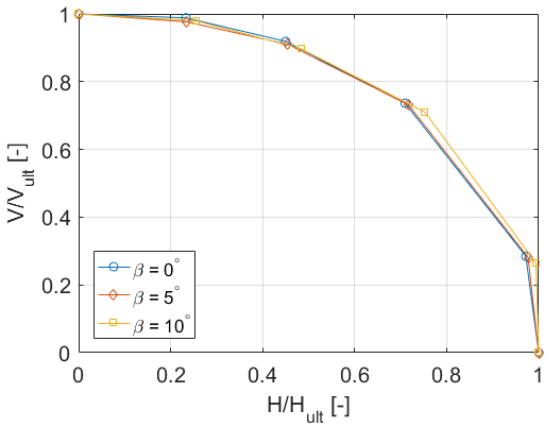

(b) HV normalised interaction diagram

Figure 5.7: SPCalc results for L/D = 1.5

On the other hand, it is apparent that misalignment has a significant impact on the pure lateral capacity of the anchor, which is more profound as the aspect ratio increases. More precisely, an increase of the misalignment angle, β, from 0° to 10°, leads to a 9%, 6% and 4% decrease of the pure lateral capacity of the short, medium and long anchor respectively.

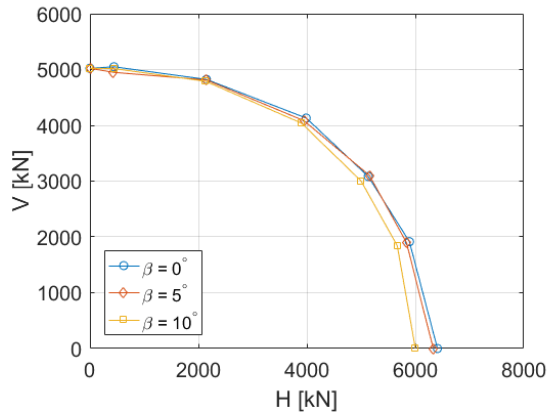

(a) HV interaction diagram

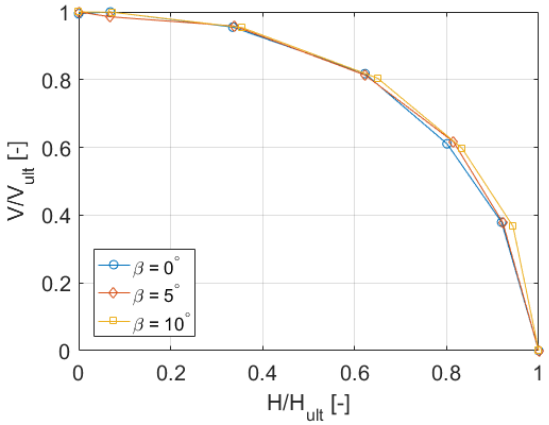

(b) HV normalised interaction diagram

Figure 5.8: SPCalc results for L/D = 3

Figures 5.7b, 5.8b and 5.9b illustrate the normalised HV interaction diagrams for all aspect ratios. These plots reveal that the shape of the normalised failure loci is not affected by low misalignment angles ($\leq 10°$) as the plots for different β angles of each one of the aspect ratios coincide. It is interesting to note that this phenomenon was also obrserved in the results of Plaxis 3D carried out in the context of the benchmark study [39].

Consequently, the numerical data of each analysis, which corresponds to one aspect ratio, can be interpolated with one elliptical curve that is described by Equation 2.6. This can accomplished by adjusting the shape coefficients (a and b) to fit satisfactorily the data. Figures 5.10a, 5.10b and 5.10c illustrate the elliptical fits determined through the aforementioned procedure.

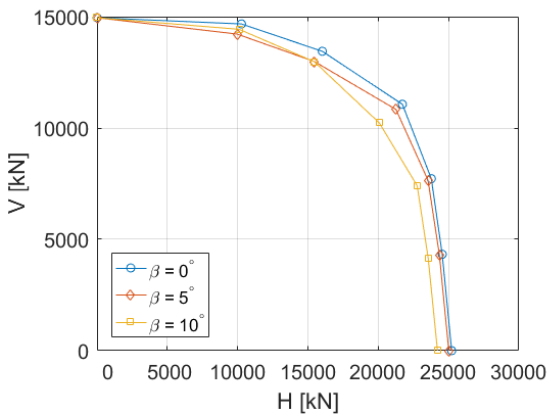

(a) HV interaction diagram

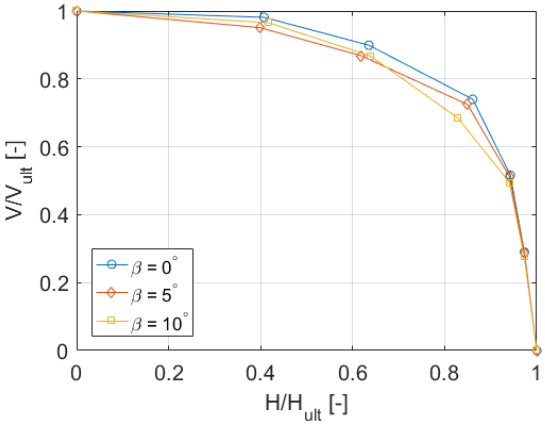

(b) HV normalised interaction diagram

Figure 5.9: SPCalc results for L/D = 6

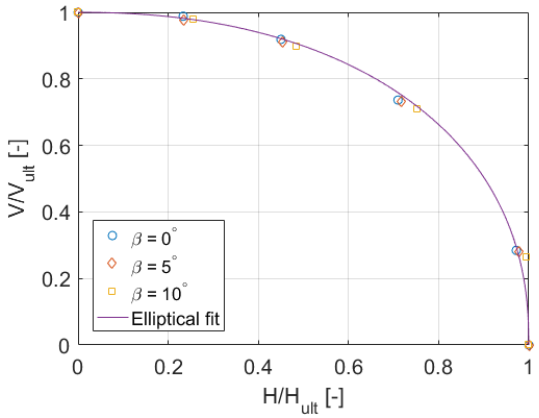

(a) L/D = 1.5

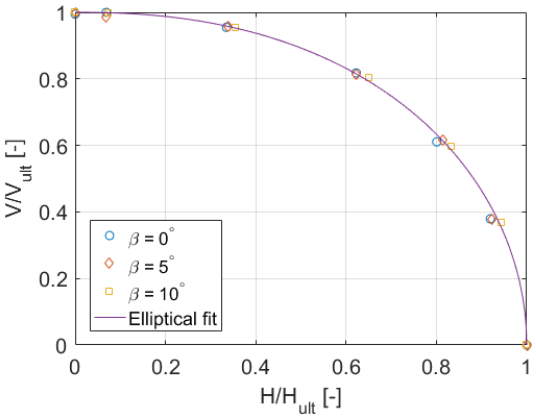

(b) L/D = 3

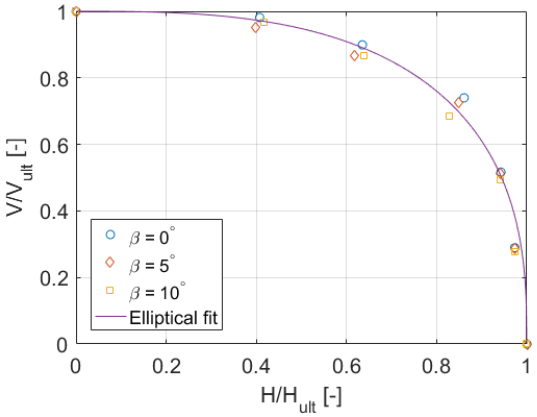

(c) L/D = 6

Figure 5.10: Elliptical curves integrated for the numerical data of all aspect ratios

Table 5.4 shows the determined shape coefficients, a and b, for SPCalc in comparison to the ones determined for the benchmark study.

Table 5.4: Shape coefficients, a and b, for all aspect ratios of SPCalc and Plaxis 3D results

Aspect ratio	**SPCalc Analysis**		**Total Stress Analysis**	
L/D [-]	a [-]	b [-]	a [-]	b [-]
1.5	2.2	2.3	2.18	2.9
3	2.3	2	2.54	2.48
6	2.9	2.7	5.33	2

5.5 Comparison between SPCalc and Plaxis 3D results

The main purpose of this section is to reveal the similarities and discrepancies between the results that stemmed from the three dimensional analysis of the benchmark study using Plaxis 3D and the two dimensional analysis using SPCalc. Initially, the magnitude of the reduction of the ultimate horizontal capacity with respect to misalignment is investigated. Furthermore, the influence of the anchor length on the pure vertical and lateral capacity of the anchors is also examined. All the aforementioned results are assessed and discussed in the following paragraphs. Moreover, comparative HV failure envelopes are drawn for all aspect ratios so that potential differences between the two approaches in the prediction of the overall bearing capacity are unveiled.

5.5.1 Reduction of ultimate lateral capacity due to misalignment

It is important to note that the decrease of the overall anchor capacity due to misalignment is related to the reduction of the ultimate horizontal capacity, as the ultimate vertical capacity remains uninfluenced by the introduction of torsion into the problem.

One way to investigate the reduction of the lateral bearing capacity of the anchors as computed by the two approaches is through the lateral capacity factor, N_{h}, which is also described in Section 2.3.1. This factor, N_{h}, is computed through Equation 5.14 and allows for the determination of the normalised lateral capacity of the anchor. This is also apparent in Equation 5.14, where the bottom resistance of the caisson is subtracted by the ultimate lateral capacity, H_{ult} and then the outcome is normilised with reference to the anchor geometry and the soil shear strength.

$$N_{\mathrm{h}} = \frac{H_{\mathrm{ult}} - A\, s_{\mathrm{u,tip}}}{L\, D\, \overline{s_{\mathrm{u}}}} \tag{5.14}$$

Once this factor is plotted against the sinus of the misalignment angle (Figure D.18), it is obvious that an increase of β angle leads to a decline of the the normalised lateral capacity for all aspect ratios of both analysis. Moreover, the predicted lateral capacity of all the anchors resulting from SPCalc (Figure 5.11a) is remarkably lower compared to Plaxis 3D (Figure 5.11b).

A further research is conducted regarding the actual reduction of ultimate lateral capacity with respect to the misalignment angle. The ratio of the ultimate lateral capacity at different misalignment angles, $H_{\mathrm{ult},\beta}$, divided by the ultimate lateral capacity when no torsion is present, $H_{\mathrm{ult},\beta=0^\circ}$, is computed. In Figure 5.12a, the plot of this ratio against $\sin\beta$ is presented, which unveils that this ratio always reduces with an increase in of the torsional angle. A more detailed look at this graph reveals that the decrease of H_{ult} is greater when the shortest anchor is considered ($L/D = 1.5$) for SPCalc.

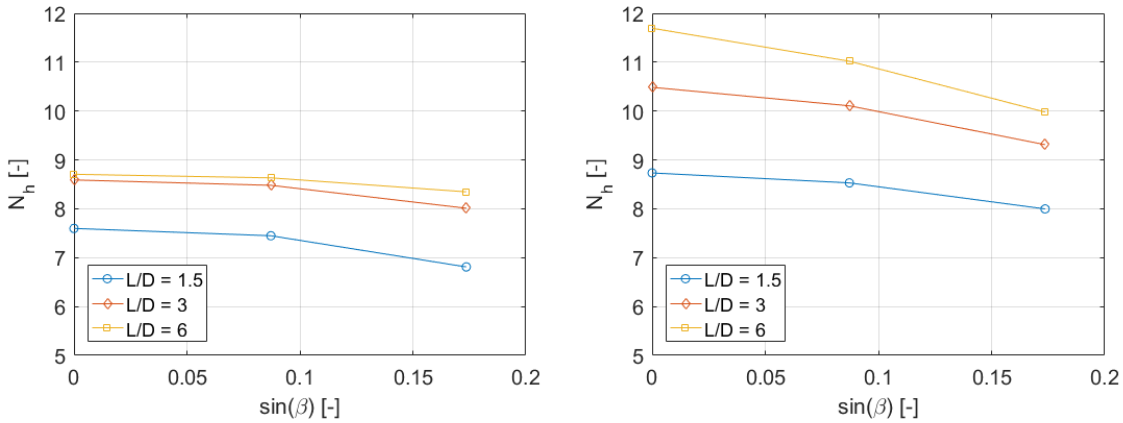

(a) SPCalc (b) Plaxis 3D

Figure 5.11: Lateral capacity factor, N_{h}, relationship with $\sin\beta$ for all aspect ratios of SPCalc and Plaxis 3D analyses

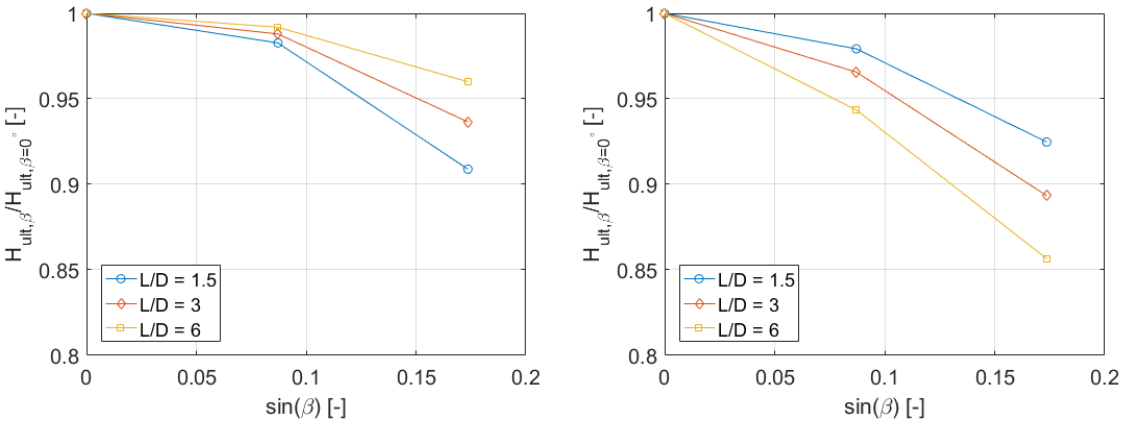

(a) SPCalc (b) Plaxis 3D

Figure 5.12: $H_{\mathrm{ult},\beta}/H_{\mathrm{ult},\beta=0^\circ}$ relationship with $\sin\beta$ for all aspect ratios of SPCalc and Plaxis 3D analyses

Figure 5.12b is an equivalent plot to the one described previously and depicts the relationship between $H_{\mathrm{ult},\beta}/H_{\mathrm{ult},\beta=0^\circ}$ and $\sin\beta$ of the analyses carried out within Plaxis 3D. A comparison between the aforementioned graphs unveils that the decrease of the lateral capacity is for all aspect ratios more intense for Plaxis 3D. Furthermore, it is interesting to note that, although the highest decrease of H_{ult} is noticed for the shortest anchor ($L/D = 1.5$) for SPCalc, Plaxis results show the exact opposite pattern proposing that the H_{ult} of the longest anchor ($L/D = 6$) is the one most significantly affected by misalignment.

Since only a limited number of mathematical formulas are available by [12] that give an insight into the internal calculations carried out by SPCalc, it is hard to draw conclusions on the reason why this phenomenon takes place. A reference can only be made to Equation 3.3 that suggests that an increase of the misalignment angle leads to a reduction of the adhesion factor and, consequently, lower anchor capacity. However, the reduction of adhesion is also dependent on the geometry of the anchor. Taking the same mathematical formula into consideration, it can be argued that the length of the pile (L) is negatively correlated with the reduction of adhesion as higher lengths increase the torsional capacity, M_{max} of the pile which is also present in the formula. This could explain why a notewor-

thy increase of the length of the anchor leads to a lower reduction of adhesion factor and, thus, the anchor capacity and the resulting $H_{ult,\beta}/H_{ult,\beta=0^\circ}$ ratio is grows.

5.5.2 Increment of ultimate bearing capacities with aspect ratio

As stated above, the analysis conducted in SPCalc involved three different suction anchors that are characterised by aspect ratios equal to 1.5, 3 and 6. The aspect ratio varies as the length of the anchors are selected to be 7.5, 15 and 30 respectively. Hence, observations concerning the influence of the aspect ratio on the horizontal and vertical capacity are possible.

The influence of the aspect ratio on lateral capacity can be evaluated by plotting the normalised lateral capacity factor, N_h, against the L/D values. This plot is presented in Figure 5.13a, where results from SPCalc and Plaxis 3D are available. Apparently, longer suction piles lead to greater magnitudes of lateral capacity both for Plaxis 3D and SPCalc analyses. It is also remarkable that SPCalc results are more conservative and the increase of N_h is lower compared to the three dimensional approach. The third line that is drawn in this graph stems from the displacement - controlled numerical analyses of [45] where a suction anchor is subjected to torsion and displacement.

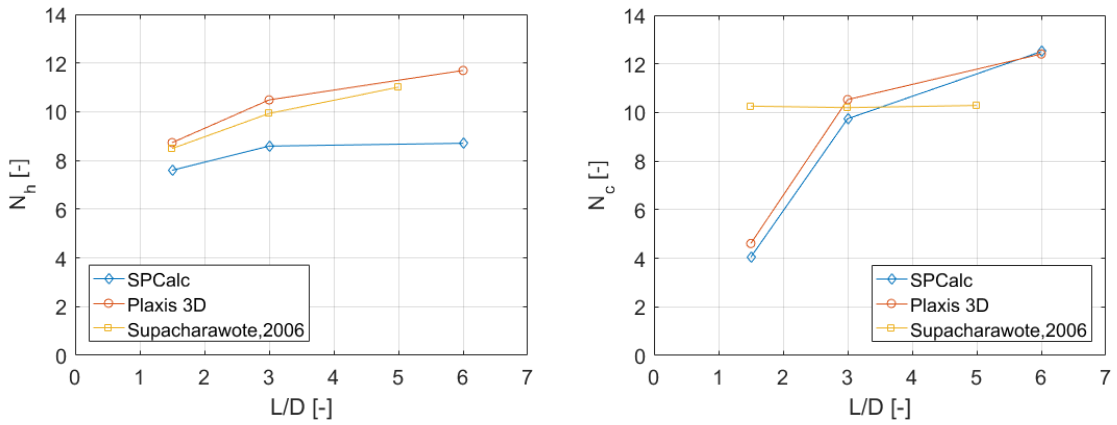

(a) N_h variation with aspect ratio (b) N_c variation with aspect ratio

Figure 5.13: Lateral capacity factor, N_h, and end bearing capacity factor, N_c variation with aspect ratio of SPCalc analyses, Plaxis 3D analyses and results from [45]

In order to assess the degree of influence that aspect ratio has on the magnitude of the vertical capacity, it is convenient to compute the reverse end bearing factor, N_c, that is further explained in Section 2.3.1. This factor expresses the (normalised) unit base resistance of the anchor and, for its calculation by Equation 5.15, the shaft resistance is subtracted from the ultimate vertical capacity V_{ult} and then the outcome is normalised with respect to the anchor geometry and soil shear strength. Figure 5.13b unveils a relatively sharp increase of the anchor vertical capacity with respect to aspect ratio. In this case, results coming from the two dimensional and the three dimensional approach are very close.

$$N_c = \frac{V_{ult} - \alpha\, \overline{s_u}\, S}{A\, s_{u,tip}} \tag{5.15}$$

It is worth noting that the results coincide for the long anchor ($L/D = 6$). This can be attributed to the fact that, for such a long suction pile ($L = 30$m), it is true that its capacity is governed by the shaft resistance, while the reverse end bearing mechanism

plays a minor role. As a consequence, in this case, SPCalc prediction is closer to Plaxis 3D as its difficulty to capture the reverse end bearing mechanism does not influence the results in a sufficiently great way.

The reason why the line stemming from the numerical data of [45] does not follow a similar upward trend is that the analyses of this research are displacement - controlled. Additionally, in this study rotation is not allowed when the anchor is pulled out, which would consume some of the resistance. Other reasons for the evident discrepancies are different meshes used for the modelling of the problem and different displacements at which the analyses were concluded.

5.5.3 HV failure envelopes

As a start, the results are compared in the form of HV failure envelopes and HV normalised failure envelopes. Hence, it can be easily observed whether the results coincide or deviate. In addition, the trends of the results coming from the two approaches, when the suction anchors are subjected to combined loading, can be compared.

Figures 5.14a, 5.15a and 5.16a reveal that, for the whole range of misalignment angles examined, SPCalc predicts lower anchor bearing capacity for all aspect ratios comprared to Plaxis 3D results. Therefore, in all these graphs the three lower curves always correspond to SPCalc, whereas the three upper ones to Plaxis 3D. Even though this phenomenon seems to be untrue for the long anchor (Figure 5.16a), where there is a sharp transition observed in the upper part of the curves that correspond to Plaxis 3D results, this steep inclination is attributed to the lack of results from the benchmark study for loading angles between 20.81° and 90°. If the missing results were available, then the curves coming from Plaxis 3D analysis would still be on top.

Figures 5.14b, 5.15b and 5.16b demonstrate the elliptical curves of SPCalc and Plaxis 3D analyses that are obtained after normalisation and the elliptical interpolation of the numerical data using Equation 2.6. It is obvious that that shapes of the plotted ellipses are very similar for both analysis for all aspect ratios. This remark suggests that the main differences between the two approaches originate from the prediction of pure lateral and pull - out capacity of this problem.

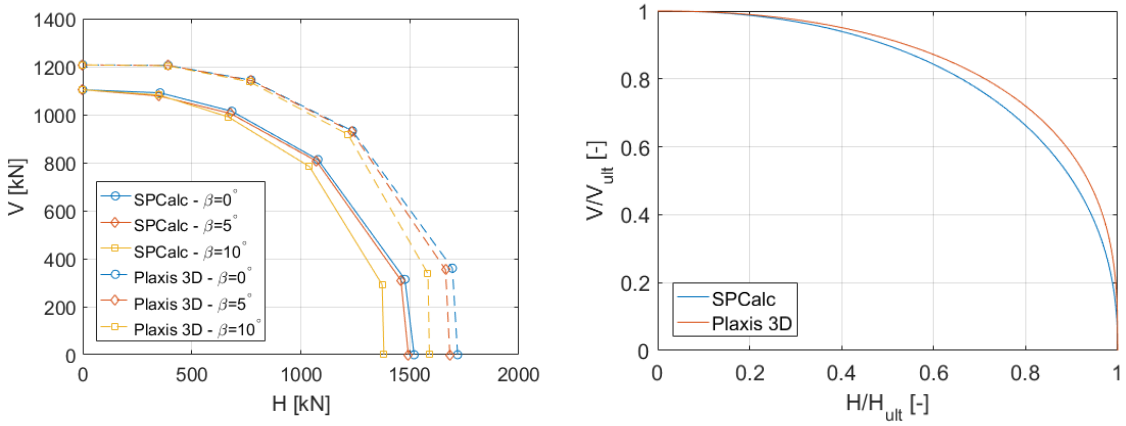

(a) HV interaction diagrams

(b) Elliptical curves

Figure 5.14: Comparison of (a) HV interaction diagrams and (b) elliptical curves stemming from SPCalc and Plaxis 3D analyses for L/D = 1.5

One possible explanation for the evident disagreement in the results depicted in Figures 5.14, 5.15 and 5.16 could be that the bearing capacity of the anchor is concluded at different anchor displacements between the two approaches. This is schematically explained in 5.17.

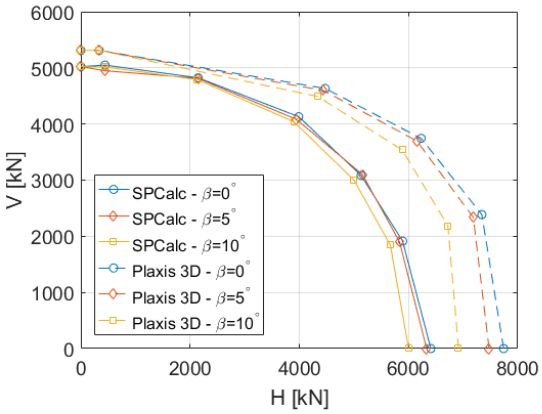

(a) HV interaction diagrams

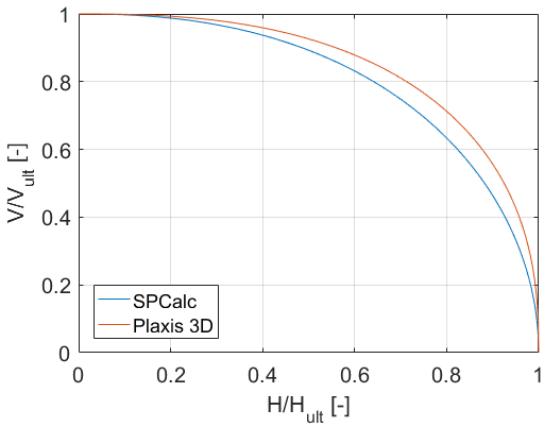

(b) Elliptical curves

Figure 5.15: Comparison of (a) HV interaction diagrams and (b) elliptical curves stemming from SPCalc and Plaxis 3D analyses for L/D = 3

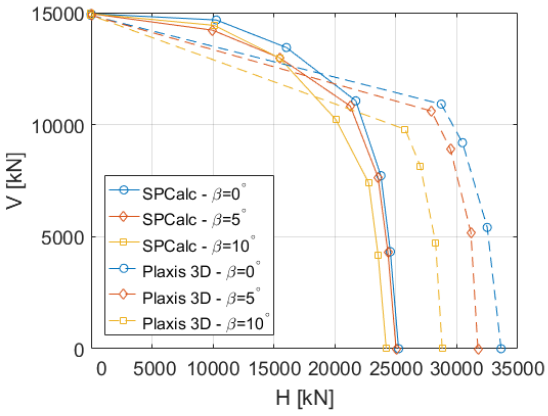

(a) HV interaction diagrams

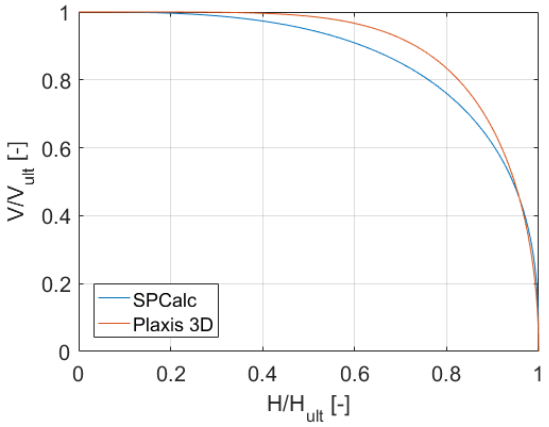

(b) Elliptical curves

Figure 5.16: Comparison of (a) HV interaction diagrams and (b) elliptical curves stemming from SPCalc and Plaxis 3D analyses for L/D = 6

For SPCalc, the maximum displacement of the anchor is not controlled by the user as the analyses stop when the stiffness of the system is minimised and, thus, failure is reached. However, the analyses stop at an early stage of the plateau of the load - displacement curve, where displacement is less than 1.5 meters. On the other hand, during the calculations performed within Plaxis 3D, well - defined plateau of the load - displacement curves are formed as the analyses continue for several meters of anchor displacement until failure is reached. At this point, there is an indication the soil body seems to collapse. Thus, in Plaxis calculations, even though failure has been theoretically reached, the capacity of the anchor keeps increasing slightly.

Figure 5.17a consists of two load - displacement curves coming from the pure horizontal load of the short anchor without misalignment. The displacement is related to a point located at the center of the top cap of the anchor. In this case, the bearing capacity of the anchor is concluded for Plaxis at 2 meters displacement, whereas for SPCalc at 0.5 meters of displacement. In Plaxis calculations, the capacity from 0.5 to 2 meters of displacement increases by 1%. Assuming that a similar increase would take place in SPcalc, then the dotted blue line would be approximately followed showing that the results of these two

approaches are still different in the end. In Figure 5.17b, the same comparison is made but in this case the anchor is loaded vertically without rotation. Even though the increase of Plaxis 3D results is more important (around 1.25%) from the point that SPCalc stops the analysis, the results are still different but closer.

As a consequence, the initial hypothesis of having different capacities from the two approaches due to different anchor displacements is not true. Taking all the above into consideration, it can be argued that SPCalc is always more conservative than Plaxis 3D, which is an aspect that was somehow expected. SPCalc is a two dimensional tool that involves a significant number of assumptions about the soil, the anchor and their interaction during loading. These assumptions make the simulation of this problem within SPCalc representative of the actual conditions but not as realistic as in the simulation of Plaxis 3D and, thus, SPCalc results are smartly designed to be always on the safe side. The presented discrepancies can be attributed to the fact that SPCalc cannot capture sufficiently the three dimensional failure mechanisms that develop when the load inclination imposed on the anchor varies. Furthermore, the deviation between the results might also be caused by the fact that the end bearing mechanism cannot be captured within the SPCalc calculation as well as it is captured in a 3D analysis.

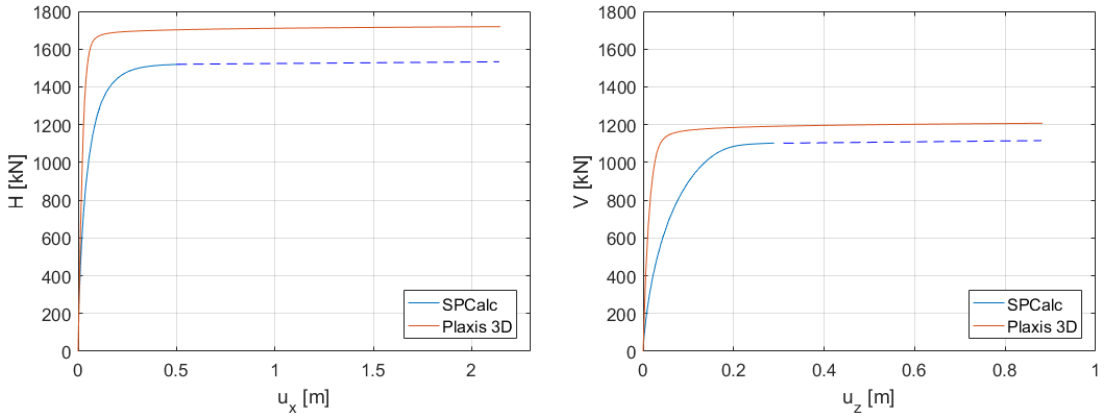

(a) Lateral load - lateral displacement curves (b) Vertical load - vertical displacement curves

Figure 5.17: Comparison of load - displacement curves from SPCalc and Plaxis 3D analyses

The limit loads that resulted from all the calculations conducted within SPCalc are available in Appendix E.

Chapter 6

Conclusions and recommendations

6.1 Concluding remarks

In this study, finite element analyses were conducted for the investigation of the undrained bearing capacity of misaligned suction anchors that are founded in normally consolidated clay and are subjected to horizontal - vertical - torsional (HVT) loading. The numerical analyses involved a 3D effective stress approach and a 2D simplified approach of the same problem. The results were compared with a benchmark study that followed a 3D total stress approach. The conclusions drawn by this comparative study are divided in two distinctive categories that correspond to the two current numerical approaches conducted in the context of this research.

6.1.1 Effective Stress Analysis with Plaxis 3D

The use of an advanced constitutive model coupled with an effective stress analysis enhances the accurate prediction of the actual soil behaviour under the undrained loading of a suction anchor. In this way, numerical analyses can capture sufficiently the evolution of effective stress paths and the generation of pore water pressures. However, the numerical implementation of a complicated material model requires a significant number of assumptions to be made about the model parameters. Furthermore, this effective stress framework poses additional difficulties about the soil parameter calibration.

It was interesting to note that the HV interaction diagrams stemming from the effective stress analysis of two distinctive calibrated models with $\phi' = 18^\circ$ and 22°, which produce precisely the compressive and shear behaviour of the benchmark study, coincide. Thus, it can be concluded that the overall bearing capacity of the anchor is primarily dependent on the peak strength of the soil and not on the amount of pore pressures generated until failure is reached that is different for these two examined cases.

A representative calibration is thought to be the one that reflects the failure mechanisms that develop around the anchor during loading involving compressive, extensive and shear stress paths. Although this seems relatively easy to be determined for one loading scenario, the application of inclined anchor loading in the range of 0° to 90° constitutes the decision on the dominant failure mechanism rather difficult. Hence, the following calibrations of the Soft Soil constitutive model have been realised in order to capture the undrained soil behaviour of the benchmark study that is modelled in the well - established framework of Tresca plasticity under differnet types of loading.

- Calibration B: Matching triaxial compression (TXC) and direct simple shear (DSS)
- Calibration C: Matching triaxial extension (TXE)
- Calibration D: Matching the average of TXC, TXE and DSS

- Calibration E: Matching the average of TXC (or DSS) and TXE

A summary of the results depicted in Figure 6.1, in the form of HV interation diagrams, shows that, when the anchor is loaded with a load inclination of less than 12°, the soil around the anchor is subjected to compression, extension and shear in an equal manner. Moreover, as the inclination of loading increases, the extensive failure mechanism becomes progressively more important. It is believed that if the anchor was pulled out from the top cap and not from the depth of the padeye, then the ultimate vertical capacity would be very similar to the one predicted from the calibration matching extension.

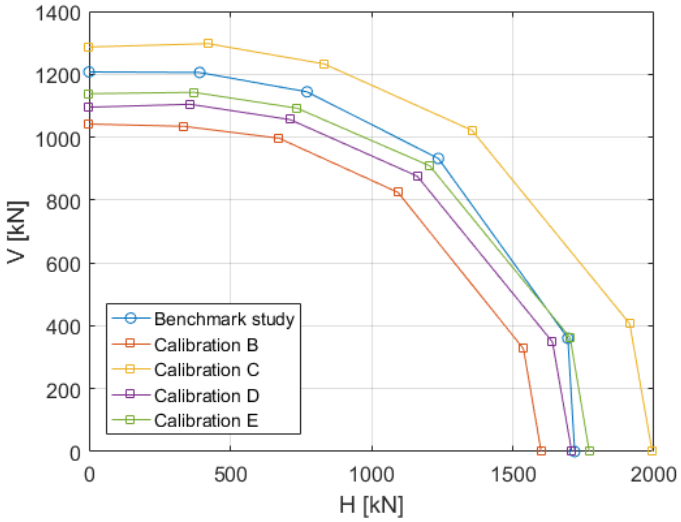

Figure 6.1: Comparison of HV failure envelopes from the current effective stress analyses and total stress analysis of benchmark study for $L/D = 1.5$

Taking all the above into consideration, it is apparent that calibrations that aim to match the average of soil behaviour coming from different types of loading are the most suitable ones to be employed for this type of problem that involves different loading inclinations causing the interchange of importance between the developed failure mechanisms.

6.1.2 Analysis with SPCalc

The results of the simplified two dimensional approach, adopted for the determination of the bearing capacity of misaligned suction anchors installed in NC clay, showed that the ultimate vertical capacity of the anchors is not influenced by the presence of torsion. On the contrary, the influence of misalignment is considered non - negligible for the ultimate horizontal capacity of the anchor. In particular, an increase of the misalignment angle, β, from 0° to 10°, leads to a 9%, 6% and 4% decrease of the pure lateral capacity of the short, medium and long anchor respectively.

A comparison of the derived HV interaction diagrams with the 3D approach of the benchmark study reveals that SPCalc is in any case more conservative with respect to the equivalent 3D numerical analysis carried out by the benchmark study within Plaxis. Considering the identical shapes of the HV normalised failure envelopes for all aspect ratios of these two methods, it can be argued that the main differences between them originate from the prediction of pure lateral and pull - out capacity of the anchors.

Having excluded that the evident discrepancies stem from the conclusion of numerical calculations at different anchor displacements for the two approaches, it can be claimed that SPCalc leads to lower anchor capacities so that it always remains on the safe side. This is the only way that the inevitable assumptions made for numerical convenience about

the soil behaviour and the soil - interaction are compensated. Additionally, even though SPCalc aims to capture the 3D effects that govern the evolution of the failure mechanisms under different types of loading through the application of certain reduction factors, it is apparent that the complexity of the reverse end bearing mechanism is not sufficiently simulated by its 2D plain strain calculations.

Finally, emphasis should be given to the fact that the computational time required for the simplest loading scenario in Plaxis 3D is approximately 3 hours, while all loading scenarios can be run in less than a minute in SPCalc. Therefore, it can be argued that SPCalc is a very fast and straightforward numerical tool that produces consistent and relatively conservative results concerning the bearing capacity of suction anchors.

6.2 Recommendations for further research

Although this study constitutes an extensive comparative research of the undrained bearing capacity of misaligned suction anchors installed in normally consolidated clay, additional parametric investigations are still required in the same direction. A number of possible relevant inquiries are listed below.

- A thorough investigation on the stress paths that are followed around the anchor during different types of loading would be very useful to assess the governing failure mechanisms that develop under different loading scenarios.
- Effective stress analyses of the presented calibrations for all anchor aspect ratios could be conducted.
- The whole range of misalignment angles (from 10° to 90°) would be interesting to be investigated following an effective stress analysis.
- Different anchor diameters, D, and soil - anchor interface resistances could be examined.
- Other soil conditions could be investigated involving distinctive soil layers.
- The suitability of other advanced constitutive models for an effective stress analysis could be researched.

References

[1] Allersma, H. G. B., Kirstein, A. A., Brinkgreve, R. B. J., & Simon, T. (1999, January). Centrifuge and numerical modelling of horizontally loaded suction piles. In The Ninth International Offshore and Polar Engineering Conference. International Society of Offshore and Polar Engineers.

[2] Andersen, K. H., Murff, J. D., Randolph, M. F., Clukey, E. C., Erbrich, C. T., Jostad, H. P., & Supachawarote, C. (2005, September). Suction anchors for deepwater applications. In Proceedings of the 1st International Symposium on Frontiers in Offshore Geotechnics, ISFOG, Perth (pp. 3-30).

[3] Andersen, K. H., Dyvik, R., Schrøder, K., Hansteen, O. E., & Bysveen, S. (1993). Field tests of anchors in clay II: Predictions and interpretation. Journal of Geotechnical Engineering, 119(10), 1532-1549.

[4] API. (1993). Reccomended practice for planning, designing and constructing fixed offshore platforms - working stress design, API-RP-2A, 20th edition, American Petroleum Institute, Washington.

[5] Api.org. (2016). Offshore Production Facilities. , http://www.api.org

[6] Aubeny, C. P., Han, S. W., & Murff, J. D. (2003). Inclined load capacity of suction caissons. International Journal for Numerical and Analytical Methods in Geomechanics, 27(14), 1235-1254.

[7] Basack, S., & Sen, S. (2013). Numerical solution of single piles subjected to pure torsion. Journal of Geotechnical and Geoenvironmental Engineering, 140(1), 74-90.

[8] Beer, G. (1985). An isoparametric joint/interface element for the analysis of fractured rock. Int J Numer Meth Eng, 21, 585-600.

[9] Bishop, A. W., Webb, D. L., & Lewin, P. I. (1965). Undisturbed samples of London Clay from the Ashford Common shaft: strength–effective stress relationships. Geotechnique, 15(1), 1-31.

[10] Brinkgreve, R. B. J. (1994). Geomaterial models and numerical analysis of softening. TU Delft, Delft University of Technology.

[11] Brinkgreve, R., Kumarswamy, S. & Swolfs, W. (2015). Plaxis 3D AE Manuals. Delft: Plaxis bv.

[12] Brinkgreve, R. & Laera, A. (2014). SPCalc Manuals. Delft: XG-Geotools.

[13] Cao, J., Phillips, R., Popescu, R., Audibert, J. M. E., & Al-Khafaji, Z. (2003). Numerical analysis of the behavior of suction caissons in clay. International Journal of Offshore and Polar Engineering, 13(02).

[14] Coffman, R. A., El-Sherbiny, R. M., Rauch, A. F., & Olson, R. E. (2004, January). Measured horizontal capacity of suction caissons. In Offshore Technology Conference. Offshore Technology Conference.

[15] Chow, Y. K. (1985). Torsional response of piles in nonhomogeneous soil. Journal of Geotechnical Engineering, 111(7), 942-947.

[16] Clukey, E. C., & Morrison, M. J. (1993). A centrifuge and analytical study to evaluate suction caissons for TLP applications in the Gulf of Mexico. In Design and performance of deep foundations: Piles and piers in soil and soft rock (pp. 141-156). ASCE.

[17] Deng, W., & Carter, J. P. (2002). A theoretical study of the vertical uplift capacity of suction caissons. International Journal of Offshore and Polar Engineering, 12(02).

[18] Edgers, L., Andresen, L., & Jostad, H. P. (2009). Capacity analysis of suction anchors in clay by 3d finite element analysis. Plaxis BV.

[19] Finn, W. D., & Byrne, P. M. (1972, January). The evaluation of the break-out force for a submerged ocean platform. In Offshore Technology Conference. Offshore Technology Conference.

[20] Fuglsang, L. D., & Steensen-Bach, J. O. (1991). Breakout resistance of suction piles in clay. In Proceedings of the international conference: centrifuge (Vol. 91, pp. 153-9).

[21] Genesis Oil and Gas Consultants Ltd. (2013). Riser Analysis - Advanced Mechanical and Subsea Design - Specialist Technical Services - Services - Genesis Oil and Gas Consultants Ltd. , http://www.genesisoilandgas.com/Services/Specialist-Technical-Services/Advanced-Mechanical-and-Subsea-Design/Riser-Analysis/

[22] Grimstad, G., Andresen, L., & Jostad, H. P. (2012). NGI-ADP: Anisotropic shear strength model for clay. International Journal for Numerical and Analytical Methods in Geomechanics, 36(4), 483-497.

[23] Guo, W. D., & Randolph, M. F. (1996). Torsional piles in non-homogeneous media. Computers and Geotechnics, 19(4), 265-287.

[24] Hight, D. W., Gens, A., & Jardine, R. J. (1985). Evaluation of geotechnical parameters from triaxial tests on offshore clay. In Offshore Site Investigation (pp. 253-268). Springer Netherlands.

[25] Hu, Y., & Randolph, M. F. (1998). H-adaptive FE analysis of elasto-plastic non-homogeneous soil with large deformation. Computers and Geotechnics, 23(1), 61-83.

[26] Janbu, N. (1985). Soil models in offshore engineering. Géotechnique, 35(3), 241-281.

[27] Jeanjean, P., Znidarcic, D., Phillips, R., Ko, H. Y., Pfister, S., & Schroeder, K. (2006). Centrifuge testing on suction anchors: double-wall, stiff clays, and layered soil profile. In Proc. Offshore Technology Conf.

[28] Lee, Y. C., Audibert, J. M. E., & Tjok, K. M. (2005, October). Lessons learned from several suction caisson installation projects in clay. In Proc Int Symp on Frontiers in Offshore Geotechnics (pp. 235-241).

[29] Lee, J., & Randolph, M. (2010). Penetrometer-based assessment of spudcan penetration resistance. Journal of Geotechnical and Geoenvironmental Engineering, 137(6), 587-596.

[30] Lunne, T., & Andersen, K. H. (2007, January). Soft clay shear strength parameters for deepwater geotechnical design. In OFFSHORE SITE INVESTIGATION AND GEOTECHNICS, Confronting New Challenges and Sharing Knowledge. Society of Underwater Technology.

[31] Murff, J. D., & Hamilton, J. M. (1993). P-ultimate for undrained analysis of laterally loaded piles. Journal of Geotechnical Engineering, 119(1), 91-107.

[32] Offshore-mag.com. (2016). Bullwinkle leading generation of platforms in US Gulf scheduled for upgrading. , http://www.offshore-mag.com/articles/print/volume-56/issue-9/news/general-interest/bullwinkle-leading-generation-of-platforms-in-us-gulf-scheduled-for-upgrading.html.

[33] Randolph, M. F. (1981). The response of flexible piles to lateral loading. Geotechnique, 31(2), 247-259.

[34] Randolph, M., Cassidy, M., Gourvenec, S., & Erbrich, C. (2005, September). Challenges of offshore geotechnical engineering. In Proceedings of the international conference on soil mechanics and geotechnical engineering (Vol. 16, No. 1, p. 123).

[35] Randolph, M., & Gourvenec, S. (2011). Offshore geotechnical engineering. CRC Press.

[36] Randolph, M. F., & Houlsby, G. T. (1984). The limiting pressure on a circular pile loaded laterally in cohesive soil. Geotechnique, 34(4), 613-623.

[37] Randolph, M. F., & House, A. R. (2002, January). Analysis of suction caisson capacity in clay. In Offshore technology conference. Offshore Technology Conference.

[38] Randolph, M. F., O'neill, M. P., Stewart, D. P., & Erbrich, C. (1998, January). Performance of suction anchors in fine-grained calcareous soils. In Offshore technology conference. Offshore Technology Conference.

[39] Saviano, A. (2016). Effect of misalignment on the undrained HV capacity of suction anchors in clay. MSc. Delft University of Technology.

[40] Senders, M., & Kay, S. (2002). Geotechnical suction pile anchor design in deep water soft clays. In Conference Deepwater Risers Mooring and Anchorings, London.

[41] Sørlie, E. (2013). Bearing capacity failure envelope of suction caissons subjected to combined loading. Norvegian University of Science and Technology Master Thesis.

[42] Steensen-Bach, J. D. (1992, January). Recent model tests with suction piles in clay and sand. In Offshore Technology Conference. Offshore Technology Conference.

[43] Strukts.com. (2016). Types of offshore platforms. , http://www.strukts.com/2012/05/types-of-offshore-platforms_70.html.

[44] Supachawarote, C., Randolph, M., & Gourvenec, S. (2004, January). Inclined pullout capacity of suction caissons. In The Fourteenth International Offshore and Polar Engineering Conference. International Society of Offshore and Polar Engineers.

[45] Supachawarote, C. (2007). Inclined load capacity of suction caisson in clay. University of Western Australia.

[46] Suroor, H., & Hossain, J. (2015). Effect of torsion on suction piles for subsea and mooring applications. Frontiers in Offshore Geotechnics III, 325.

[47] Taiebat, H. A., & Carter, J. P. (2005, January). Interaction of forces on caissons in undrained soils. In The Fifteenth International Offshore and Polar Engineering Conference. International Society of Offshore and Polar Engineers.

[48] Thian, S. Y., & Lee, C. Y. (2014). Strength and Deformation Characteristics of High Plasticity Offshore Clay. British Journal of Applied Science & Technology, 4(31), 4468.

[49] Watson, P. G., & Randolph, M. F. (1997, January). Vertical capacity of caisson foundations in calcareous sediments. In The Seventh International Offshore and Polar Engineering Conference. International Society of Offshore and Polar Engineers.

[50] Wind-energy-the-facts.org. (2016). Offshore support structures. , http://www.wind-energy-the-facts.org/offshore-support-structures.html

[51] Zdravkovic, L., Potts, D. M., & Jardine, R. J. (1998, January). Pull-out capacity of bucket foundations in soft clay. In Offshore site investigation and foundation behaviour'new frontiers: Proceedings of an international conference. Society of Underwater Technology.

[52] Zienkiewicz, O. C. (1967). The Finite Element Method in Structural and Continum Mechanics: Numerical Solution of Problems in Structural and Continuum Mechanics.

Appendix A

Procedure of Soft Soil model calibration

In this section, the steps that were followed so that the Soft Soil mode calibrations could be accomplished are elaborated. In this way, a better insight into the way each one of the model parameters was determined is given. In Section 4.4.2, it is highlighted that the accomplishment of this task has as a prerequisite that certain assumptions regarding material parameters are made. These assumptions include the value of the angle of friction, ϕ'. The value of ϕ' is equal to 18° for calibration A and ° for calibrations B, C, D and E.

The first step of the calibration is to match the elastic loading behaviour of the Mohr - Coulomb model with the unloading - reloading behaviour of the Soft Soil model, which is also elastic even though plastic strains are also generated. To accomplish that, the elastic shear moduli, G, of both models are set equal as described below. As an outcome of this mathematical derivation, the determination of k^* is feasible.

For the total stress analysis of the benchmark study, it is true that $E_{\mathrm{u}} = 625z$ and $\nu_{\mathrm{u}} = 0.49$. Thus, the elastic shear modulus of the Mohr - Coulomb model is given by the first part of Equation **??** and, it in this case, it is equal to:

$$G_{\mathrm{MC}} = 209z \tag{A.1}$$

When the Soft Soil model is considered, the shear modulus of unloading - reloading is computed through the following equation taking into account elasticity.

$$G_{\mathrm{SS}} = \frac{3K_{\mathrm{ur}}(1 - 2\nu_{\mathrm{ur}})}{2(1 + \nu_{\mathrm{ur}})} \tag{A.2}$$

Where p'_{ref} is computed via Equation A.3, considering that the effective unit weight, γ' equals $\gamma_{\mathrm{sat}} - \gamma_{\mathrm{w}} = 16 - 10 = 6kN/m^3$.

$$p'_{\mathrm{ref}} = \frac{(1 + 2K_{\mathrm{o}})\gamma' z}{3} \tag{A.3}$$

Setting the equations A.1 and A.2 equal leads to the computation of the modified swelling index, k^*. The computed values vary for each calibration but they all lie in the range of 0.0163 and 0.186.

The final step of the calibration involves an iterative procedure that aims to the determination of the modified swelling index, λ^*, the lateral earth pressure coefficient, $K_{\mathrm{o}}^{\mathrm{nc}}$, and k^* and stops when the preferable soil response is achieved. For instance, the goal of Calibrations A and B is to achieve the same peak undrained shear strength in compression and shear with the benchmark study.

Appendix B

Soft Soil model responses for Calibrations C, D and E

The responses of the Soft Soil model under different types of loading using the material parameters of Calibrations C, D and E are depicted in the sections that follow. Simultaneously, the obtained soil behaviour from the calibrated models is compared with the benchmark study that uses a Tresca failure criterion. The graphs stem from numerical simulations of real geotechnical laboratory tests, including:

- Undrained triaxial compression (TXC)
- Undrained triaxial extension (TXE)
- Undrained direct simple shear (DSS)

The tests listed above were conducted within the Plaxis Soil Test Facility for a single stress point located at 30 meters depth. The soil behaviour depicted in these graphs reflects qualitatively the soil behaviour that is expected at every single stress point in the soil domain.

See next pages for graphs.

B.1 Calibration C

The aim of this calibration is to match the extensive behaviour of the soil that is present in the benchmark study. The calibrated parameters and the respective soil response can be found below.

Table B.1: Soft Soil model parameters of Calibration C

Parameters	**Symbol**	**Values**
Friction angle	ϕ'	22 °
Lateral earth pressure coefficient	K_o^{nc}	0.6362
Modified compression index	λ^*	0.1
Modified swelling index	κ^*	0.0163
K_o^{nc} - parameter	$M_{\text{Soft Soil}}$	1.226

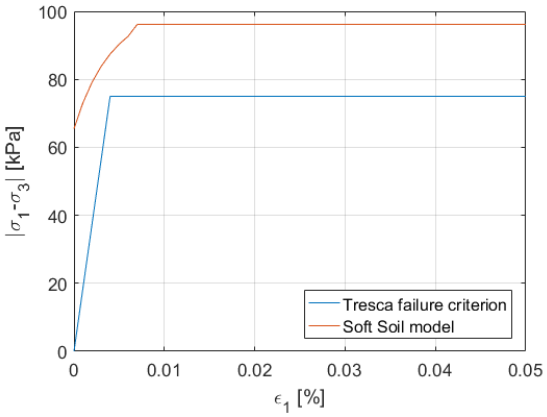

Figure B.1: Undrained triaxial compression of Calibration C

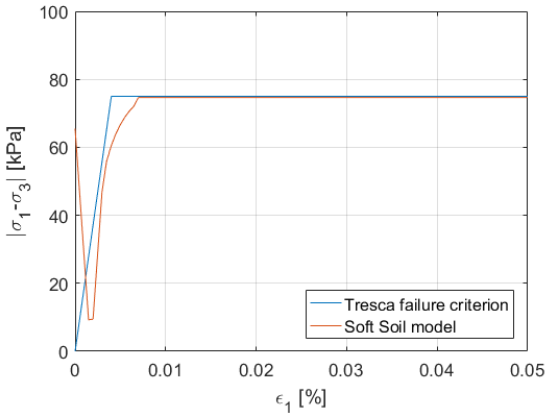

Figure B.2: Undrained triaxial extension of Calibration C

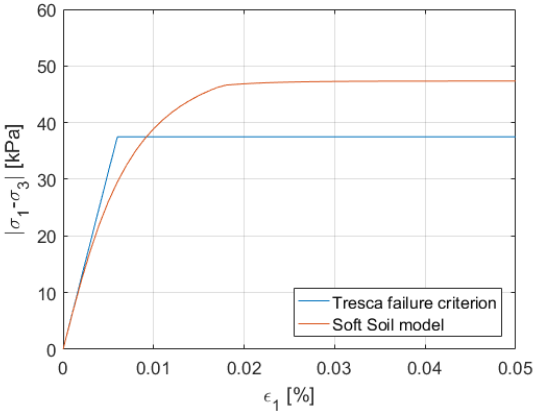

Figure B.3: Undrained direct simple shear of Calibration C

B.2 Calibration D

The purpose of this calibrations is to have an average behaviour stemming from undrained TXC, TXE and DSS that matches the the soil behaviour of the benchmark study.

Table B.2: Soft Soil model parameters of Calibration D

Parameters	**Symbol**	**Values**
Friction angle	ϕ'	22 °
Lateral earth pressure coefficient	$K_{\mathrm{o}}^{\mathrm{nc}}$	0.76
Modified compression index	λ^*	0.16
Modified swelling index	κ^*	0.0181
$K_{\mathrm{o}}^{\mathrm{nc}}$ - parameter	$M_{\text{Soft Soil}}$	0.9266

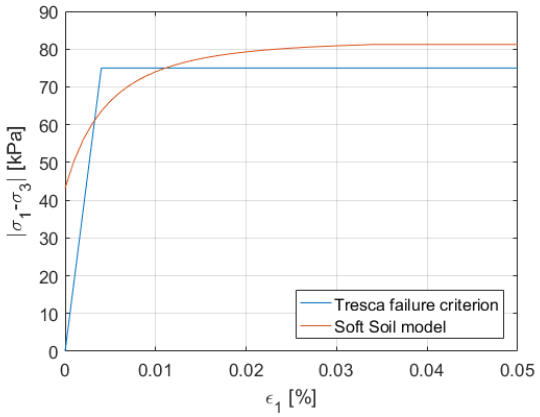

Figure B.4: Undrained triaxial compression of Calibration D

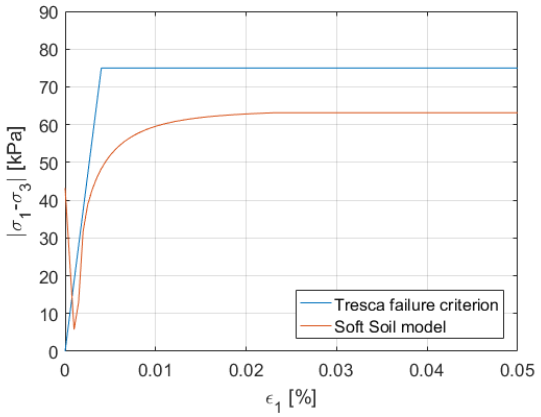

Figure B.5: Undrained triaxial extension of Calibration D

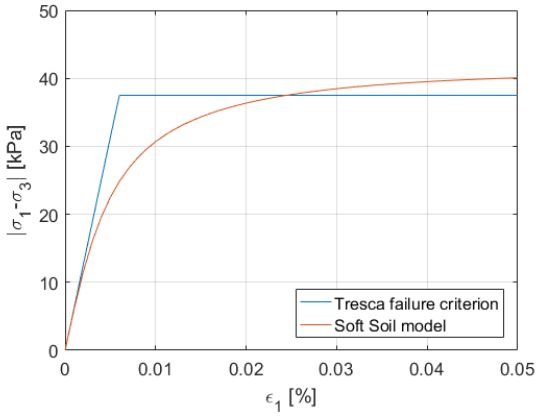

Figure B.6: Undrained direct simple shear of Calibration D

B.3 Calibration E

The goal of this calibration is to have an average behaviour coming form TXC and TXE that fits the soil behaviour of the benchmark study.

Table B.3: Soft Soil model parameters of Calibration E

Parameters	Symbol	Values
Friction angle	ϕ'	22 °
Lateral earth pressure coefficient	K_o^{nc}	0.74
Modified compression index	λ^*	0.14
Modified swelling index	κ^*	0.0178
K_o^{nc} - parameter	$M_{\text{Soft Soil}}$	0.9721

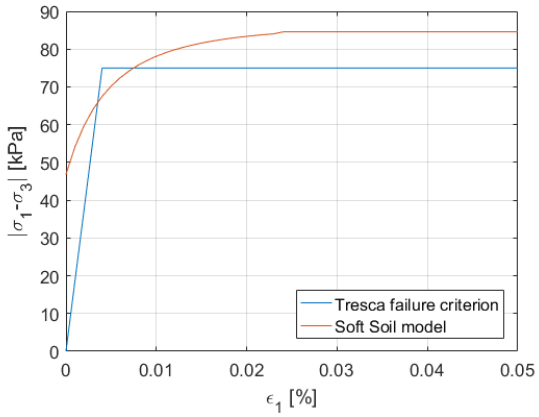

Figure B.7: Undrained triaxial compression of Calibration E

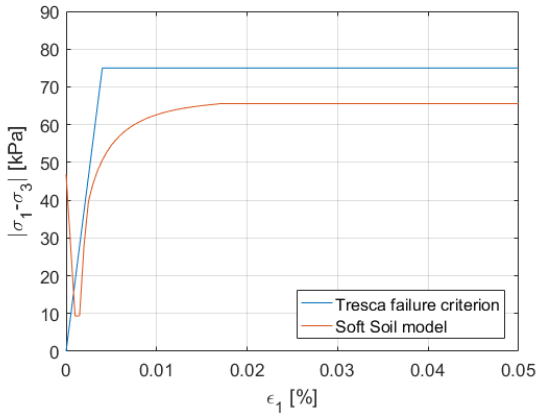

Figure B.8: Undrained triaxial extension of Calibration E

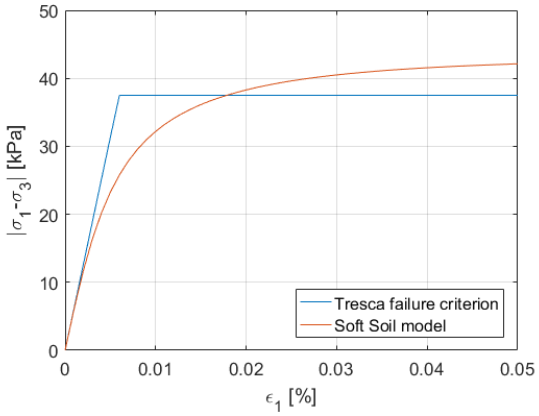

Figure B.9: Undrained direct simple shear of Calibration E

Appendix C

Benchmark Study Results

C.1 Limit loads for all aspect ratios

In this section, the limit loads that stemmed from the numerical analysis of the benchmark for all aspect ratios are presented. There are the loads that are used for the creation of the comparative HV interaction diagrams illustrated in the main matter of this thesis. Vertical (V), horizontal (H), inclined (F) and torsional (T) limit loads for various loading , θ, and torsional angles, β are available in the tables that follow. Additionally, normalised ratios, H/H_{ult} and V/V_{ult}, are also provided.

Table C.1: Benchmark Study Results for different misalignment angles of L/D = 1.5

θ[°]	H [kN]	V[kN]	F [kN]	T [kN]	H/H_{ult} [-]	V/V_{ult} [-]
$\beta = 0°$						
0	1719	0	1719	0	1.00	0.00
12	1695	360	1733	0	0.99	0.30
37	1237	932	1549	0	0.72	0.77
56	772	1144	1380	0	0.45	0.95
72	392	1206	1268	0	0.23	1.00
90	0	1207	1207	0	0.00	1.00
$\beta = 5°$						
0	1684	0	1684	367	1.00	0.00
12	1664	354	1701	363	0.99	0.29
37	1233	929	1544	269	0.73	0.77
56	770	1142	1378	168	0.46	0.95
72	392	1205	1267	85	0.23	1.00
90	0	1207	1207	0	0.00	1.00
$\beta = 10°$						
0	1590	0	1590	690	1.00	0.00
12	1583	337	1619	687	1.00	0.28
37	1217	917	1524	528	0.77	0.76
56	767	1137	1371	333	0.48	0.94
72	391	1203	1265	170	0.25	1.00
90	0	1208	1208	0	0.00	1.00

Table C.2: Benchmark Study Results for different misalignment angles of L/D = 3

θ[°]	H [kN]	V[kN]	F [kN]	T [kN]	H/H_{ult} [-]	V/V_{ult} [-]
$\beta = 0°$						
0	7741	0	7741	0	1.00	0.00
18	7342	2386	7720	0	0.95	0.45
31	6231	3744	7270	0	0.80	0.70
46	4474	4634	6441	0	0.58	0.87
85	336	5312	5322	0	0.04	1.00
90	0	5312	5312	0	0.00	1.00
$\beta = 5°$						
0	7475	0	7475	1629	1.00	0.00
18	7186	2335	7555	1566	0.96	0.44
31	6154	3698	7179	1341	0.82	0.70
46	4440	4598	6391	967	0.59	0.87
85	336	5311	5321	73	0.04	1.00
90	0	5312	5312	0	0.00	1.00
$\beta = 10°$						
0	6916	0	6916	3002	1.00	0.00
18	6721	2184	7067	2918	0.97	0.41
31	5886	3537	6867	2555	0.85	0.67
46	4336	4491	6242	1882	0.63	0.85
85	336	5312	5322	146	0.05	1.00
90	0	5313	5313	0	0	1

Table C.3: Benchmark Study Results for different misalignment angles of L/D = 6

θ[°]	H [kN]	V[kN]	F [kN]	T [kN]	H/H_{ult} [-]	V/V_{ult} [-]
$\beta = 0°$						
0	33630	0	33630	0	1.00	0.00
9.46	32494	5414	32942	0	0.97	0.36
16.8	30462	9197	31820	0	0.91	0.62
20.81	28726	10918	30731	0	0.85	0.73
90	0	14878	14878	0	0.00	1.00
$\beta = 5°$						
0	31729	0	31729	6913	1.00	0.00
9.46	31153	5191	31582	6788	0.98	0.35
16.8	29479	8900	30794	6423	0.93	0.60
20.81	27911	10608	29859	6082	0.88	0.71
90	0	14877	14877	0	0.00	1.00
$\beta = 10°$						
0	28802	0	28802	12504	1.00	0.00
9.46	28264	4710	28654	12270	0.98	0.32
16.8	27006	8154	28210	11724	0.94	0.55
20.81	25762	9791	27560	11184	0.89	0.66
90	0	14877	14877	0	0.00	1.00

C.2 HV interaction diagrams and shape coefficients

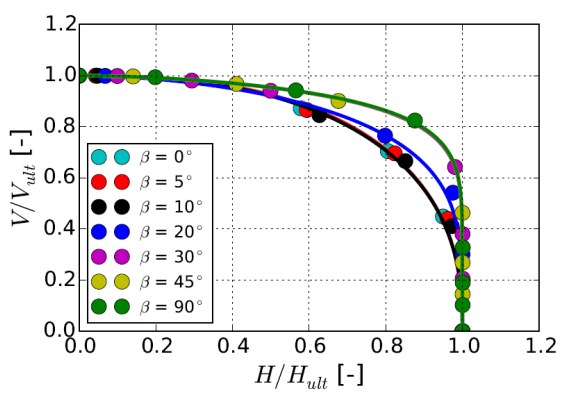

(a) HV interaction diagram

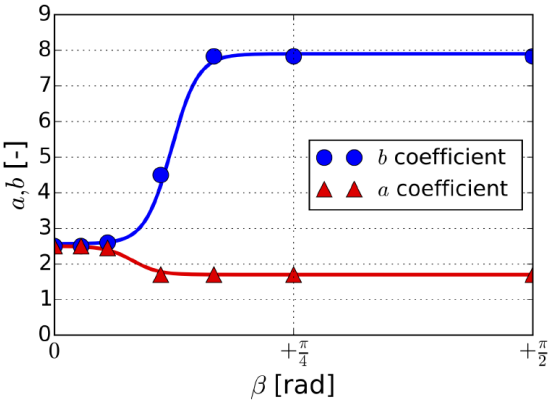

(b) a, b shape coefficients

Figure C.1: Misalignment effect on HV interaction diagrams and a, b shape coefficients for medium anchor ($L/D = 3$) [39]

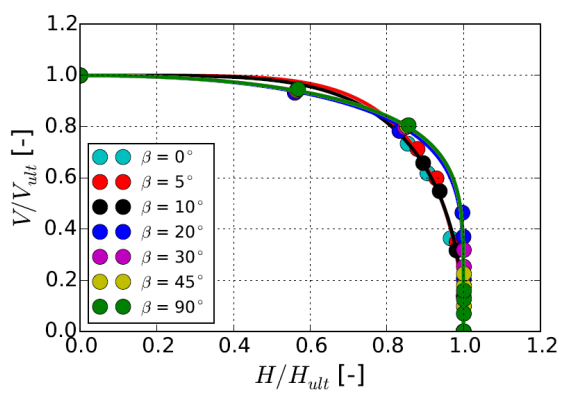

(a) HV interaction diagram

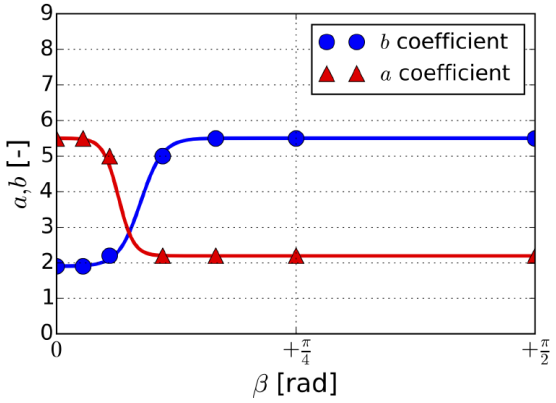

(b) a, b shape coefficients

Figure C.2: Misalignment effect on HV interaction diagrams and a, b shape coefficients for long anchor ($L/D = 6$) [39]

Appendix D

Effective Stress Analysis Results

In this section, figures that illustrate the final displacements of the mesh for all the aspect ratios of Calibration A are available. Additionally, the ultimate loads that are obtained from the effective stress analysis carried out by Plaxis 3D are presented in this section in the form of tables. These limit loads were essential for the creation of the comparative HV interaction diagrams depicted in the main matter of this thesis. Vertical (V), horizontal (H), inclined (F) and torsional (T) limit loads for various loading angles, θ, and torsional angles, β can be found in the tables that follow. Additionally, normalised ratios, H/H_{ult} and V/V_{ult}, are also computed.

The torsional limit loads (T) are computed through the following formula which is schematically explained in Figure D.1.

$$T = H \cdot \sin\beta \cdot \frac{D}{2} \tag{D.1}$$

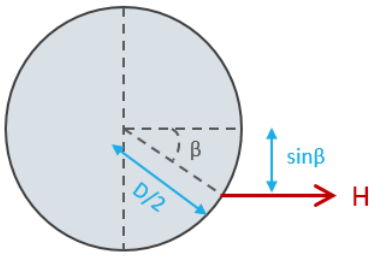

Figure D.1: Computation of torsion induced on the pile due to β

Only in the case of the initial Calibration A, load - displacement curves are provided. The examined displacements correspond to a point that is located at the center of the top cap of the anchor. The evolution of lateral, as well as vertical ultimate capacities, during the analyses are demonstrated. For the majority of the analysis, the point at which the calculations stop, and the curves end, is determined by Plaxis 3D revealing that this is the point where failure has been reached and bearing capacity has been fully activated. However, in a few cases, analysis were stopped manually as a well - defined yield plateau has been formed but the analyses kept running for days.

See next pages for results.

D.1 Calibration A

D.1.1 Suction anchor with L/D = 1.5

Table D.1: Calibration A results for different misalignment angles of L/D = 1.5

θ[°]	H [kN]	V[kN]	F [kN]	T [kN]	H/H_{ult} [-]	V/V_{ult} [-]
$\beta = 0°$						
0	1599	0	1599	0	1.00	0.00
12	1545	328	1580	0	0.97	0.32
37	1094	824	1369	0	0.68	0.79
56	672	996	1201	0	0.42	0.96
72	340	1045	1099	0	0.21	1.00
90	0	1042	1042	0	0.00	1.00
$\beta = 10°$						
0	1498	0	1498	650	1.00	0.00
12	1470	312	1502	638	0.98	0.30
37	1074	810	1345	466	0.72	0.78
56	665	986	1190	289	0.44	0.95
72	339	1042	1096	147	0.23	1.00
90	0	1042	1042	0	0.00	1.00

Misalignment angle of 10°

The load - displacement curves of the short suction anchor without the presence of rotation are provided in the main matter of this thesis (Section 4.7.2).

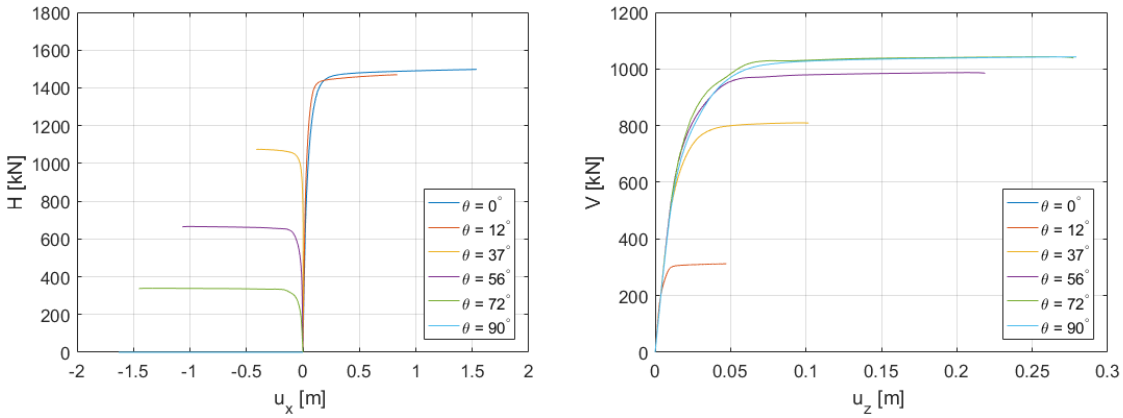

(a) H - u_x curves (b) V - u_z curves

Figure D.2: Load - displacement curves for different load inclinations of suction anchor with $L/D = 1.5$ ($\beta = 10°$)

D.1.2 Suction anchor with L/D = 3

Displacements due to horizontal loading ($\theta = 0°$)

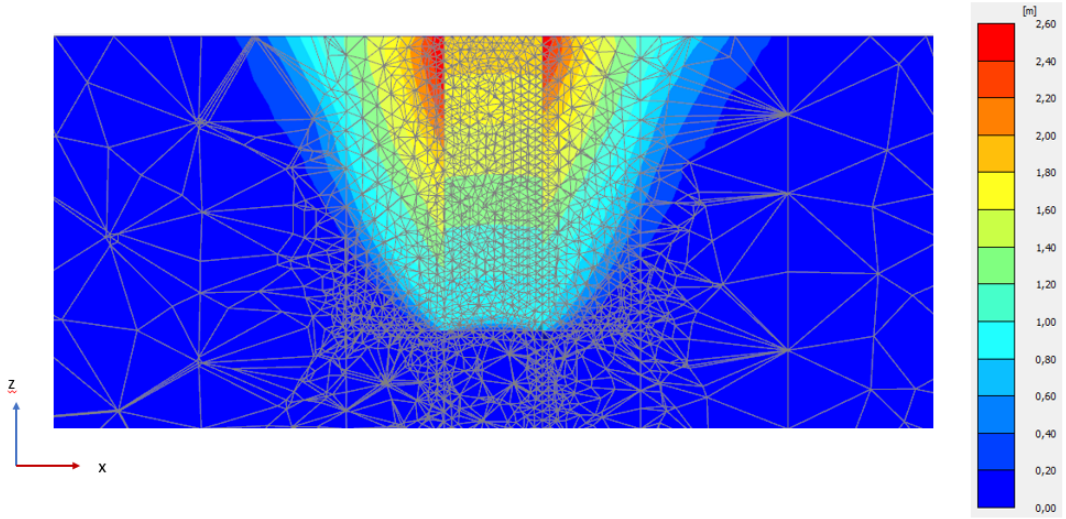

Figure D.3: Displacements (shading) of medium anchor due to horizontal loading (maximum displacement = 2.58 m)

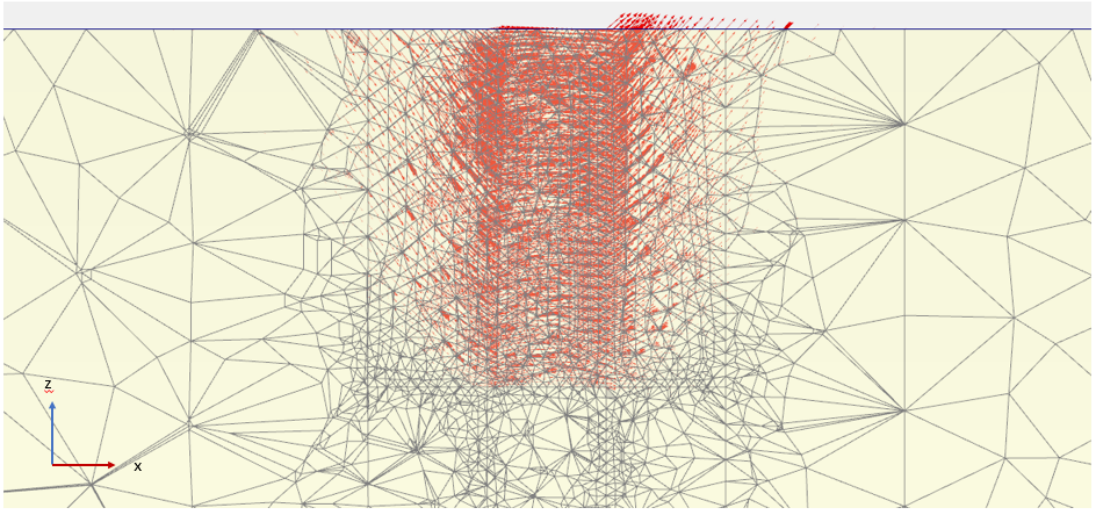

Figure D.4: Displacements (arrows) of medium anchor due to horizontal loading (maximum displacement = 2.58 m)

Displacements due to inclined loading ($\theta = 46°$)

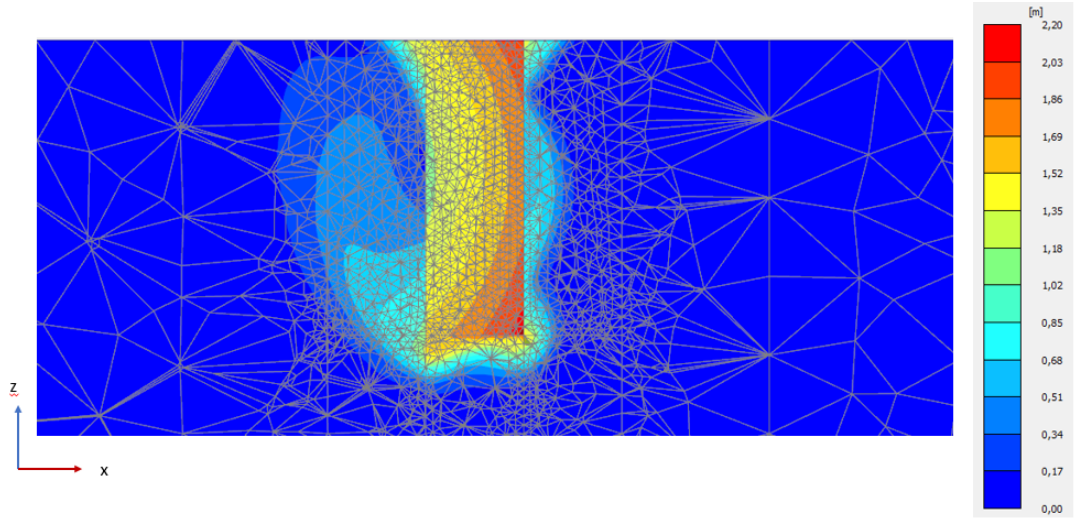

Figure D.5: Displacements (shading) of medium anchor due to loading of $\theta = 46°$ (maximum displacement = 2.13 m)

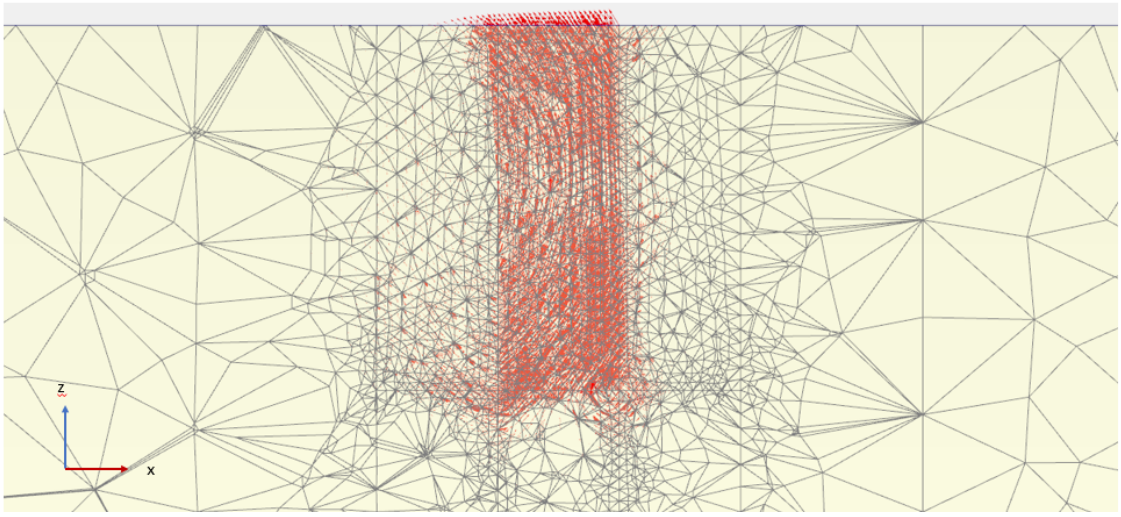

Figure D.6: Displacements (arrows) of medium anchor due to loading of $\theta = 46°$ (maximum displacement = 2.13 m)

Displacements due to vertical loading ($\theta = 90°$)

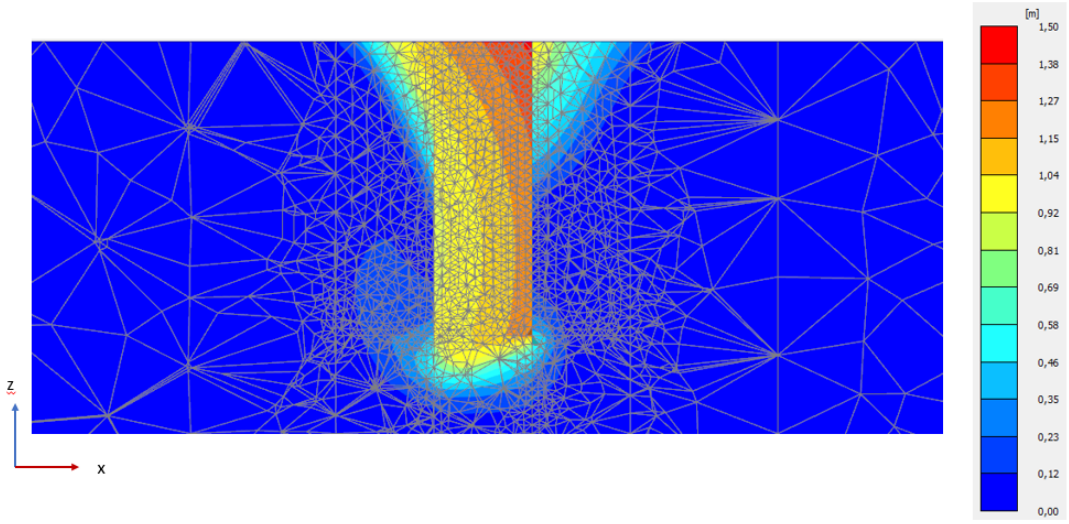

Figure D.7: Displacements (shading) of medium anchor due to vertical loading (maximum displacement = 1.41 m)

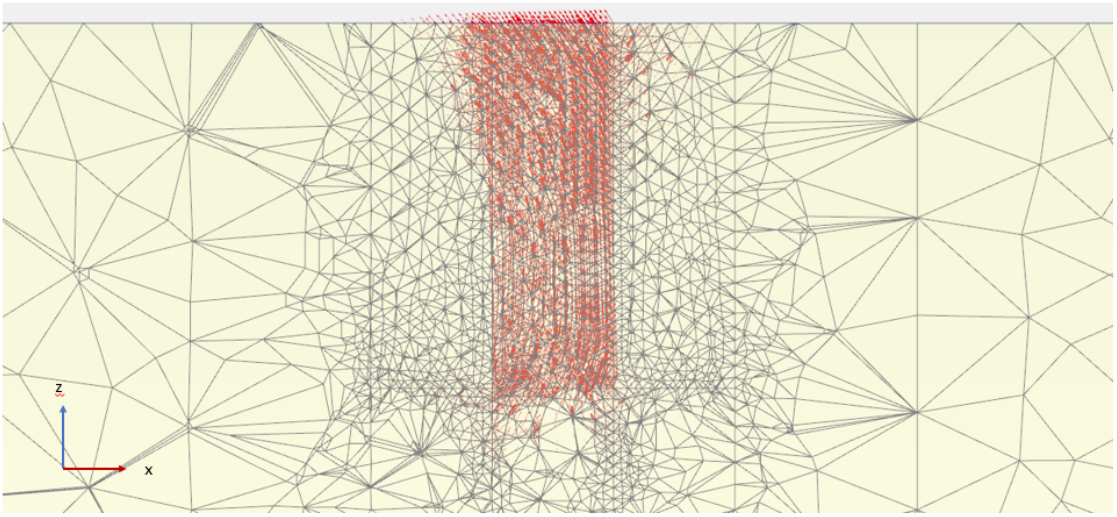

Figure D.8: Displacements (arrows) of medium anchor due to vertical loading (maximum displacement = 1.41 m)

Table D.2: Calibration A results for different misalignment angles of L/D = 3

θ[°]	H [kN]	V[kN]	F [kN]	T [kN]	H/H_{ult} [-]	V/V_{ult} [-]
$\beta = 0°$						
0	7032	0	7032	0	1.00	0.00
18	6648	2160	6991	0	0.95	0.47
31	5528	3322	6450	0	0.79	0.72
46	3917	4057	5640	0	0.56	0.88
90	0	4594	4594	0	0.00	1.00
$\beta = 10°$						
0	6416	0	6416	2785	1.00	0.00
18	6270	2037	6593	2722	0.98	0.44
31	5265	3164	6142	2286	0.82	0.69
46	3800	3935	5470	1650	0.59	0.86
90	0	4594	4594	0	0.00	1.00

No misalignment angle

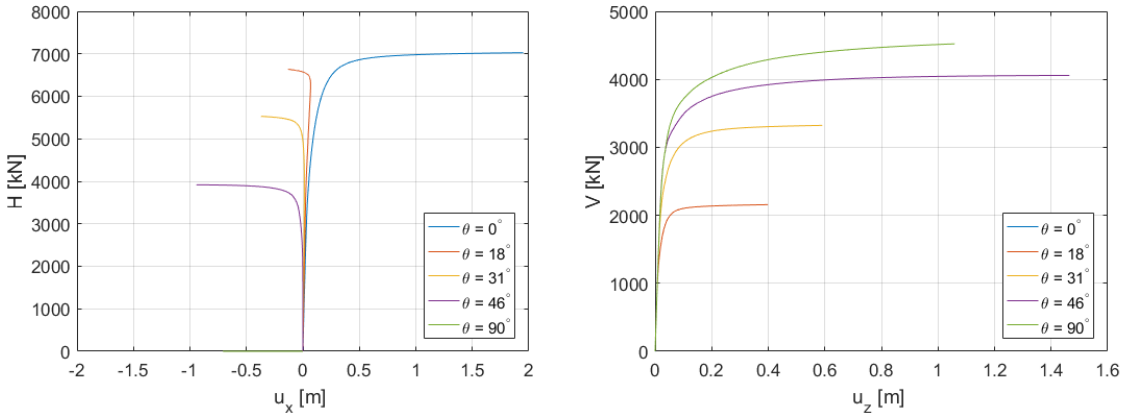

(a) H - u_x curves (b) V - u_z curves

Figure D.9: Load - displacement curves for different load inclinations of suction anchor with $L/D = 3$ ($\beta = 0°$)

Misalignment angle of 10°

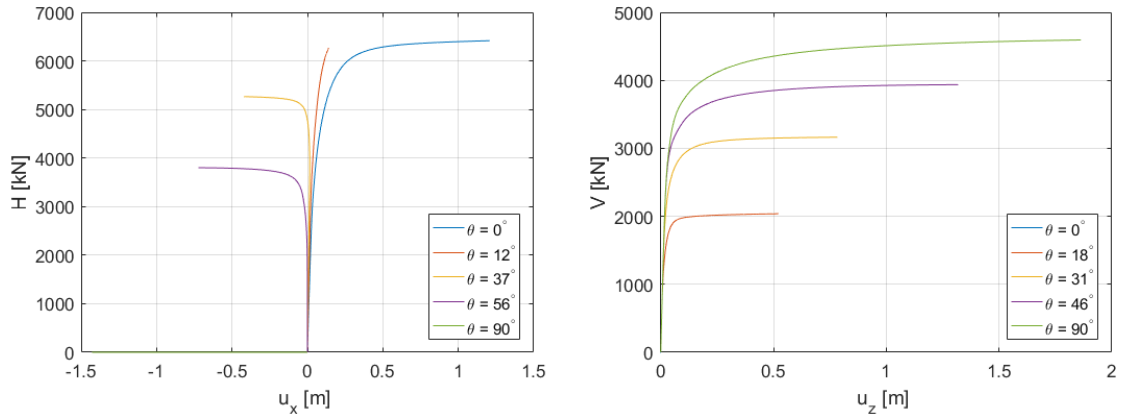

(a) H - u_x curves (b) V - u_z curves

Figure D.10: Load - displacement curves for different load inclinations of suction anchor with $L/D = 3$ ($\beta = 10°$)

D.1.3 Suction anchor with L/D = 6

Displacements due to horizontal loading ($\theta = 0°$)

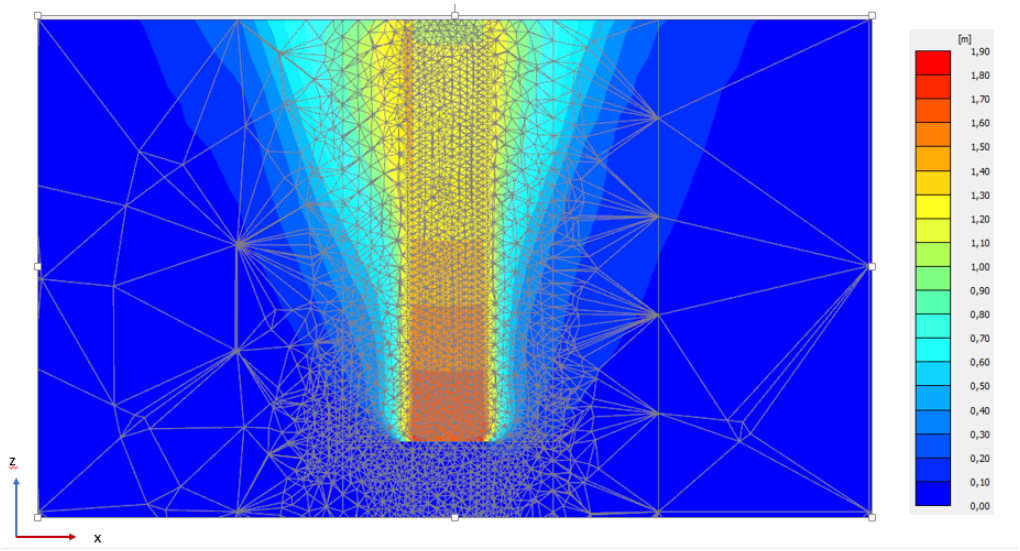

Figure D.11: Displacements (shading) of long anchor due to horizontal loading (maximum displacement = 1.82 m)

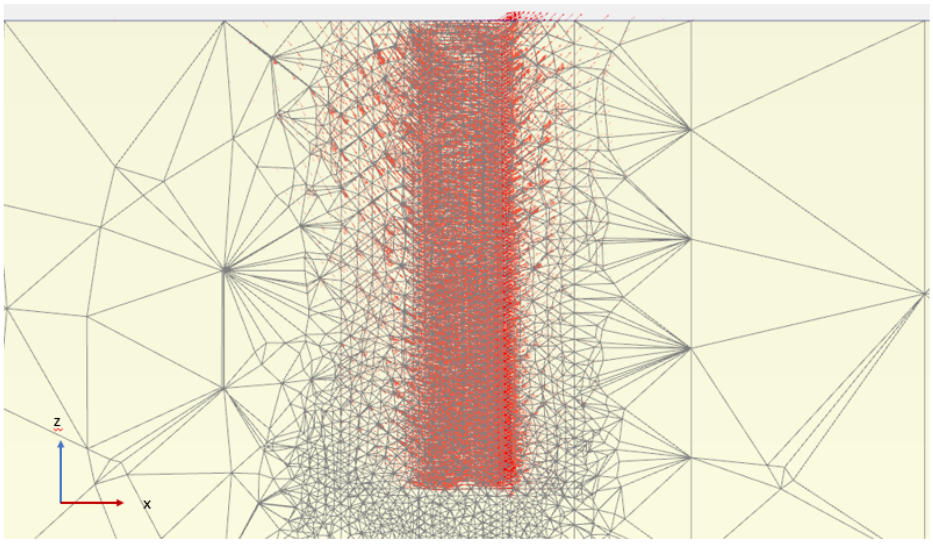

Figure D.12: Displacements (arrows) of long anchor due to horizontal loading (maximum displacement = 1.82 m)

Displacements due to inclined loading ($\theta = 20.81°$)

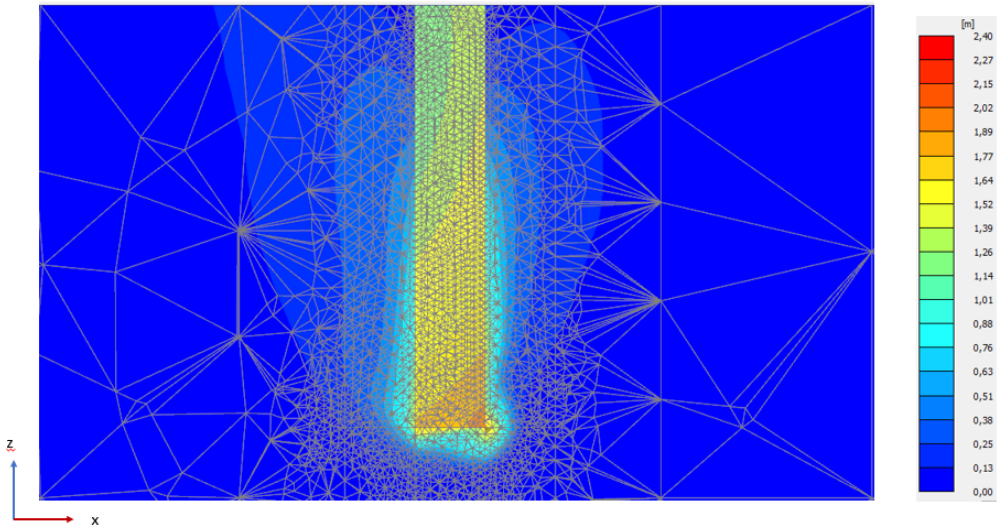

Figure D.13: Displacements (shading) of long anchor due to loading of $\theta = 20.81°$ (maximum displacement = 2.39 m)

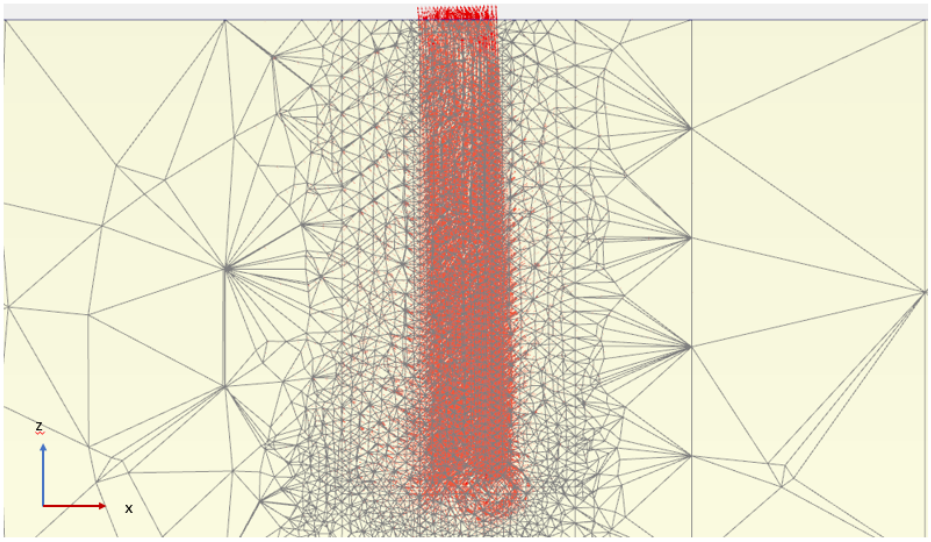

Figure D.14: Displacements (arrows) of long anchor due to loading of $\theta = 20.81°$ (maximum displacement = 2.39 m)

Displacements due to vertical loading ($\theta = 90°$)

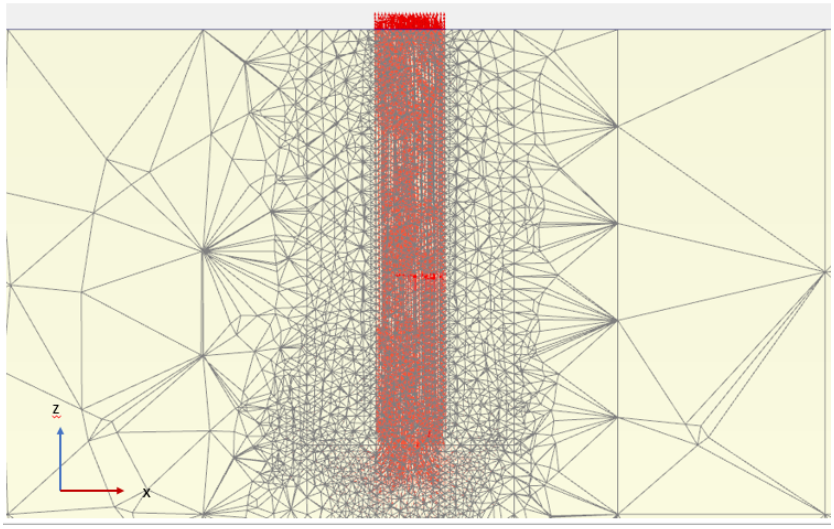

Figure D.15: Displacements (shading) of long anchor due to vertical loading (maximum displacement = 2.13 m)

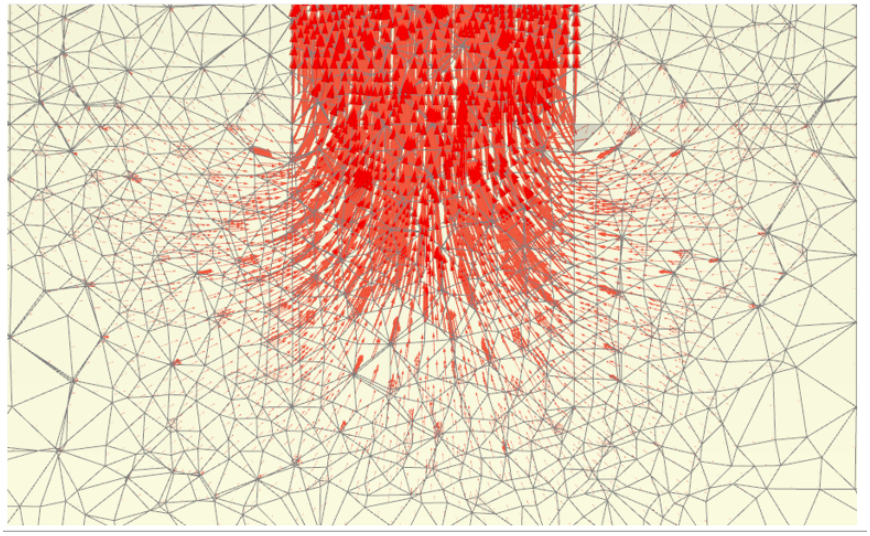

Figure D.16: Detail of displacements (arrows) at the bottom of long anchor due to vertical loading

Table D.3: Calibration A results for different misalignment angles of L/D = 6

θ[°]	H [kN]	V[kN]	F [kN]	T [kN]	H/H_{ult} [-]	V/V_{ult} [-]
$\beta = 0°$						
0	30522	0	30522	0	1.00	0.00
9.46	29412	4901	29818	0	0.96	0.36
16.8	27969	8444	29216	0	0.92	0.62
20.81	26526	10082	28377	0	0.85	0.72
90	0	13713	13713	0	0.00	1.00
$\beta = 10°$						
0	26637	0	26637	11564	1.00	0.00
9.46	26526	4420	26892	11516	1.00	0.32
16.8	25638	7741	26781	11130	0.96	0.56
20.81	24529	9322	26241	10167	0.88	0.65
90	0	13713	13713	0	0.00	1.00

No misalignment angle

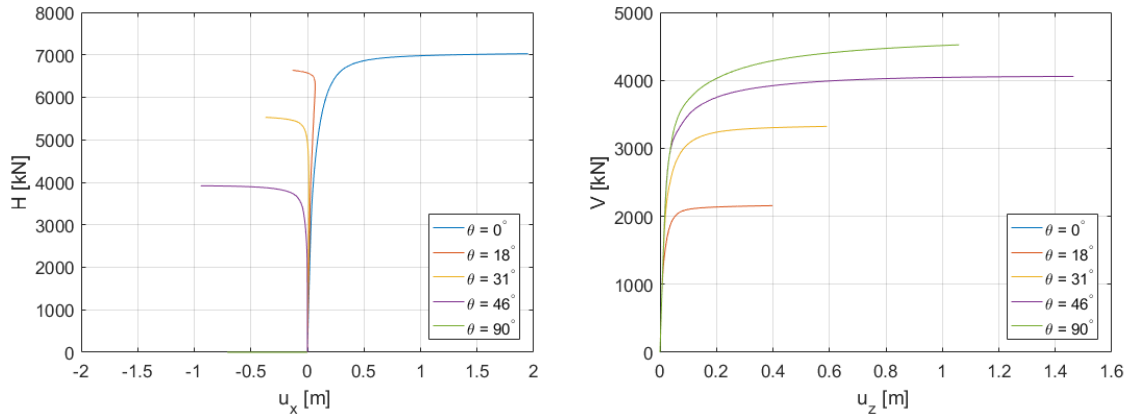

(a) H - u_x curves (b) V - u_z curves

Figure D.17: Load - displacement curves for different load inclinations of suction anchor with $L/D = 6$ ($\beta = 0°$)

Misalignment angle of 10°

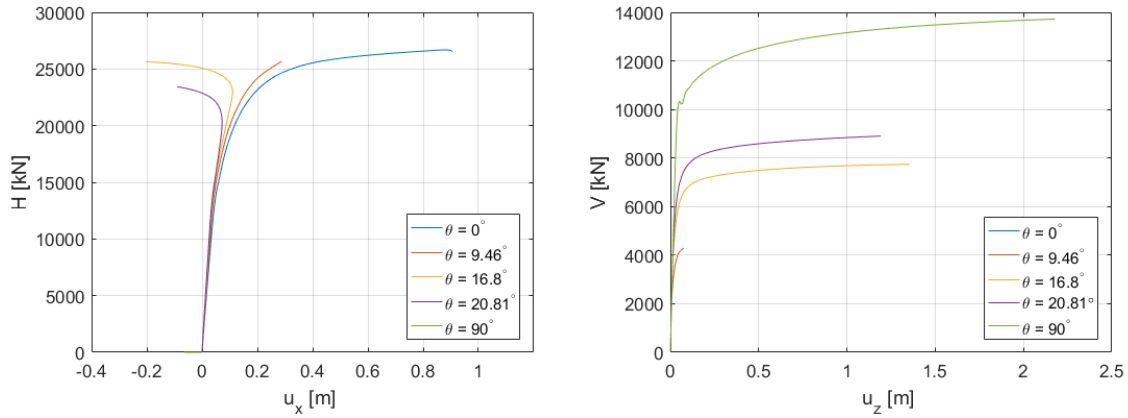

(a) H - u_x curves (b) V - u_z curves

Figure D.18: Load - displacement curves for different load inclinations of suction anchor with $L/D = 6$ ($\beta = 10°$)

D.2 Calibration B

Table D.4: Calibration B results for different misalignment angles

θ[°]	H [kN]	V[kN]	F [kN]	T [kN]	H/H_{ult} [-]	V/V_{ult} [-]
$\beta = 0°$						
0	1601	0	1601	0	1.00	0.00
12	1538	327	1572	0	0.96	0.31
37	1094	824	1369	0	0.68	0.79
56	672	997	1202	0	0.42	0.96
72	336	1034	1088	0	0.21	0.99
90	0	1042	1042	0	0.00	1.00
$\beta = 10°$						
0	1491	0	1491	647	1.00	0.00
12	1470	312	1502	638	0.99	0.30
37	1071	807	1341	465	0.72	0.78
56	663	983	1186	288	0.44	0.95
72	338	1039	1093	147	0.23	1.01
90	0	1034	1034	0	0.00	1.00

D.3 Calibration C

Table D.5: Calibration C results for different misalignment angles

θ[°]	H [kN]	V[kN]	F [kN]	T [kN]	H/H_{ult} [-]	V/V_{ult} [-]
$\beta = 0°$						
0	1994	0	1994	0	1.00	0.00
12	1914	407	1957	0	0.96	0.32
37	1356	1022	1698	0	0.68	0.79
56	832	1233	1487	0	0.42	0.96
72	422	1297	1364	0	0.21	1.01
90	0	1287	1287	0	0.00	1.00
$\beta = 10°$						
0	1880	0	1880	816	1.00	0.00
12	1823	387	1863	791	0.97	0.30
37	1327	1000	1662	576	0.71	0.78
56	820	1216	1467	356	0.44	0.95
72	422	1297	1364	183	0.22	1.01
90	0	1287	1287	0	0.00	1.00

D.4 Calibration D

Table D.6: Calibration D results for different misalignment angles

θ[°]	H [kN]	V[kN]	F [kN]	T [kN]	H/H_{ult} [-]	V/V_{ult} [-]
$\beta = 0°$						
0	1709	0	1709	0	1.00	0.00
12	1640	349	1677	0	0.96	0.32
37	1162	876	1455	0	0.68	0.80
56	712	1056	1273	0	0.42	0.96
72	359	1104	1161	0	0.21	1.01
90	0	1095	1095	0	0.00	1.00
$\beta = 10°$						
0	1606	0	1606	697	1.00	0.00
12	1561	332	1596	678	0.97	0.30
37	1145	863	1434	497	0.71	0.79
56	706	1047	1263	307	0.44	0.96
72	359	1104	1161	156	0.22	1.01
90	0	1095	1095	0	0.00	1.00

D.5 Calibration E

Table D.7: Calibration E results for different misalignment angles

θ[°]	H [kN]	V[kN]	F [kN]	T [kN]	H/H_{ult} [-]	V/V_{ult} [-]
$\beta = 0°$						
0	1771	0	1771	0	1.00	0.00
12	1703	362	1741	0	0.96	0.32
37	1206	909	1510	0	0.68	0.80
56	737	1092	1317	0	0.42	0.96
72	371	1143	1201	0	0.21	1.00
90	0	1138	1138	0	0.00	1.00
$\beta = 10°$						
0	1669	0	1669	725	1.00	0.00
12	1615	343	1652	701	0.97	0.30
37	1185	893	1484	514	0.71	0.78
56	729	1081	1304	317	0.44	0.95
72	370	1140	1198	161	0.22	1.00
90	0	1138	1138	0	0.00	1.00

Appendix E

SPCalc Results

A summary of all the limit loads obtained from the SPCalc analyses is presented in tables for three misalignment angles ($\beta = 0°, 5°$ and $10°$) and three aspect ratios ($L/D = 1.5$, 3 and 6) including vertical (V), horizontal (H), inclined (F) and torsional (T) limit loads for various loading angles, θ, and torsional angles, β, as well as computed ratios, H/H_{ult} and V/V_{ult}.

Table E.1: SPCalc Results for different misalignment angles of L/D = 1.5

θ[°]	H [kN]	V[kN]	F [kN]	T [kN]	H/H_{ult} [-]	V/V_{ult} [-]
$\beta = 0°$						
0	1520	0	1520	0	1.00	0.00
12	1477	314	1510	0	0.97	0.28
37	1079	813	1351	0	0.71	0.74
56	684	1014	1223	0	0.45	0.92
72	355	1091	1147	0	0.23	0.99
90	0	1104	1104	0	0.00	1.00
$\beta = 5°$						
0	1493	0	1493	325	1.00	0.00
12	1459	310	1492	318	0.98	0.28
37	1071	807	1341	233	0.72	0.73
56	678	1005	1212	148	0.45	0.91
72	350	1078	1134	76	0.23	0.98
90	0	1104	1104	0	0.00	1.00
$\beta = 10°$						
0	1381	0	1381	600	1.00	0.00
12	1373	292	1404	596	0.99	0.26
37	1040	784	1302	451	0.75	0.71
56	668	990	1195	290	0.48	0.90
72	351	1082	1137	153	0.25	0.98
90	0	1104	1104	0	0.00	1.00

Table E.2: SPCalc Results for different misalignment angles of L/D = 3

θ[°]	H [kN]	V[kN]	F [kN]	T [kN]	H/H_{ult} [-]	V/V_{ult} [-]
$\beta = 0°$						
0	6408	0	6408	0	1.00	0.00
18	5892	1914	6195	0	0.92	0.38
31	5132	3084	5987	0	0.80	0.61
46	3988	4130	5742	0	0.62	0.82
66	2147	4823	5279	0	0.34	0.96
85	442	5050	5069	0	0.07	1.01
90	0	5022	5022	0	0.00	1.00
$\beta = 5°$						
0	6331	0	6331	1379	1.00	0.00
18	5837	1897	6138	1272	0.92	0.38
31	5157	3099	6016	1124	0.81	0.62
46	3944	4084	5678	859	0.62	0.81
66	2143	4813	5269	467	0.34	0.96
85	433	4950	4969	94	0.07	0.99
90	0	5022	5022	0	0.00	1.00
$\beta = 10°$						
0	6001	0	6001	2605	1.00	0.00
18	5667	1841	5959	2460	0.94	0.37
31	4999	3004	5832	2170	0.83	0.60
46	3901	4039	5615	1693	0.65	0.80
66	2133	4790	5243	926	0.36	0.95
85	439	5018	5037	191	0.07	1.00
90	0	5022	5022	0	0.00	1.00

Table E.3: SPCalc Results for different misalignment angles of L/D = 6

θ[°]	H [kN]	V[kN]	F [kN]	T [kN]	H/H_{ult} [-]	V/V_{ult} [-]
$\beta = 0°$						
0	25222	0	25222	0	1.00	0.00
10	24550	4329	24929	0	0.97	0.29
18	23774	7725	24997	0	0.94	0.52
27	21716	11065	24372	0	0.86	0.74
40	16022	13444	20915	0	0.64	0.90
55	10274	14673	17913	0	0.41	0.98
90	0	14952	14952	0	0.00	1.00
$\beta = 5°$						
0	25017	0	25017	5451	1.00	0.00
10	24350	4294	24726	5306	0.97	0.29
18	23540	7649	24752	5129	0.94	0.51
27	21260	10833	23861	4632	0.85	0.72
40	15471	12981	20195	3371	0.62	0.87
55	9957	14219	17359	2169	0.40	0.95
90	0	14952	14952	0	0.00	1.00
$\beta = 10°$						
0	24212	0	24212	10511	1.00	0.00
10	23552	4153	23915	10224	0.97	0.28
18	22773	7399	23945	9886	0.94	0.49
27	20075	10229	22531	8715	0.83	0.68
40	15461	12973	20182	6712	0.64	0.87
55	10106	14432	17619	4387	0.42	0.97
90	0	14952	14952	0	0.00	1.00